Skew-Kappa distribution functions & whistler heat flux instability in the solar wind: the Core-Strahlo model

Tesis entregada a la Universidad de Chile

En cumplimiento parcial de los requisitos para optar al grado de

Doctora en Ciencias con mención en Física

Facultad de Ciencias

por

Beatriz Antonia Zenteno Quinteros

Santiago de Chile

Noviembre, 2023

Director de tesis: **Dr. Pablo S. Moya**

FACULTAD DE CIENCIAS
UNIVERSIDAD DE CHILE

INFORME DE APROBACIÓN
TESIS DE DOCTORADO

Se informa a la Escuela de Postgrado de la Facultad de Ciencias que la Tesis de Doctorado presentada por la candidata

Beatriz Antonia Zenteno Quinteros

Ha sido aprobada por la comisión de Evaluación de la tesis como requisito para optar al grado de Doctora en Ciencias con mención en Física, en el examen de Defensa Privada de Tesis rendido el día 13 de noviembre de 2023.

Director de Tesis:

Dr. Pablo S. Moya ____________________

Comisión de Evaluación de la Tesis:

Dr. Víctor Muñoz ____________________

Dr. Mario Riquelme ____________________

Dra. Marina Stepanova ____________________

To my family.

"Family means nobody gets left behind or forgotten"

- Lilo & Stitch

Acknowledgments

We thank ANID, Chile, for the financial support provided for the development of this work, through the Doctoral National Scholarship N°21181965 and FONDECyT grant N° 1191351. We also acknowledge the support from the Katholieke Universiteit Leuven. These results were also obtained in the framework of the projects C14/19/089 (C1 project Internal Funds KU Leuven), G.0025.23N (FWO-Vlaanderen), SIDC Data Exploitation (ESA Prodex-12), Belspo project B2/191/P1/SWiM.

Publications

1. Bea Zenteno-Quinteros, Adolfo F. Viñas, and Pablo S. Moya. *Skew-kappa Distribution Functions and Whistler Heat Flux Instability in the Solar Wind: The Core-strahlo Model.* The Astrophysical Journal, 923(2):180 (2021).
2. Bea Zenteno-Quinteros and Pablo S. Moya. *The Role of Core and Strahlo Electrons Properties on the Whistler Heat-Flux Instability Thresholds in the Solar Wind.* Frontiers in Physics, 10:910193 (2022).
3. Bea Zenteno-Quinteros, Pablo S. Moya, Marian Lazar, Adolfo F. Viñas, and Stefaan Poedts. *Interplay between Anisotropy- and Skewness-driven Whistler Instabilities in the Solar Wind under the Core–Strahlo Model.* The Astrophysical Journal, 954(2):184 (2023).

Contents

Abstract

Electron velocity distribution functions (eVDFs) in the solar wind exhibit energetic tails and magnetic field-aligned skewness, attributed to secondary populations such as the halo and strahl. Temperature anisotropy is also a commonly observed suprathermal feature. Both skewness and anisotropy can provide energy for the excitation of electromagnetic perturbations through the whistler heat flux instability (WHFI) and the whistler-cyclotron instability, potentially altering the plasma state through wave-particle interactions. The WHFI, in particular, is believed to play a crucial role in regulating electron heat flux in the solar wind. In this work, we introduce a novel approach to model the solar wind eVDF: the Core-Strahlo (CS) model. This representation combines a bi-Maxwellian core and a suprathermal *strahlo*, modeled by a skew-Kappa distribution and representing the halo and strahl electrons using a unified description. We demonstrate that the CS model effectively reproduces key characteristics of the solar wind eVDFs, with the advantage of controlling skewness through a single parameter, δ. Using linear kinetic theory and considering small skewness, we conduct a comprehensive stability analysis of the parallel-propagating whistler mode and establish stability threshold conditions for comparison with observational data.

We show that plasma states with distinct WHFI stability levels may exhibit identical electron heat flux values, $q_{\parallel e}$. Therefore, systems with high $q_{\parallel e}$ values can be

stable enough, so that the WHFI may not be able to effectively modify electron heat flux values through wave-particle interactions. Consequently, skewness (a kinetic property of the eVDF) emerges as a better indicator of instability compared to the heat flux parameter (a plasma macroscopic quantity). Our study further investigates anisotropic cases, revealing that the strahlo anisotropy is a more efficient source of free energy for destabilizing the whistler mode compared to field-aligned skewness. This suggests a greater role of anisotropic suprathermal populations in processes governed by wave-particle interactions. We hope this study will motivate the development of theoretical works exploring the dynamics of the halo and strahl using a unified description. This approach could be especially valuable for addressing the interaction between these populations as they move away from the Sun. Lastly, we expect our results to find validation through electron measurements obtained from current and upcoming solar wind missions.

Resumen

Las funciones de distribución de velocidad de electrones (eVDF, por sus siglas en inglés) en el viento solar muestran colas energéticas y asimetría alineada con el campo magnético, atribuidas a poblaciones secundarias como el halo y el strahl. La anisotropía de temperatura también es una característica supratérmica comúnmente observada. Tanto la asimetría como la anisotropía pueden proporcionar energía para la excitación de perturbaciones electromagnéticas a través de la inestabilidad whistler flujo de calor (WHFI) y la inestabilidad whistler-ciclotrón, potencialmente alterando el estado del plasma mediante interacciones onda-partícula. En particular, se cree que la WHFI desempeña un papel crucial en la regulación del flujo de calor de electrones en el viento solar. En este trabajo, presentamos un nuevo enfoque para modelar la eVDF del viento solar: el modelo Core-Strahlo (CS). Esta representación combina un *core* bi-Maxwelliano y un *strahlo* supratérmico, modelado con una distribución Kappa asimétrica, el cual representa a los electrones del halo y el strahl usando una descripción unificada. Demostramos que el modelo CS reproduce de manera efectiva las características clave de las eVDF del viento solar, con la ventaja de controlar la asimetría a través de un solo parámetro, δ. Utilizando teoría cinética lineal y considerando una asimetría pequeña, realizamos un análisis exhaustivo de la estabilidad del modo whistler de propagación paralela y establecemos condiciones de umbral de estabilidad para su comparación con datos observacionales.

Mostramos que estados con distintos niveles de estabilidad a la WHFI pueden exhibir valores idénticos de flujo de calor electrónico, $q_{\parallel e}$. Por lo tanto, sistemas con valores elevados de $q_{\parallel e}$ pueden ser lo suficientemente estables como para que la WHFI no pueda modificar efectivamente los valores del flujo de calor electrónico a través de interacciones onda-partícula. Como resultado, la asimetría (una propiedad cinética de la eVDF) surge como un mejor indicador de inestabilidad en comparación con el parámetro de flujo de calor (una cantidad macroscópica del plasma). Nuestro estudio investiga además casos anisotrópicos, revelando que la anisotropía del strahlo es una fuente de energía libre más eficiente para desestabilizar el modo whistler en comparación con la asimetría alineada al campo. Esto sugiere un papel más importante de poblaciones supratérmicas anisotrópicas en procesos gobernados por interacciones onda-partícula. Esperamos que este estudio motive el desarrollo de trabajos teóricos que exploren la dinámica del halo y el strahl utilizando una descripción unificada. Este enfoque podría ser especialmente valioso para abordar la interacción entre estas poblaciones a medida que se alejan del Sol. Por último, esperamos que nuestros resultados sean validados mediante mediciones de electrones obtenidas en las misiones espaciales actuales y futuras del viento solar.

Chapter 1

Introduction

Since the 1940s, the study of plasma has been a rapidly growing field in both theoretical and experimental physics due to its prevalence in the universe. Plasma, colloquially known as the fourth state of matter, is an ionized gas characterized by its quasi-neutral nature and collective behaviors. Remarkably, it constitutes 99% of the visible matter in the universe [1], manifesting at various spatial and temporal scales. It appears in astrophysical plasmas such as accretion disks and active galactic nuclei [2–5], space plasmas like the interplanetary medium and planetary magnetospheres [6, 7], and laboratory plasmas, including inertial confinement devices and tokamaks [8–10]. The properties and behaviors of plasma systems differ significantly from those of normal gases due to the influence of long-range electromagnetic forces on the motion of their constituent particles. Understanding these distinct behaviors and their interactions with the environment is crucial, as it allows us to comprehend, explain, and predict processes observed in the universe, ultimately impacting life on Earth. A pertinent example is space weather, encompassing phenomena such as solar flares, coronal mass ejections, and geomagnetic storms. These events can disrupt satellite communications and affect power grids, underscoring the critical importance of studying and predicting them [11–13]. Furthermore, examining the behavior of these systems enables the development of various technological applications aimed at improving our quality of life, ranging from nuclear fusion and plasma medicine to plasma-based environmental remediation techniques [14–19].

While plasma is prevalent in the visible universe, it is relatively rare on Earth's surface, prompting us to look beyond our planet towards outer space to find natural occurrences of plasma. In our nearby celestial neighborhood, the solar system offers numerous examples. For instance, the Sun is a vast sphere of plasma [20]. Phenomena such as the solar wind and the ionosphere also involve plasmas [21, 22]. Trapped plasma exists within the Earth's magnetosphere as well [23]. Given their proximity to Earth, space plasmas can be explored through satellites and space probes, serving as our natural laboratory to study and understand the properties and processes inherent to such systems. Currently, a significant fleet of satellites is actively exploring the solar system and collecting invaluable data for the scientific community. Notable missions include THEMIS, WIND, and more recently, Parker Solar Probe and Solar Orbiter. Furthermore, space plasmas are generally immersed in macroscopic magnetic fields, which can originate in the Sun or from planetary sources. This is a notable characteristic as these magnetic fields can have a significant influence on the behavior of these plasma systems [24–28].

Another crucial feature of these magnetized space systems is their tendency to exist out of thermal equilibrium due to the low collision frequency among their constituent particles. Coulomb collisions are an efficient mechanism for relaxing particle populations to thermodynamic equilibrium, where the distribution functions reduce to Maxwellian profiles. Consequently, in non-collisional systems, particle velocity distributions can deviate from that profile and develop nonthermal features, representing free energy within the system [29–34]. In this non-collisional regime, other processes become important for the dynamics, as the free energy present in these out-of-equilibrium states has the potential to trigger electromagnetic or electrostatic radiation in the plasma. We refer to this process as “instability” [35–38]. The resulting waves and fluctuations can interact with the charged particles, modifying the plasma state. These interactions may facilitate the relaxation of the plasma to more stable states through non-collisional processes known as wave-particle interactions [39–42]. A fundamental challenge in plasma physics is understanding the excitation and relaxation of micro-instabilities in these weakly collisional plasmas, and how these phenomena regulate, through kinetic processes such as wave-particle interactions, the state of near equipartition of energy between electromagnetic turbulence and particles, as well as the properties of the plasma and macroscopic parameters.

The solar wind is a highly non-collisional plasma ejected from the solar corona into the interplanetary medium, primarily consisting of electrons, protons, and alpha particles [43]. It is widely acknowledged that this dynamic medium often exists in nonthermal states, especially evident in the high-energy tails observed in electron and ion velocity distributions [44–47]. Moreover, the velocity distributions of solar wind electrons exhibit other significant nonthermal features, with skewness along the interplanetary magnetic field, and a quasithermal core at lower energies being the most notable [48–50]. The suprathermal nature of solar wind electrons is typically characterized by three subpopulations: core, halo, and strahl. This is the most accepted interpretation of solar wind electrons and is supported by numerous observational reports [51–57]. The dense quasi-thermal core component is usually observed at low energies in electron distributions and is well-described by bi-Maxwellian functions. In contrast, at higher energies, halo electrons enhance the power-law tails of the distributions and are best modeled by bi-Kappa functions. Lastly, the strahl population is a magnetic field-aligned beam that becomes more prominent in fast winds and closer to the Sun [58–62]. The strahl gives the electron distribution its distinctive skewness, a characteristic that is usually emulated in theoretical models considering a drifting anti-sunward distribution. The skewness in the electron distribution provides free energy to the system for the excitation of different instabilities contingent on plasma parameters [63–66]. These skewness-driven instabilities, also receive the name of electron heat flux instabilities (HFIs), as the skewness gives the electron distribution a non-zero macroscopic heat flux moment. They have been extensively discussed in the literature, as they are believed to be responsible for the non-collisional self-regulation of electron heat flux below the collisional limit in the solar wind [65–75].

There is ample observational evidence indicating that the electron heat flux in the solar wind cannot be fully explained by the collisional Spitzer-Härm theory [76]. While this model adequately describes the heat flux in slow solar wind conditions, it often predicts higher values than those observed at 1 astronomical unit from the Sun [33, 70]. This discrepancy has been a subject of investigation for decades. For instance, studies have attempted to reconcile this disparity by empirically reducing thermal conductivity to reproduce the observed heat flux values [77]. Additionally, theoretical models have been proposed to explore various physical mechanisms that could potentially regulate the electron heat flux through non-collisional processes [34, 78, 79]. The most widely accepted mechanism to explain the suppression of electron heat flux values below those predicted by the collisional transport model involves non-collisional regulation through kinetic processes of wave-particle interactions [80–82]. The primary candidates for this process are the electron HFIs, due to the close relationship between the electron heat flux and skewness [63, 65, 83]. Among these skewness-driven instabilities, the excitation of the whistler mode of the electron cyclotron branch, known as the whistler heat flux instability (WHFI), has been frequently cited as one of the most probable non-collisional mechanisms regulating the electron heat flux in the solar wind [68, 69, 72, 73]. However, the dominant wave mode is still under debate, and recent works even suggest that it may not be possible to identify a single instability as the primary non-collisional mechanism [66]. Thus, studies regarding the regulation of electron heat flux in the solar wind should consider the interplay and/or succession of different instabilities [84].

It is crucial to highlight that measurements in the solar wind consistently demonstrate that the kinetic temperature (T) of electron populations is not isotropic [48, 53, 54, 85, 86]. Temperature anisotropy, denoted as $\mu = T_\perp / T_\parallel \neq 1$ (where $\parallel$ and $\perp$ refer to directions relative to the local magnetic field), represents an additional source of free energy in the system, capable of exciting electromagnetic radiation. This anisotropy can manifest not only in the suprathermal populations but also in the core electrons. Instabilities triggered by temperature anisotropy have been extensively investigated [87–96]. For anisotropic electrons with $\mu > 1$, dispersion and stability theories predict two instabilities: the mirror and whistler-cyclotron instability (WCI), while electrons with opposite anisotropy, $\mu < 1$, may trigger firehose instabilities, both periodic and aperiodic [97–102]. Therefore, given the significant role that temperature anisotropies play in kinetic processes, it is crucial to incorporate anisotropic scenarios ($\mu \neq 1$), alongside skewness, when analyzing the impact of HFIs on the dynamics of the solar wind electron population. This consideration holds special importance in studying the non-collisional regulation of electron heat flux, offering a more realistic understanding of the role played by HFIs and WCIs in this process.

The debate regarding the primary heat transport mechanism in the solar wind remains ongoing. Numerous theoretical and observational studies have aimed to assess the significance of HFIs in the non-collisional regulation of electron heat flux in the solar wind. Observational studies primarily focus on comparing measurements of the normalized electron heat flux macroscopic moment with analytical expressions of marginal stability thresholds for electron HFIs [64, 70, 103–105]. Theoretical investigations using linear and quasilinear approximations, as well as particle simulations, have also addressed this issue [63, 72, 73, 75, 83, 106, 107]. However, conducting such theoretical studies requires accurately modeling the electron velocity distribution function (eVDF). These eVDF models typically employ a linear combination of various functions, primarily bi-Maxwellian or Kappa distributions, in an attempt to replicate observations and mimic the nonthermal characteristics exhibited by electron subpopulations, namely, the quasithermal core, halo, and strahl. Among these models, the most widely considered approach involves the superposition of two drifting bi-Maxwellian distributions (typically representing the core and strahl), allowing for a skewed distribution function [66, 68, 69, 72, 73]. More realistic models have also been employed to describe the eVDF in the solar wind, using combinations of bi-Maxwellian and bi-Kappa distributions to accurately reproduce the observed high-energy tails (the halo) [65, 71, 92]. Additionally, more exotic distributions have been utilized to model the suprathermal electron population. By employing ad-hoc mathematical expressions, these models can adequately represent electron properties [95, 108–110].

In this thesis, we present a novel heuristic model for solar wind electrons called the Core-Strahlo (CS) model. This model effectively captures the behavior of a core-halo-strahl representation using just two subpopulations: a bi-Maxwellian core combined with a modified Kappa distribution that introduces skewness. This skew-Kappa function represents the suprathermal features of both the halo and strahl electrons in a single skewed distribution. It was initially proposed by Beck [111] in the context of fluid turbulence analysis. In the original derivation, the author demonstrated that the asymmetry of the distribution is correlated with the level of turbulence in the medium, quantified by the Reynolds number. Remarkably, recent research has confirmed the validity of this relationship for plasma systems as well [112]. This unified description of the observed energetic tails and skewness in the eVDF provides an alternative way to model solar wind electrons, especially beneficial for theoretical studies of instabilities, as it reduces the parameter space to be analyzed. Furthermore, the combined description of halo and strahl using a single function may enhance our understanding of the interaction between these two electron populations in the expansion of the solar wind throughout the heliosphere. This is because the halo is widely believed to form through pitch angle scattering of strahl electrons by self-generated instabilities [58, 59, 109, 113].

In the first part of this work, we aim to comprehensively explore the properties of the CS model and assess its applicability to solar wind electrons. Our goal is to establish the CS model as a robust and suitable representation of the eVDF in the solar wind. In the second part, we focus on utilizing the CS model to describe the solar wind electron population and study the effect of suprathermal electrons on the excitation of the parallel-propagating WHFI using kinetic theory applied to non-collisional and magnetized plasmas. We aim to gain insights into how this instability contributes to regulating the final state of the plasma through wave-particle interactions. Additionally, we aim to explore the interplay between skewness and anisotropy as sources of free energy within the system. By considering both suprathermal features, we seek to develop a more accurate and realistic understanding of the WHFI and its effects on the dynamics of the solar wind electron population. We propose these objectives with the intention that the obtained results will lead to a simplified description of the eVDF skewness, thus simplifying theoretical works regarding electron dynamics in the solar wind.

To effectively explore the ideas outlined, this thesis is structured as follows: In Chapter 2 we provide an overview of the basic properties of the Sun and the solar wind. We offer crucial information about solar wind electrons from observational and theoretical perspectives. Further, we examine electron skewness- and anisotropy-driven instabilities and elaborate on key definitions related to the electron heat flux, including its profile in the solar wind. In Chapter 3 we introduce the Core-Strahlo model. We thoroughly analyze the skew-Kappa function and propose it as a novel distribution function to describe both the halo and strahl suprathermal populations. We conduct a comprehensive analysis of the properties and key parameters of the CS model, establishing its applicability for the solar wind. Then, in Chapter 4, we utilize the CS model to describe the electron population in the solar wind. Using linear kinetic theory, we conduct a rigorous stability analysis of the parallel propagating whistler mode, driven unstable by the skewness of the electron distribution. Additionally, we investigate the influence of various plasma parameters on the excitation of this instability, covering all relevant parameter space in the isotropic case. In Chapter 5 we systematize the analysis from the previous chapter to obtain the marginal stability thresholds of the WHFI and their dependence on all relevant plasma parameters. Furthermore, we provide analytical expressions and best-fit parameters for these thresholds to facilitate a convenient comparison with observational data. In Chapters 6 and 7 we extend the linear stability analysis to consider skewness and anisotropy as sources of free energy in the eVDF. Finally, in Chapter 8 we summarize and discuss the main results in the context of the solar wind, providing the conclusions of this work. We also explored potential ideas for future research and possible improvements that can enhance and expand upon the current work.

Chapter 2

Solar wind electrons

2.1 The Sun

The Sun, our nearest star, holds a central position in the solar system. This massive sphere of hot plasma was formed approximately 4.65 billion years ago. Its energy is sourced from nuclear reactions occurring at its core, generating a continuous stream of power. This energy radiates out into space, making the Sun the primary energy source for our solar system and a vital factor for life on Earth. Given the crucial roles of the Sun in supporting life and human society, the study of this celestial body has been a fascinating pursuit throughout history, dating back to ancient times. Today, the Sun offers us a natural laboratory to comprehend the fundamental mechanisms governing stars and the complexities of other stellar systems [114, 115].

The Sun primarily consists of hydrogen and helium, along with smaller amounts of heavier elements like oxygen and carbon. It is positioned at an average distance of about 1.5×10^8 km from Earth, a distance defined as one astronomical unit (au). The Sun has a mass of approximately $M \approx 2 \times 10^{30}$ kg, roughly 330,000 times that of Earth, while its radius, approximately $R \approx 7 \times 10^5$ km, is nearly 109 times the Earth's radius. Maintaining its nearly spherical shape, the Sun's equilibrium is sustained by a delicate interplay known as hydrostatic equilibrium: gravitational force pulls inward, attempting to collapse the star, while internal gas pressure pushes outward, counterbalancing this force [115, 116]. Furthermore, the interior of the Sun can be broadly classified into three distinct regions. Moving outward from its center, we encounter the core, followed by the radiative zone, and the convective zone. The solar core constitutes the hottest region of the Sun, reaching temperatures of up to 1.5×10^7 K. It is both dense and hot enough to facilitate an ongoing process of nuclear fusion, where hydrogen is transformed into helium through the proton–proton chain reaction. Adjacent to the core lies the radiative zone, characterized by energy transport through radiation, where photons carry the energy generated in the core. Subsequently, we encounter the convective zone, where the density is low enough to allow convection. This results in the Sun's energy moving outward, aided by large convection cells. As we approach the surface of this zone, the temperature drops to around 5.7×10^3 K [117, 118].

After the convective zone, we encounter the highly dynamic solar atmosphere, which is the optically thin region of the Sun. The solar atmosphere is further divided into three layers. The innermost layer is the photosphere, constituting the visible surface of the Sun. It marks the upper boundary of the convective zone and showcases a granular pattern resulting from the underlying convection cells. Next, encircling the photosphere, is the chromosphere, with a temperature of approximately 10^4 K. This layer is distinguished by its reddish hue, attributed to the H-alpha emission line of hydrogen. However, it is not visible to the naked eye against the brilliant background of the photosphere [115, 118]. Lastly, we encounter the solar corona, the outermost layer of the solar atmosphere. It consists of tenuous, hot plasma that extends for millions of kilometers into space. The corona is notably characterized by its exceptionally high temperatures, exceeding 10^6 K. From the solar corona, material evaporates into the interplanetary medium, giving rise to the solar wind. Despite its significance, the exact process that heats the corona remains a mystery, marking one of the primary open questions in the field of solar physics [117, 119].

It is important to emphasize that the Sun is a highly variable magnetized star. This characteristic arises from its intricate magnetic field, a result of convection and differential rotation within the Sun's internal dynamo. This ever-changing magnetic field drives solar activity, manifested through phenomena like sunspots or solar prominences [27, 115, 120, 121]. The fluctuations in the number of sunspots on the Sun's photosphere define the 11-year cycle of solar activity, known as the solar cycle. Additionally, energetic events such as coronal mass ejections and solar flares are also encompassed within solar activity. These high-energy occurrences significantly influence space weather and have the potential to impact Earth's space environment and our technological systems [13].

2.2 The solar wind

As discussed in the previous section, the hot plasma enveloping the Sun within the solar corona expands into the interplanetary space, giving rise to the phenomenon we know as the solar wind. This solar wind is a supersonic flow of charged particles ejected from the corona, propelled by the pressure difference between the corona and the interplanetary medium [115]. This dynamic mechanism drives the solar plasma outward radially, enabling it to break free from the grasp of solar gravity. The solar wind primarily consists of electrons and protons, with alpha particles contributing to a lesser extent, alongside trace amounts of various heavier ion species [122, 123]. This plasma permeates the interplanetary space, shaping a region that envelops the Sun known as the Heliosphere. This expansive domain extends well beyond the planetary orbits. The Heliopause marks the boundary of the Heliosphere, where the solar wind interfaces with the interstellar medium. Furthermore, the solar wind carries the Sun's magnetic field, which tends to remain frozen within the flowing plasma due to its high electrical conductivity. This magnetic field is subsequently transported outward into the heliosphere, where it is recognized as the heliospheric magnetic field (HMF). Moreover, owing to solar rotation, the field lines begin to spiral as they move away from the Sun, forming distinctive Archimedean spirals.

The solar wind is not a steady phenomenon, and its key parameters such as density, speed, temperature, and strength and orientation of the embedded magnetic field vary with time [117]. One of the most common and widely used ways to categorize this variability of the solar wind is in terms of its velocity, as it travels through the heliosphere. Accordingly, the solar wind can be primarily classified into two types. The first one is the slow solar wind, characterized by bulk velocities ranging between approximately 300 km/s and 500 km/s. The other type is the fast solar wind, which exhibits bulk velocities between about 500 km/s and 800 km/s. Observations reveal that during periods near solar minimum, the fast solar wind emerges from high heliospheric latitudes, while the slow solar wind originates at lower heliospheric latitudes near the solar equator. However, this distinct boundary between fast and slow wind is significantly influenced and modified by the solar cycle. During times of solar maximum, the strong correlation between the occurrence of fast and slow wind streams and heliographic latitude disappears. Different wind streams are thought to originate from distinct sources within the solar corona. The prevailing consensus suggests that the fast solar wind is mainly associated with polar coronal holes, regions on the solar corona where magnetic field lines are open. In contrast, the slow solar wind is generally believed to emanate from the complex and dynamically changing coronal streamers, characterized by closed magnetic lines. Nevertheless, establishing a clear connection between these wind types and their specific solar origins remains an ongoing area of research [124–126].

In addition to differences in speed, the fast and slow solar winds exhibit further distinguishing characteristics. The slow-speed solar wind tends to be cooler and denser, while the high-speed solar wind is hotter and more tenuous [117]. These alternating fast and slow solar wind streams eventually intersect as they travel through the heliosphere. This collision leads to the formation of a compression zone at the interface between the high-speed wind and the comparatively slower upstream plasma. These structures adopt a spiral shape that co-rotates with the Sun, earning them the designation of "corotating interaction regions". Further, as the solar wind approaches Earth, its constituent particles experience deceleration and deflection due to Earth's magnetic field. This effect gives rise to a protective region encircling our planet known as the magnetosphere. This region acts as a barrier and effectively demarcates the terrestrial geomagnetic field from the HMF and impinging solar wind plasma. Additionally, the pressure exerted by the solar wind significantly distorts the Earth's dipolar magnetic field. In the dayside region, magnetic field lines become compressed, while on the night side, the magnetic field stretches out, forming an elongated magnetotail. The formation of a magnetosphere region is not exclusive to Earth; it is replicated in the near-space environment of other celestial bodies, with a sufficiently strong internally-generated magnetic field, such as Jupiter and Mercury.

The solar wind is significantly influenced by solar activity, transmitting the effects of solar variability throughout the Heliosphere and impacting planets. High-energy solar phenomena, such as coronal mass ejections, solar flares, and solar energetic particles, are known to trigger geomagnetic disturbances. These disturbances can have adverse effects on modern society and human life. The interaction of the solar wind with Earth's magnetic field, and the influence of solar variability on space weather, represent important and extensively studied areas of research in space plasma physics. This research is particularly critical as our lives become increasingly dependent on space-borne and ground-based technological systems [12, 115, 127, 128].

2.3 Solar wind electrons

The solar wind is characterized by being a weakly collisional medium. Collisions between charged particles, known as Coulomb collisions, play an important role in transferring energy and momentum in fully ionized plasmas, where the behavior is governed by long-range electromagnetic forces. However, for solar wind electrons at 1 AU, the mean free path for these Coulomb collisions is on the order of 10^8 km, comparable to the typical length scales of the system [34, 53]. Coulomb collisions constitute an efficient mechanism for driving and maintaining plasma locally at thermodynamic equilibrium. This state is characterized by velocity distribution functions adopting a Maxwellian profile. Consequently, collisions are insufficient to drive particle populations toward equilibrium in such systems with low Coulomb-collisionality. Thus, the velocity distributions of particles may exhibit deviations from the standard Maxwellian, leading to the development of what we refer to as nonthermal or suprathermal features.

Measurements of solar wind particle distributions confirm that this system is generally out of thermodynamic equilibrium. The nonthermal characteristics of both the electron and ion constituents of the solar wind plasma have been extensively documented in observational studies. Notable features systematically observed in electron velocity distributions include power-law high-energy tails and magnetic field-aligned skewness, along with a quasithermal core at low energies [47, 48, 50]. Figure 2.1 presents examples of observed electron distributions, highlighting the suprathermal nature of this population, after Pierrard et al. [129]. We observe typical electron velocity distributions measured by the electrostatic analyzer of the 3DP instrument aboard the WIND spacecraft at 1 AU from the Sun. Left and right panels show a distribution obtained under slow and high-speed conditions, respectively. The top panels display parallel (solid line) and perpendicular (dotted line) cross-sections of the observed velocity distributions, and the bottom panels show isocontours in the plane of normalized velocities parallel and perpendicular to the interplanetary magnetic field. From the 1D plots, we clearly observe the quasithermal core and the enhanced tails of the distribution. Additionally, both plots distinctly display the skewness of the distribution, which is more prominent in the fast solar wind distribution shown in panel 2.1(b).

The non-equilibrium electron distributions have been empirically interpreted in terms of three distinct subpopulations: core, halo, and strahl. This framework is widely accepted for characterizing the observed electron distributions and their suprathermal attributes in the solar wind [51–57]. Firstly, we identify the quasithermal core subpopulation, typically measured at low energies (up to a few tens of eV), which constitutes the majority of solar wind electrons, accounting for over 90% of the total number density. This dominant and dense population is often best described by bi-Maxwellian velocity distributions. However, a recent approach utilizing bi-self-similar functions has emerged to model the core segment of observed electron distributions in interplanetary shocks near 1 AU. This approach demonstrates that

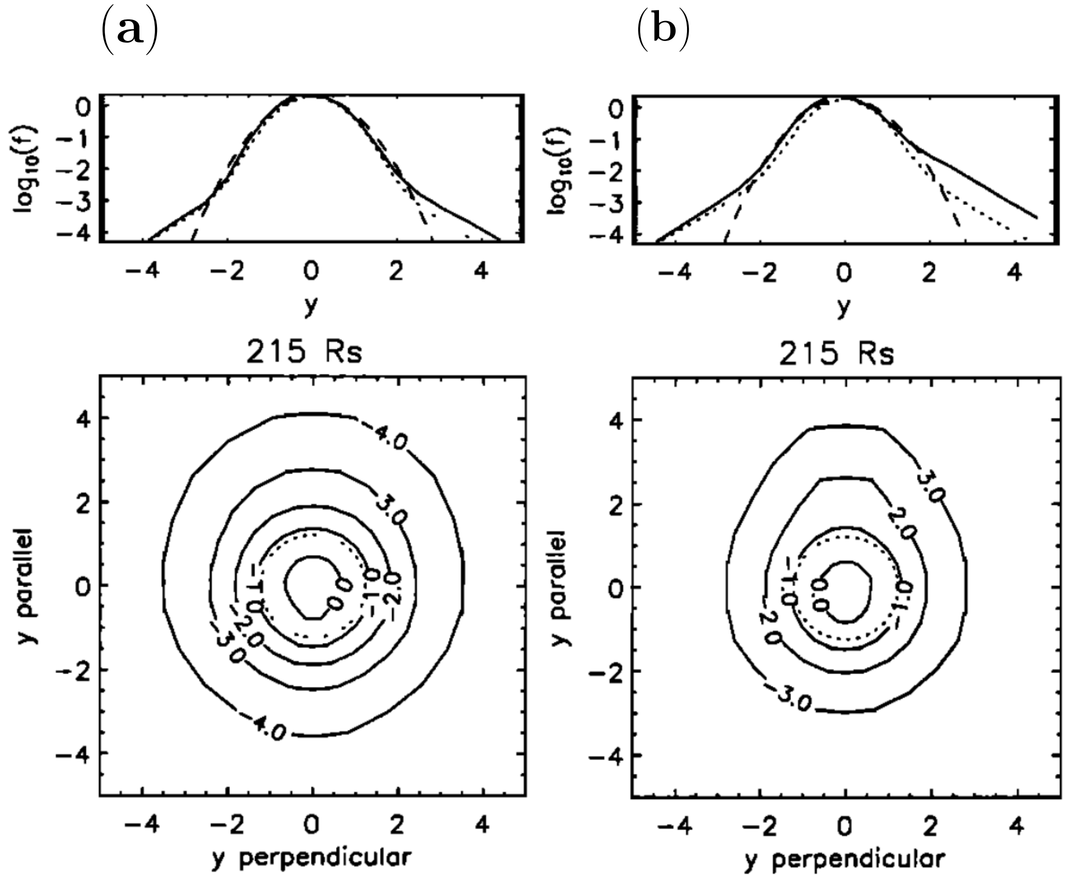

Figure 2.1: Examples of typical electron velocity distributions measured by the electrostatic analyzer of the 3DP instrument aboard the WIND spacecraft at 1 AU for low-speed (left) and high-speed solar wind (right). After Pierrard et al. [129].

a self-similar velocity distribution function provides a more accurate description of the core subpopulation compared to a standard bi-Maxwellian [56, 57]. Next, we have the halo subpopulation, observed at higher energies, often ranging up to a few keV. These halo electrons are distributed across all pitch angles and are responsible for the characteristic power-law energetic tails in the electron distribution. Historically, bi-Maxwellian functions with lower amplitudes and higher temperatures than those of the core were commonly utilized to perform fittings and emulate the energetic tails in the early works [48, 130]. However, more recent studies have shown that bi-Kappa distribution functions provide a better description of this specific subpopulation [58, 59]. Lastly, the strahl subpopulation constitutes a suprathermal beaming component, primarily moving in the antisunward direction and aligned with the magnetic field. The presence of strahl electrons imparts the characteristic skewness to the electron distributions, which is more pronounced in the fast solar wind and closer to the Sun. While efforts have been made to provide an analytical model to fit this observed population [59, 131], there is currently no consensus regarding such an analytical form. The most commonly used approach for incorporating the skewness into theoretical models is by considering drifting distributions.

Figure 2.2(a) schematically illustrates these three subpopulations in velocity space, after Verscharen et al. [132]. The total electron distribution is composed of the quasithermal core (blue), suprathermal halo (green), and electron strahl (red). On the other hand, Figure 2.2(b) provides a fitting example based on Helios I electron measurements, after Štverák et al. [53]. The solid line in the plot represents the combination of the core fit, achieved using a bi-Maxwellian (dashed line), and the halo fit, modeled using a bi-Kappa function (dash-dotted line). Additionally, the strahl population is distinctly visible. These fits using analytical models allow us to obtain and estimate fundamental parameters for these electron subpopulations, such as number density, kinetic temperatures, and heat flux, enabling exploration of their variation throughout the heliosphere. These analyses also reveal another suprathermal feature of the electron population: temperature anisotropy, observed in both the quasithermal core and the suprathermal population [54, 58, 86].

To conduct theoretical and numerical studies on solar wind electron dynamics, modeling the electron velocity distribution function (eVDF) is crucial. Over the years, several models have emerged to describe the physics of solar wind electrons. Typically, these eVDF models utilize a linear combination of different functions to depict

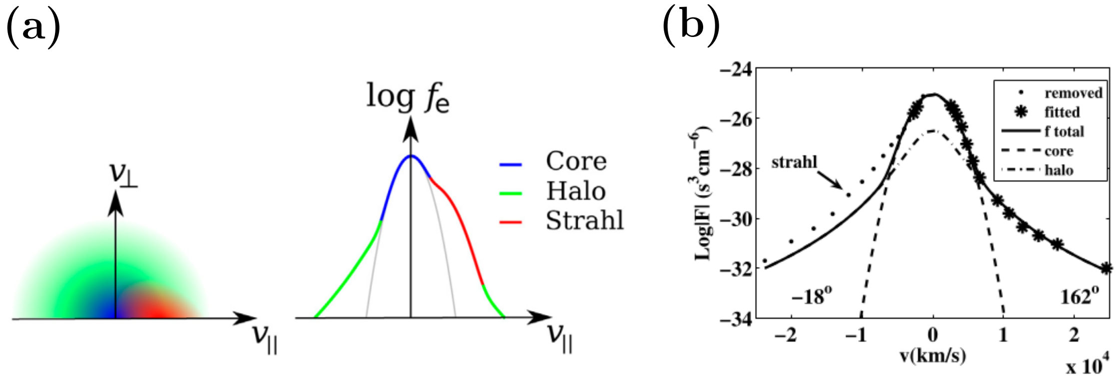

Figure 2.2: (a) Schematic of a typical electron distribution function in the solar wind and its three subpopulations: quasithermal core (blue), halo (green), and strahl (red). After Verscharen et al. [132] (b) Example of fitted eVDF from Helios measurements. After Štverák et al. [53].

the electron population and theoretically emulate the observed nonthermal characteristics. The most commonly used distributions for this purpose are the bi-Maxwellian and bi-Kappa distributions, known for providing the best fits for the data [65, 66, 68, 69, 71–73, 92]. One widely employed approach is the core-strahl model, which involves superimposing two bi-Maxwellian functions. A relative drift between them is included to emulate the skewness provided by the strahl electrons. While this model may appear simplistic and not fully capture the features of the system, it is an effective approach for studying phenomena where the tails of the distribution are not relevant. Another widely used description is the core-halo model. This model combines a bi-Maxwellian for the core and a Kappa distribution for the halo, allowing an accurate description of high-energy tails, and providing a more realistic representation of the solar wind electrons. Sometimes, a drift between the subpopulations is introduced to emulate skewness and incorporate the strahl population into the analysis. Although this approach is more realistic, its usage introduces an additional parameter into the analysis, the spectral index κ.

In recent years, studies have explored less conventional functions to model the electron subpopulations. For instance, in a theoretical analysis of electron heat flux inhibitions by Vasko et al. [110], the authors described the strahl population using a bi-Maxwellian function supplemented with extra parameters to modify its symmetry. A study by Horaites et al. [106] performed a kinetic stability analysis describing the strahl electrons with an analytical function derived from the collisional kinetic equation. These innovative functions are notable for their inherent asymmetry. Thus, the skewness of the electron distribution is not solely emulated by considering a relative drift between distributions, allowing for a more nuanced representation. In this context, we can also mention the regularized Kappa distributions, which consist of a power-law term with a Maxwellian cutoff. This distribution has emerged to address the apparent unphysical limitations associated with the standard Kappa functions, such as diverging velocity moments [95, 108]. To our knowledge, most of these proposed models have not been observationally tested. However, the emergence of models utilizing alternative approaches to describe the suprathermality of the electron distribution indicates a growing interest in extending and diversifying the study of kinetic processes.

2.4 Electron-driven instabilities

In the previous section, it was detailed that weakly collisional plasmas, such as the solar wind, are characterized by being out of thermodynamic equilibrium. This is a result of the limited effect of Coulomb collisions on the dynamics of the system due to their infrequent occurrence. These nonthermal states are characterized by the presence of suprathermal features in the velocity distributions of the different plasma populations. For plasma systems in the non-collisional regime, other processes involving the emission of radiation become important, as these systems are composed of charged particles that can be influenced by electromagnetic fields in their dynamics. It is then said that the nonthermal characteristics represent free energy in these out-of-equilibrium states, which can be emitted in the form of electromagnetic or electrostatic radiation in the plasma. This excited radiation can interact with the charged particles of the plasma, leading to the exchange of energy and momentum through wave-particle interactions. As a result of these interactions, the energy of the system is redistributed, and this non-collisional process can reshape the particle distributions until the free energy, in the form of suprathermal features, is reduced or removed [42, 133]. Consequently, these processes may assist in the relaxation of plasma populations towards more stable states. In other words, the emitted radiation can act as a mechanism for the isotropization of the plasma, and notably, this process is entirely independent of Coulomb collisions.

In plasmas, the collective process of unstable radiation emission at kinetic scales is generally referred to as micro-instability. Depending on the population providing the free energy and the specific suprathermal feature involved, different normal wave modes can be excited, each with distinct dispersive properties. These properties can be further modified for the same wave mode based on other parameters characterizing the plasma state. Consequently, a wide variety of instabilities can be triggered in a plasma. Typically, the name given to an instability allows us to differentiate the suprathermal feature acting as the energy source and the triggered wave mode [133]. The primary approach to studying these plasma instabilities in the solar wind involves employing linear kinetic theory applied to non-collisional and magnetized plasmas. This framework can tell us under which plasma conditions the instabilities can be excited in a plasma system and facilitate the study of their properties. Through a linearization procedure of the Vlasov-Maxwell system of equations and assuming that the small amplitude fluctuations of the relevant quantities are plane waves, it is possible to obtain the dispersion relation $\omega = \omega(\mathbf{k})$, for the normal modes of the system, given by $\mathbf{E}(\mathbf{r}, t) = \mathbf{E}_\mathbf{k} \exp[i(\mathbf{k} \cdot \mathbf{r} - \omega(\mathbf{k})t)]$, where $\mathbf{E}_\mathbf{k}$ is the amplitude of the waves. Here, $\omega(\mathbf{k}) = \omega_r(\mathbf{k}) + i\gamma(\mathbf{k})$, where $\omega_r(\mathbf{k})$ is the wave frequency, and $\gamma(\mathbf{k})$ is the growth (or damping) rate, both functions of the wave vector $\mathbf{k}$. The amplitude of solutions to the linear dispersion equation that satisfy $\gamma > 0$ grow exponentially over time, and we refer to this case as instability. To obtain growing solutions with $\gamma > 0$, the dispersion equation must be solved based on distribution functions involving free energy [132–134].

In the case of these kinetic instabilities, when $\gamma(\mathbf{k}) > 0$ at least one plasma population is in resonance with the instability. This feature is traditionally quantified by the resonant terms ζ_j^m, which correspond to arguments of the plasma dispersion functions involved in the linear dispersion relation. When $|\zeta_j^m| \lesssim 1$, we have a resonant wave interaction with population j. In this case, there is a considerable number of particles satisfying the resonance condition shown in Eq. (2.1). Thus, it is said that population j is resonant with the wave, and particles moving with velocities that satisfy condition (2.1) are said to be in Landau ($m = 0$) or cyclotron ($m \neq 0$) resonance with the wave [42, 132, 133]:

$$\omega_r = k_\parallel v_\parallel - m\Omega_j \quad m \in \mathbb{Z}\,. \tag{2.1}$$

In the above expression, $\Omega_j = q_j B_0 / m_j c$ is the cyclotron frequency of population j, where q_j and m_j denote the charge and mass of the particles composing this population and B_0 is the magnitude of the background magnetic field of the magnetized plasma. Further, the subscript $\parallel$ indicates the direction along the magnetic field. While this linear framework can shed light on the conditions under which instabilities may arise in the plasma, a comprehensive analysis of their evolution over time and interactions with particles requires incorporating nonlinear effects into the treatment. Plasma particle simulations, quasilinear theory, and weak turbulence theory are well-known tools to achieve this purpose [73, 75, 83, 94, 135].

It is important to remember that the solar wind is a magnetized system. The magnetic field plays a role not only in the resonance process through the cyclotron frequency but also in defining a preferred direction in the system, generating an anisotropy in the response of the plasma to perturbations. Wave modes can propagate in any arbitrary direction with respect to the background magnetic field $\mathbf{B_0}$. Generally, waves with propagation angles parallel or perpendicular to $\mathbf{B_0}$ are mathematically easier to study for realistic solar wind scenarios. Furthermore, the background magnetic field defines a fundamental plasma parameter, quantifying the importance of magnetization in the dynamics of the system relative to the thermal energy of the plasma [136]. The beta parameter of population j, β_j, is defined as the ratio between the kinetic pressure and the magnetic pressure, and it is calculated using the following expression:

$$\beta_j = \frac{8\pi n_j k_B T_j}{B_0^2}\,, d \tag{2.2}$$

where k_B represents the Boltzmann constant, n_j is the number density and T_j is the kinetic temperature of population j. The plasma beta provides valuable information about the relative importance of thermal and magnetic effects on plasma behavior and the effectiveness of the magnetic field in confining the movement of plasma particles. Consequently, this parameter is crucial in assessing the significance of the magnetic field in triggering instabilities in the plasma. In general, as β decreases, more pronounced suprathermal features are needed to excite radiation [66, 68, 137].

In this study, our primary focus is on electron-driven instabilities, where radiation is triggered by the nonthermal characteristics of the electron population. These instabilities have been extensively investigated, primarily due to their potential role in constraining plasma observations related to electron heat flux and kinetic temperature anisotropies. Detailed analyses of these instabilities can be found in studies such as Gary [133] and Verscharen et al. [132]. Of particular interest for this work are the whistler heat flux instability, which is triggered by skew electron distributions, and the whistler-cyclotron instability, which is excited by anisotropic electron configurations that satisfy $T_{\perp e}/T_{\parallel e} > 1$. Both of these instabilities correspond to cyclotron-resonant instabilities of the electromagnetic fast-magnetosonic/whistler wave mode, and they exhibit maximum growth rates for parallel propagation $\mathbf{k} \times \mathbf{B_0} = 0$ [132, 133].

It is crucial to emphasize that in studies utilizing kinetic theory to investigate plasma instabilities, it is necessary to employ a model to describe the plasma populations. This enables the evaluation of the dispersion relation and prediction of possible wave activity resulting from nonthermal features. Most stability analyses use analytical models. Drifting bi-Maxwellian or bi-Kappa distributions are the most commonly employed functions. However, recent works have expanded this approach by allowing the use of arbitrary gyrotropic distribution functions defined numerically to solve the dispersion and stability properties of plasma instabilities [95, 138]. Furthermore, depending on the selected model to describe the populations, the same instability may differ either qualitatively or quantitatively in its dispersive properties. For example, in Shaaban et al. [65], the authors demonstrated that utilizing a drifting Kappa distribution instead of a drifting bi-Maxwellian to describe the suprathermal electron population in the solar wind resulted in a significantly more unstable WHFI. This enhancement is observed through increased growth rates and an expanded range of unstable wave numbers. Specifically, for the parameters used in their analysis, the maximum growth rate increased by almost five times for a Kappa function with $\kappa = 3$ compared to the maximum growth rate obtained with a bi-Maxwellian distribution (see Figure 6 in Shaaban et al. [65]). This result suggests that the power-law energetic tails are relevant to consider in the study of this instability in solar wind scenarios. Therefore, utilizing models that accurately capture the complexities of velocity distributions is necessary to obtain a realistic understanding of the influence and importance of different plasma instabilities in the solar wind.

2.5 Electron heat flux moment

The electron heat flux corresponds to a macroscopic quantity of the plasma, characterizing the thermal energy transport by electrons. It is defined such that $\mathbf{q_e} \cdot \hat{\mathbf{n}}$ quantifies the amount of thermal energy per unit area and unit time flowing across a surface whose normal points in the direction of the unit vector $\hat{\mathbf{n}}$. If we consider that the electron population is described by the distribution function f_e, then the heat flux macroscopic parameter is calculated as the third velocity moment of f_e according to:

$$\mathbf{q_e} = \frac{m_e}{2} \int (\mathbf{v} - \mathbf{U_e})^2 \; (\mathbf{v} - \mathbf{U_e}) \; f_e \, \mathbf{dv} \, . \tag{2.3}$$

Here, m_e represents the electron mass, and $\mathbf{U_e}$ is the electron drift velocity. It is important to note that the integral in Equation (2.3) evaluates to zero if the distribution function f_e is symmetric with respect to the drift velocity. In the solar wind, the electron population exhibits magnetic field-aligned skewness. Consequently, in general, the electron heat flux in the direction of the background magnetic field is nonzero ($q_{\|e} \neq 0$).

Recent observations have revealed that the collisional Spitzer-Härm transport model [76] cannot fully explain electron heat flux measurements in the solar wind. This model relates the electron heat flux to the electron temperature profile according to Equation (2.4), known as the Spitzer-Härm (SH) law, for a completely ionized gas where Coulomb collisions are relevant for the dynamics:

$$\mathbf{q_e} = -k_{SH} \nabla T \,. \tag{2.4}$$

In the above expression, k_{SH} is the thermal conductivity coefficient. In Bale et al. [70], it was demonstrated that the field-aligned electron heat flux at 1 AU from the Sun aligns with the SH model only up to a temperature Knudsen number of $K_n \sim 0.3$. This primarily corresponds to the slow solar wind. Beyond this point, the observed heat flux values are lower than those predicted by the SH law. The temperature Knudsen number K_n is defined as the ratio between the mean free path (λ_{fp}) and the temperature gradient scale (L_T). Figure 2.3, after Bale et al. [70], illustrates this critical behavior of the electron heat flux profile. The top panel shows the joint normalized distribution of the normalized parallel electron heat flux $q_{\|e}/q_0$, where q_0 represents the free streaming or saturation heat flux, and the temperature Knudsen number K_n. The bottom panel displays the distribution of data with K_n. The diagonal line in the top panel corresponds to the Spitzer–Härm relationship (2.4), which takes the following form in this parameter space [33]:

$$\frac{q_{\|e}}{q_0} \approx 1.07 \frac{\lambda_{fp}}{L_T} \,. \tag{2.5}$$

From the figure, it is evident that the SH relation is a reasonably good approximation, as the heat flux data closely follows Eq. (2.5) across a significant portion of its range. However, at approximately $\lambda_{fp} \simeq 0.28 L_T$, the measured data deviates from the SH line and flattens to a fixed value of $q_{\|e} \sim 0.29 q_0$. This is a well-known result, possibly implying the presence of non-collisional processes that are necessary for a comprehensive understanding of electron thermal energy transport in the heliosphere. It is important to note that for the calculation of L_T in this plot, the authors assumed that the electron temperature depends on the heliocentric distance following a power-law relation $T_e \propto r^{-\alpha}$ with $\alpha = 2/7$, value that ensures a constant conductive luminosity.

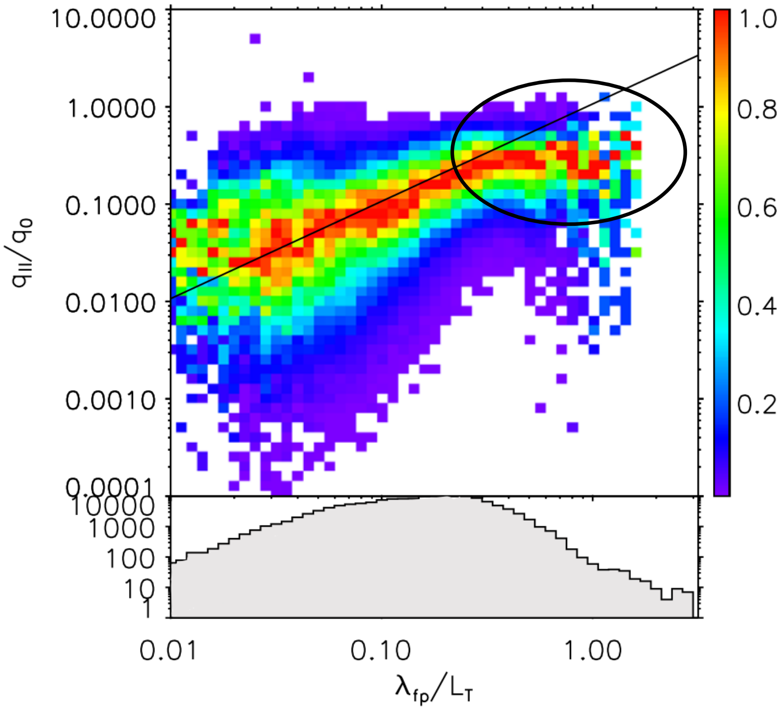

Figure 2.3: Top panel: joint normalized distribution of the normalized electron heat flux and the temperature Knudsen number. Bottom panel: distribution of data with the Knudsen number. After Bale et al. [70].

The Parker Solar Probe (PSP) has provided valuable insights to investigate this issue in the near-sun environment. Its initial observations conducted within 0.25 AU from the Sun reveal that the heat flux observations deviate significantly from the SH law, not conforming to this model for almost any range of the estimated Knudsen number (K_n) [104]. In Figure 2.4, after Halekas et al. [104], the authors present a 2D frequency distribution of the normalized heat flux and the temperature Knudsen number (K_n) for two values of the electron temperature exponent: $\alpha = 2/7$ (left) and $\alpha = 0.5$ (right), for the first two PSP orbits. The diagonal lines in both panels correspond to the SH relation (2.5). For $\alpha = 2/7$, the normalized heat flux remains nearly constant at $\sim 0.1 - 0.3$ for $K_n > 0.2$ and aligns with the SH limit for $0.1 < K_n < 0.2$. However, for a larger exponent $\alpha = 0.5$, which is more consistent with observational results, $q_{\|e}/q_0$ remains below the SH limit for all observed values of K_n. This trend also persists in the data collected during the fourth and fifth orbits. Here, the great majority of the observed heat flux values lie below the SH limit, irrespective of the assumed temperature exponent. Consequently, this data suggests that non-collisional mechanisms may play an even more substantial role closer to the Sun in shaping the electron heat flux profile.

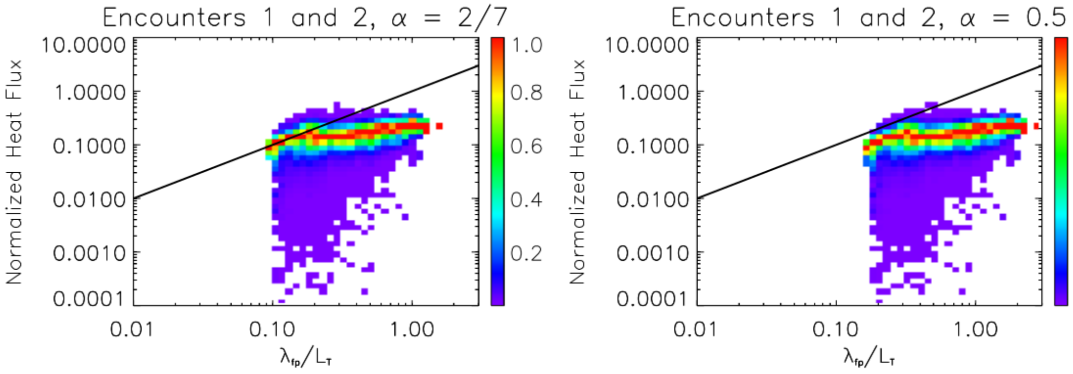

Figure 2.4: 2D normalized frequency distributions of the normalized heat flux and the Knudsen number K_n for the first two PSP orbits, considering for values of the electron temperature exponent: $\alpha = 2/7$ (left) and $\alpha = 0.5$ (right). After Halekas et al. [104].

The most accepted mechanism to explain this suppression of the heat flux values below the SH limit corresponds to kinetic processes of wave-particle interactions. Considering that the electron heat flux is closely related to the eVDF skewness, HFIs are the primary candidates to be the mechanism that self-regulates the heat flux and explains the observed profile in the solar wind [63, 65, 83]. Further, the whistler waves excited by the WHFI, have been the most extensively studied and frequently cited as a relevant non-collisional process, however, the dominant wave mode involved is still under debate [66, 67, 70, 107, 139].

In general, one of the primary methods to assess the importance of these HFIs in constraining the electron heat flux values in the non-collisional regime is to compare analytical marginal stability thresholds of the HFIs, obtained from theoretical linear stability works, with measurements of the electron heat flux moment in the solar wind [64, 70, 103–105]. An early example of this procedure can be found in Gary et al. [64], where the authors, using Ulysses electron observations, found qualitative agreement between the observable bounds of the heat flux data and the Alfvén heat flux instability threshold in the low beta regime and between the WHFI for higher beta values. Furthermore, in Bale et al. [70], the authors contrasted data obtained by the WIND spacecraft with theoretical threshold values for the whistler and magnetosonic instabilities. They concluded that for the dataset analyzed, the WHFI overconstrains the observations while the magnetosonic instability is more consistent in the non-collisional regime when $K_n > 0.3$ and the plasma beta is large. In addition, in Halekas et al. [104], the authors used data provided by PSP at heliocentric distances between 0.125 and 0.25 AU from the Sun. They concluded that the observed heat flux dependence on plasma beta is consistent with theoretical thresholds associated with oblique whistler waves generated via the fan instability [110]. In contrast, in Cattell et al. [105], authors showed that whistler waves are extremely rare inside $\sim$0.13 AU and the heat flux vs beta relationship is not constrained by the heat flux fan instability this close to the Sun. The debate regarding the non-collisional mechanisms shaping the electron heat flux profile in the solar wind is ongoing. Consequently, a comprehensive understanding of the HFIs in solar wind-relevant scenarios is crucial to evaluate their significance in this phenomenon.

Chapter 3

The Core-Strahlo model [†]

To characterize the distribution function of solar wind electrons, denoted as f_e, we employ a superposition of two distinct subpopulations, as outlined in Equation (3.1). The first subpopulation is described by a bi-Maxwellian distribution (f_c), shown in Equation (3.2), representing the core electrons. The second subpopulation is modeled using a skew-Kappa function (f_s), to describe both the halo and strahl electrons. Henceforth, we will refer to this subpopulation as the *strahlo* and this composite representation of solar wind electrons as the *Core-Strahlo Model.* Within this framework, f_s corresponds to a Kappa function to which an asymmetry term δ has been added, as detailed in Equation (3.3).

$$f_e(v_\perp, v_\parallel) = f_c(v_\perp, v_\parallel) + f_s(v_\perp, v_\parallel), \tag{3.1}$$

[†] This chapter is based on information included in the articles: *Skew-Kappa Distribution Functions and Whistler Heat Flux Instability in the Solar Wind: The Core-Strahlo Model*, **Bea Zenteno-Quinteros**, Adolfo F. Viñas, & Pablo S. Moya, The Astrophysical Journal, 923(2):180 (2021) [140] and *The Role of Core and Strahlo Electron Properties on the Whistler Heat-Flux Instability Thresholds in the Solar Wind*, **Bea Zenteno-Quinteros** & Pablo S. Moya, Frontiers in Physics, 10:910193 (2022) [141].

with:

$$f_c(v_\perp, v_\parallel) = \frac{n_c}{\pi^{3/2}\alpha_\perp^2 \alpha_\parallel} \ \exp\left(-\frac{v_\perp^2}{\alpha_\perp^2} - \frac{(v_\parallel - U_c)^2}{\alpha_\parallel^2}\right), \tag{3.2}$$

$$f_s(v_\perp, v_\parallel) = n_s C_s \left[1 + \frac{1}{\kappa - \frac{3}{2}}\left(\frac{v_\perp^2}{\theta_\perp^2} + \frac{v_\parallel^2}{\theta_\parallel^2} + \delta\left(\frac{v_\parallel}{\theta_\parallel} - \frac{v_\parallel^3}{3\theta_\parallel^3}\right)\right)\right]^{-(\kappa+1)} . \tag{3.3}$$

In the expressions above, the subscripts $\perp$ and $\parallel$ refer to directions relative to the background magnetic field. Additionally, in Equation (3.2), the parameters $\alpha_\perp$ and $\alpha_\parallel$ represent the core thermal velocities, n_c stands for the core number density, and U_c denotes the core drift velocity. In Equation (3.3), n_s is the strahlo number density, and C_s serves as the normalization constant, ensuring that $n_s = \int f_s d\mathbf{v}$. Moreover, $\theta_\perp$ and $\theta_\parallel$ are associated with the strahlo kinetic temperatures, $T_{\perp,\parallel,s}$, as defined in Equations (A.5) and (A.6), respectively. Lastly, κ quantifies the deviation of this function from a Maxwellian distribution, and δ controls the field-aligned skewness. It is worth noting that when $\delta = 0$, we recover the well-known Kappa distribution. [58, 101, 142–147].

3.1 Validity of the model

Depending on the values of the κ and δ parameters, Equation (3.3) may yield negative, complex, or multi-valued results, introducing certain caveats and limitations to the applicability of the skew-Kappa function for modeling the electron velocity distribution function (eVDF). Specifically, for arbitrary values of δ and κ, there exists a critical value $u = v_\parallel/\theta_\parallel$ at which the skew-Kappa function exhibits a divergence, following a vertical asymptote. For $v_\perp = 0$, this critical value corresponds to the real solution of the following equation:

$$\kappa - \frac{3}{2} + \frac{v_\parallel^2}{\theta_\parallel^2} + \delta\left(\frac{v_\parallel}{\theta_\parallel} - \frac{v_\parallel^3}{3\theta_\parallel^3}\right) = 0, \tag{3.4}$$

which always exists for real values of κ and δ. The dependency of u on the parameters δ and κ exhibits contrasting strengths. Notably, the relationship with δ is strong, while the influence of κ is comparatively weaker. For example, for $\delta = 0.1$, the real solutions of Eq. (3.4), in units of the strahlo's thermal speed, are approximately $u \simeq 30.1$ for $\kappa = 3$ and $u \simeq 30.4$ for $\kappa = 10$. Similarly, when $\delta = 0.2$, the values become approximately $u \simeq 15.3$ and $u \simeq 15.7$ for $\kappa = 3$ and $\kappa = 10$, respectively. Furthermore, due to the peak of the skew-Kappa function at $v_\parallel \simeq 0$ and the presence of the aforementioned asymptote, the distribution always exhibits a local minimum at u_{min}, where $0 < u_{min} < u$. This minimum is determined by the solution to the derivative of Eq. (3.4), namely

$$u_{min} = \frac{v_{\parallel min}}{\theta_\parallel} = \frac{1 + \sqrt{1+\delta^2}}{\delta}\,, \tag{3.5}$$

a monotonically decreasing function of δ, with $u_{min} \simeq 20.0$ for $\delta = 0.1$, and $u_{min} \simeq 10.1$ for $\delta = 0.2$. Consequently, for any given value of δ, there exists a speed regime in which the integrals necessary for constructing the moments of the distribution or the dispersion relation will exhibit vertical asymptotes, branch cuts, and poles. Thus, the analytical continuation of this function in the complex plane under such conditions can become a complex and challenging task. While we believe it may be feasible to obtain a bounded reasonable solution, conducting such calculations for any arbitrary parameter falls beyond the scope of this work. Therefore, the skew-Kappa model requires careful treatment when selecting values for δ.

To address these challenges, we employ the heuristic Core-Strahlo (CS) model in cases where the electron distribution exhibits small skewness, and the asymptote remains well-separated from the central core, measured in terms of thermal speed units. This allows us to expand all relevant integrals in a finite Taylor series around $\delta = 0$. It is important to note that this Taylor series is not applicable near $v_\parallel = u\theta_\parallel$ due to the vertical asymptote at u in f_s. For it to be allowable, the first derivatives of f_s with respect to velocity must exist, which is not the case for velocity values that satisfy Eq. (3.4). However, this mathematical problem can be overlooked if all relevant features of the distribution are concentrated at velocities within the $|v_\parallel|/\theta_\parallel < |u_{min}|$ range, i.e when the asymptote of the function is far away from the main core. In such cases, even though the Taylor series approximation will not precisely replicate the exact function for all velocity values, conducting calculations based on the approximate version across the entire velocity domain will allow analytical calculations while keeping all relevant physical characteristics of the skew-Kappa distribution. This approach will subsequently lead to a direct interpretation of the results and the relevance of each parameter. On the other hand, addressing the general case with arbitrary skewness, where the asymptote may be closer to the main core of the distribution, remains to be solved. In such scenarios, the Taylor expansion approach may not be a suitable representation of the skew-Kappa function near the singularity, and alternative functional expressions with more favorable properties in the complex plane might offer a better solution. In this context, one potential method to approximate the initial distribution for arbitrary skewness is by expanding Eq. (3.3) using a different basis. After preliminary analysis, it appears that the Padé approximant [148] could be a reasonable approach for such an endeavor, as this approximation does not introduce new singularities. However, it is important to note that such cases with arbitrary skewness, may not have a clear physical interpretation.

Moving forward, we will focus on situations with small values of δ, where $\delta^3 \ll 1$, and employ a Taylor expansion of Eq. (3.3) up to the second order in δ, as described in Eq.(A.1) in Appendix A.

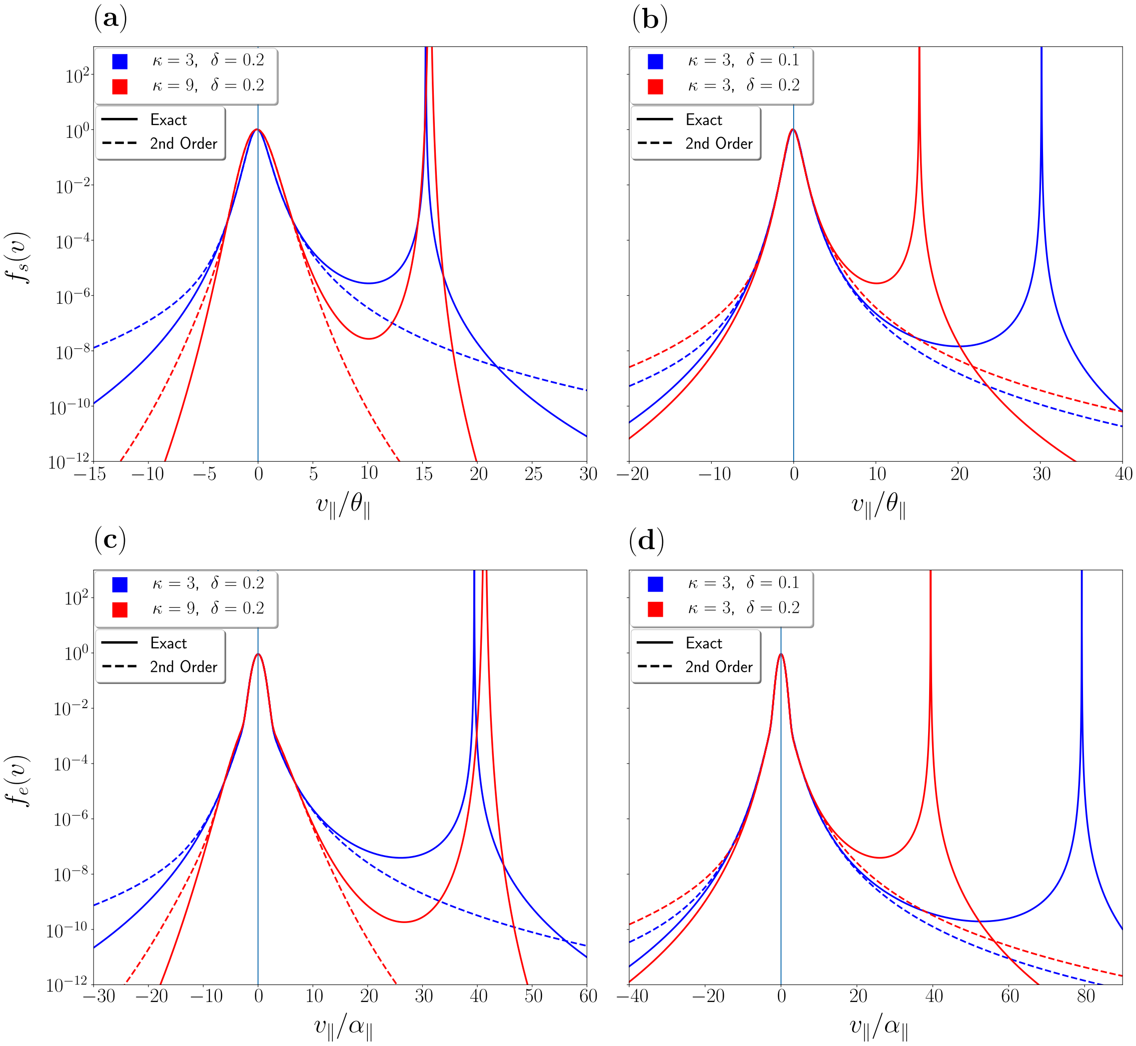

Figure 3.1: Parallel cuts at $v_\perp = 0$ of the electron distribution, considering isotropic subpopulations with $n_s/n_e = 0.1$ and $T_{\parallel s}/T_{\parallel c} = 7.0$, and various choices of κ and δ. The top and bottom panels show the skew-Kappa strahlo and the total electron distribution, respectively. In each panel, solid lines represent the exact function, while dashed lines correspond to the second-order Taylor expansion in δ. Moreover, vertical dotted lines indicate the local minima of the function, v_{min}, as defined in Eq. (3.5), and velocities are expressed in units of the thermal speed of the strahlo (top) or the core (bottom).

Figure 3.1 shows parallel cuts at $v_\perp = 0$ of the electron distribution for various choices of κ and δ with $n_s/n_e = 0.1$, $T_{\parallel s}/T_{\parallel c} = 7.0$ and considering isotropic subpopulations ($T_{\perp s}/T_{\parallel s} = T_{\perp c}/T_{\parallel c} = 1.0$), where $T_{\perp j}$ and $T_{\parallel j}$ represent the perpendicular and parallel kinetic temperatures of population j with respect to the background magnetic field. The top and bottom panels show, respectively, the skew-Kappa strahlo described by Eq. (3.3) and the total electron distribution, given by Eq. (3.1). These figures compare the exact distribution with a second-order Taylor expansion up to δ_s^2, as outlined in Eq. (A.1). Additionally, vertical dotted lines indicate the value of v_{min}, as defined in Eq. 3.5. From the figure, we observe that within the $|v_\parallel| < |v_{min}|$ velocity range, the exact and approximated versions of the distributions closely match. Notably, all significant features of the eVDF, including skewness and suprathermal tails, are clearly evident in both representations within this velocity range (as we will elaborate in Section 3.2). Consequently, for the regime of small skewness ($\delta_s^3 \ll 1$), a second-order approximation of electrons following a skew-Kappa distribution, as described in Eq.(3.3), can be reasonably represented by the Taylor expansion detailed in Eq.(A.1). In this scenario, all dispersion functions can be simplified into a superposition of standard integrals of the Kappa distribution in $v_\parallel$, similar to the Q integral presented in Eq. (5) of Mace and Hellberg [149] or Eq. (12) of Hellberg and Mace [150]. This regime has already been extensively investigated for both integer [151] and arbitrary [149, 150] values of the κ parameter.

Lastly, it is important to note that Kappa functions exhibit power-law behavior for high-velocity values, which can lead to divergent moments of the distribution, depending on the κ parameter. This places constraints on permissible values of κ. In the case of a Kappa distribution, according to the standard definition, pressure is well-defined only for $\kappa > 3/2$. However, within our specific context, to ensure real and finite values for temperature and heat flux moments, κ must be further restricted to $\kappa > 5/2$ (additional details are provided in Appendix A). In summary, within the scope of this study, where $\delta^3 \ll 1$, the eVDF remains real and positive up to the second order in δ for all real values of $v_\parallel$. Additionally, the integrals in velocity space share the same poles and branch cuts as Kappa distributions [149, 150]. Consequently, all moments of the eVDF, as well as the dielectric tensor of the plasma, are well-defined within these constraints.

3.2 Properties of the model in the small skewness approximation

Even though the CS model has several free parameters, quasineutrality and zero-current conditions in the ions frame establish specific relationships among them. To illustrate, if the ion density is denoted as n_p, quasineutrality dictates that $n_e = n_c + n_s = n_p$. This relationship can be expressed as:

$$\frac{n_c}{n_e} + \frac{n_s}{n_e} = 1. \tag{3.6}$$

Also, due to the particular shape of the skew-Kappa distribution, when $\delta \neq 0$, f_s inherently possesses a field-aligned drift, specifically $U_s = -\delta\theta_\parallel/4$. Consequently, the zero-current condition determines that the value of U_c must satisfy:

$$U_c = \frac{n_s}{n_c}\frac{\delta}{4}\theta_\parallel. \tag{3.7}$$

Therefore, under this description, there will be a relative drift $\Delta U_\parallel$ between core and strahlo populations in the ions frame, which can be expressed as:

$$\Delta U_{\parallel} = \frac{\delta}{4}\,\theta_{\parallel}\,\frac{n_e}{n_c}\,. \tag{3.8}$$

Note that this relative drift arises solely due to the skewness of the strahlo component. In instances where the electron distribution has no skewness ($\delta = 0$), f_e reduces to a symmetrical distribution with a quasi-thermal core and a nonthermal halo represented by a Kappa distribution (see Pierrard et al. [52]). It is important to emphasize that these parameter restrictions, as given by Eqs. (3.6) and (3.7), are applicable to scenarios with small skewness values. Moreover, within the small skewness approximation, the normalization constant takes the form shown in Eq. (3.9).

$$C_s = \frac{\Gamma(\kappa+1)}{\left[(\kappa-\frac{3}{2})\pi\right]^{3/2}\theta_{\perp}^2\theta_{\parallel}\Gamma(\kappa-\frac{1}{2})}\left[1-\frac{\delta^2}{4}\Psi_1(\kappa)\right]\,, \tag{3.9}$$

where:

$$\Psi_1(\kappa) = \left(\frac{2\kappa-1}{2\kappa-3}\right) - \frac{7}{12}\,.$$

For more details, full expressions of the macroscopic parameters of the strahlo distribution function can be found in Appendix A. Additionally, as we will demonstrate in Figures 3.2 and 3.3, the small skewness approximation effectively describes both quasithermal and suprathermal electrons in the solar wind. The parallel cuts of the eVDF exhibit remarkably similar shapes to those previously observed using data from ISEE-1 (see Fig. 1b in Scudder and Olbert [49]) and Wind (see Fig. 6 in Nieves-Chinchilla and Viñas [47]).

Figure 3.2 presents 1D plots at $v_{\perp} = 0$ of the total eVDF given by Eq. (3.1) and its two components, f_c and f_s, as functions of the velocity parallel to the mean magnetic field, expressed in units of the parallel thermal speed of the core. In the figure, the

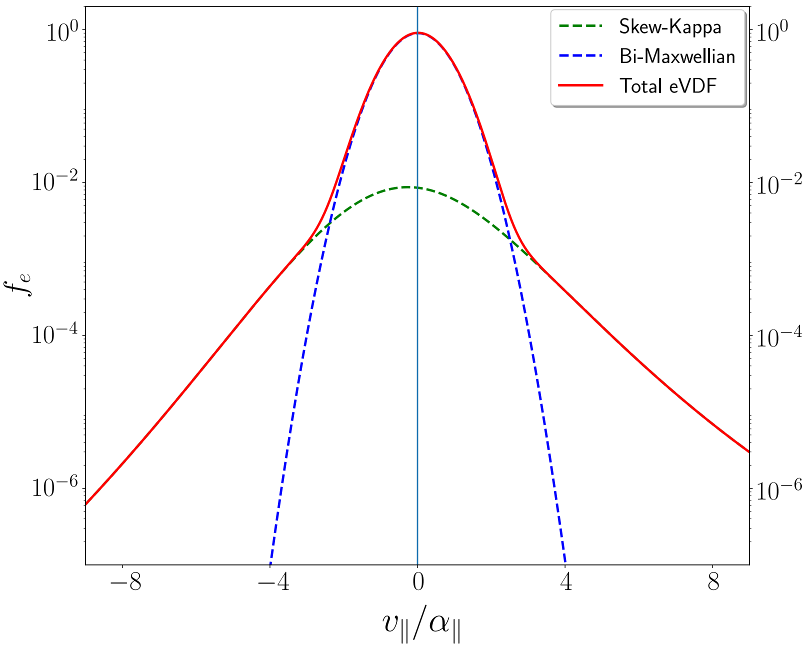

Figure 3.2: Parallel cuts at $v_{\perp} = 0$ of the electron distribution considering isotropic subpopulations with $n_s/n_e = 0.1$, $T_{\parallel s}/T_{\parallel c} = 7.0$, $\kappa = 5$, and $\delta = 0.2$. Blue, green, and red curves correspond to core, strahlo, and total eVDF, respectively. Velocity is expressed in units of the thermal speed of the core.

blue and green curves represent the core and strahlo subpopulations, respectively, while the red curve represents the total distribution. These curves were obtained with fixed parameters, including a 10% density for the suprathermal population (strahlo) ($n_s/n_e = 0.1$), and a temperature ratio of $T_{\parallel s}/T_{\parallel c} = 7.0$, which are typical values found in the solar wind [54, 58, 86]. We also considered $\delta = 0.2$ and $\kappa = 5$, along with isotropic subpopulations ($T_{\perp s}/T_{\parallel s} = T_{\perp c}/T_{\parallel c} = 1.0$). It is evident that the skew-Kappa distribution (3.3) exhibits asymmetry with respect to $v_{\parallel} = 0$, and this model presents characteristic features of solar wind electrons, such as enhanced tails and a narrower core for lower energies. Furthermore, a positive skewness parameter ($\delta > 0$) enhances the skew-Kappa and the total eVDF to the right, resulting in a positively skewed distribution along the field lines.

Furthermore, Figure 3.3 presents 1D plots at $v_{\perp} = 0$ (left) and contour plots (right)

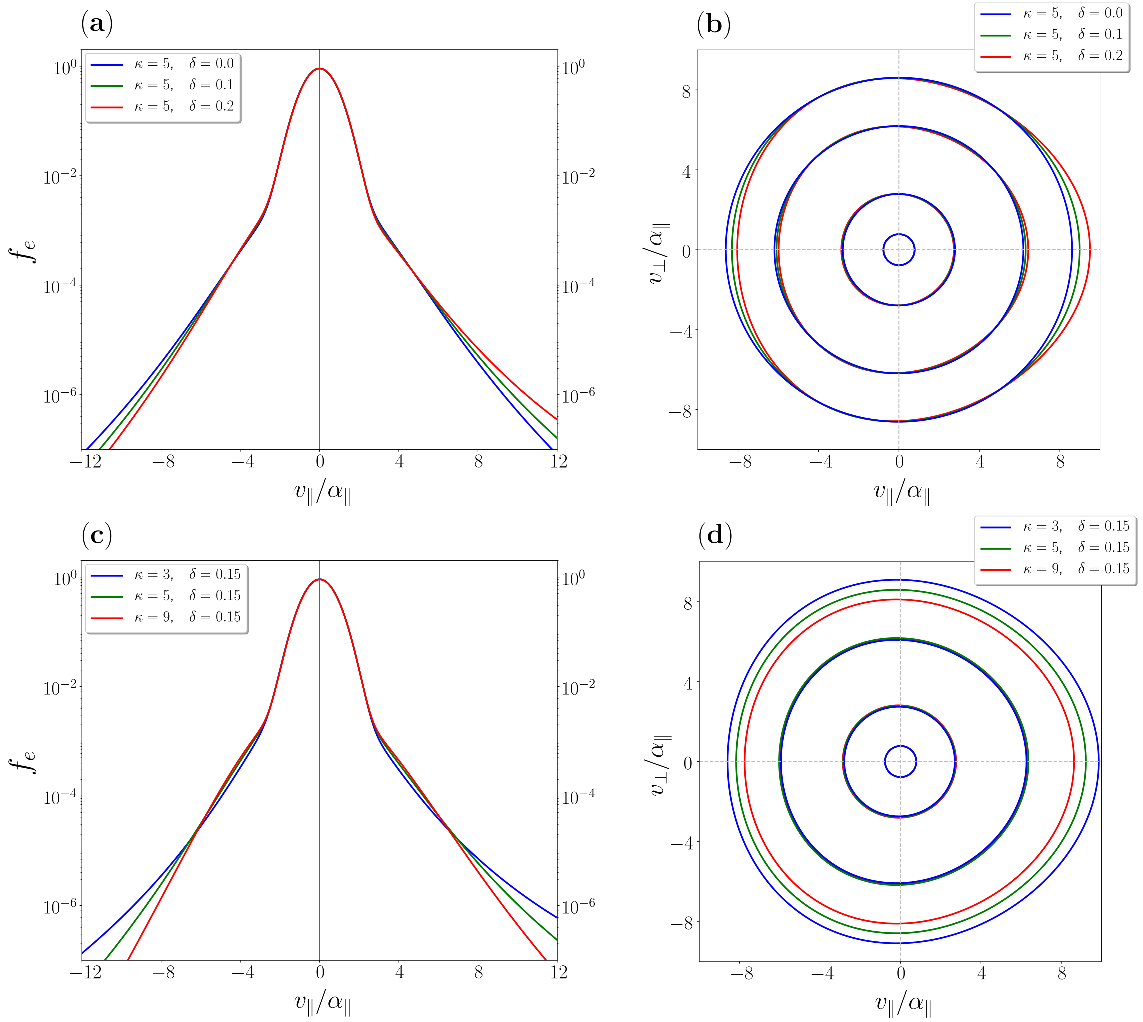

Figure 3.3: Parallel cuts (left) and contour plots (right) of the CS distribution from Eq. (3.1). Top panels consider fixed $\kappa = 5$, and different values of the skewness parameter: $\delta = 0$ (blue), $\delta = 0.1$ (green), and $\delta = 0.2$ (red); Bottom panels consider a fixed skewness ($\delta = 0.15$) and different kappa values: $\kappa = 3$ (blue), $\kappa = 5$ (green), and $\kappa = 9$ (red). All other parameters are the same as in Figure 3.2. In all panels, parallel and perpendicular velocity components are expressed in units of the thermal speed of the core $\alpha_\parallel$.

of the total electron distribution (3.1) for various values of δ and κ. For these plots, the rest of the relevant parameters remain the same as in Figure 3.2. In panels 3.3(a) and 3.3(b), we illustrate how the distribution changes for three distinct values of the δ parameter while keeping a fixed value of $\kappa = 5.0$. Both plots clearly depict that the strahlo distribution loses its symmetry compared to a Kappa function (represented by the $\delta = 0$ case), feature that is more evident in the outermost contours. Additionally, it is evident that higher values of δ result in a more skewed distribution. Panels 3.3(c) and 3.3(d), show how the distribution changes for three different κ values while maintaining a fixed $\delta = 0.15$. In panel 3.3(c), it is observed that increasing κ leads to a reduction in the high-energy tails, a characteristic inherited from Kappa distributions, which are reduced to Maxwellian functions in the limit $\kappa \to \infty$. However, unlike Kappa distributions, skew-Kappa functions never converge to Maxwellian distributions because they preserve skewness for all values of κ when $\delta \neq 0$. In panel 3.3(d), we notice that the outer contours appear to shrink proportionally as κ decreases, while the core remains unchanged. Consequently, the overall shape of the contours remains consistent, suggesting that κ does not impact the symmetry of the distribution.

Consequently, the CS distribution is able to replicate the primary field-aligned kinetic characteristics of the electron distribution observed in the solar wind: a quasi-thermal core, high-energy tails (whose slope is determined by κ), and magnetic field-aligned skewness (controlled by the parameter δ). Therefore, the skew-Kappa function effectively reproduces the distinct attributes of halo and strahl electrons in an integrated manner. It is the field-aligned skewness the supathermal feature providing the necessary energy for the excitation of the whistler heat flux instability (WHFI), which forms the central focus of our analysis in the subsequent chapters.

3.3 Influence of density and temperature on the model

Numerous studies have documented variations in the relative density of the suprathermal electron population (represented as the strahlo in this context), as well as fluctuations in the temperature ratio between different subpopulations throughout the Heliosphere [58, 86]. Consequently, it is of significant interest to investigate the impact of these parameters on the overall electron distribution and, by extension, their influence on the WHFI. In this section, we explore the modifications introduced by the strahlo-to-core parallel temperature ratio, $T_{\|s}/T_{\|c}$ and the relative density of the strahlo subpopulation, $\eta_s = n_s/n_e$ on the CS distribution, as defined by Eq. (3.1). Furthermore, these are the last two parameters that determine the shape of the total eVDF, that remain to be analyzed in the isotropic case ($T_{\perp s}/T_{\|s} = T_{\perp c}/T_{\|c} = 1.0$).

Figure 3.4 displays parallel cuts at $v_\perp = 0$ (left panels) and contour plots (right panels) of the CS distribution (3.1) under two sets of conditions: The top panels maintain a fixed $T_{\|s}/T_{\|c} = 7.0$ while varying the relative density of the strahlo subpopulation, $\eta_s = 0.04,\ 0.08,\ 0.12$. The bottom panels, on the other hand, fix $\eta_s = 0.08$ and vary the strahlo-to-core parallel temperature ratio, $T_{\|s}/T_{\|c} = 5.0,\ 7.0,\ 9.0$. In all cases, the plots were obtained considering isotropic core and strahlo distributions, with a skewness parameter $\delta = 0.2$ and a kappa parameter $\kappa = 3.0$. This figure illustrates key features of the CS distribution, including its field-aligned skewness, enhanced tails, and a narrower Maxwellian core, as previously discussed. In panels 3.4(a) and 3.4(b), we observe that changes in the relative density of the strahlo subpopulation have a notable impact on the high-energy tail of the distribution. As the skew-Kappa function describing the strahlo goes up with higher values of η_s, the

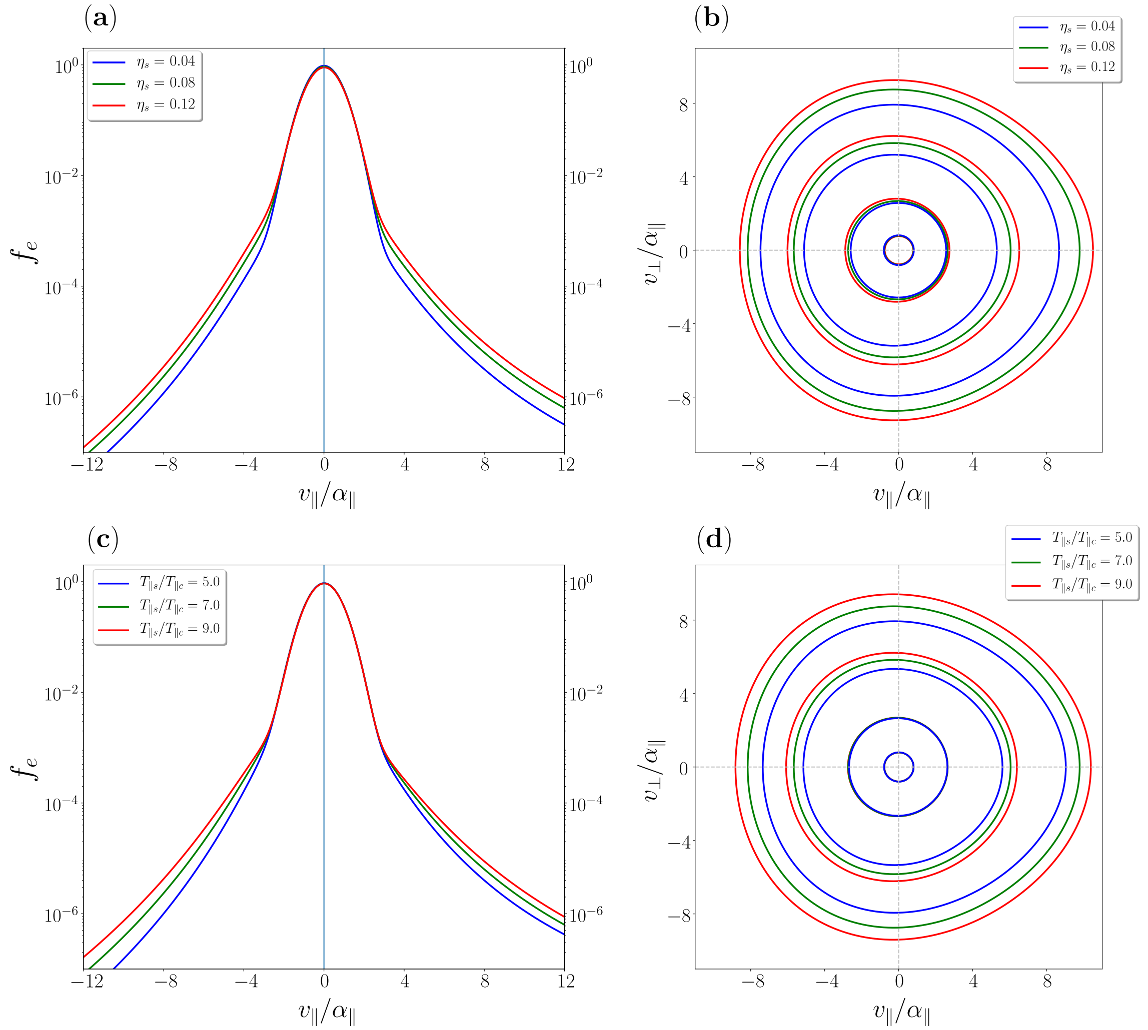

Figure 3.4: Parallel cuts (left) and contour plots (right) of the CS distribution from Eq. (3.1). Top panels consider fixed $T_{\parallel s}/T_{\parallel c} = 7.0$, and different densities $\eta_s = 0.04$ (blue), $\eta_s = 0.08$ (green), and $\eta_s = 0.12$ (red); Bottom panels consider fixed density ($\eta_s = 0.08$), and different temperature ratios $T_{\parallel s}/T_{\parallel c} = 5.0$ (blue), $T_{\parallel s}/T_{\parallel c} = 7.0$ (green), and $T_{\parallel s}/T_{\parallel c} = 7.0$ (red). In all panels, we considered a skewness parameter $\delta = 0.2$, a kappa parameter $\kappa = 3.0$, and set the anisotropy for the electron core and strahlo equal to one. Also, parallel and perpendicular velocity components are expressed in units of the thermal speed of the core $\alpha_\parallel$.

tails of the distribution become more pronounced. Conversely, variations in η_s have a relatively minor effect on the quasithermal core of the eVDF, resulting in only a slight decrease in core amplitude as η_s increases. Additionally, it is worth noting that from panel 3.4(a) it seems that the slope of these energetic tails remains consistent across varying values of η_s. The field-aligned skewness of the CS distribution also appears to remain unchanged, which becomes more evident in the contour plot shown in panel 3.4 (also, compare with Figure 3.3(b)).

We observe a similar trend when we modify the strahlo-to-core temperature ratio, $T_{\|s}/T_{\|c}$, as shown in panels 3.4(c) and 3.4(d). Clearly, this parameter also has an impact on the high-energy tails of the CS, distribution. Increased values of $T_{\|s}/T_{\|c}$ result in more pronounced energetic tails due to the widening of the skew-Kappa function describing the strahlo subpopulation as $T_{\|s}/T_{\|c}$ increases. In contrast, the Maxwellian core remains unaffected by changes in $T_{\|s}/T_{\|c}$, unlike the behavior observed with the previous parameter, η_s. Additionally, the skewness of the distribution appears to remain constant when $T_{\|s}/T_{\|c}$ is modified, as evident in the contour plot presented in panel 3.4(d). To summarize, both the strahlo-to-core temperature ratio and the density of the strahlo subpopulation can alter the tails of the distribution (3.1). The general trend is that as $T_{\|s}/T_{\|c}$ and η_s decrease, the high-energy tails diminish while preserving the skewness of the distribution. It is worth noting that in the analysis, we have used representative values for both parameters, which have been measured at various solar distances in the solar wind [54, 86].

3.4 A final comment on skew-Kappa functions

To the best of our knowledge, Beck [111] was the first to introduce skew distributions of the type (3.3) in a study of fully developed hydrodynamic turbulent flows, via non-extensive statistical mechanics. In this work, the author demonstrated that the asymmetry term, denoted as δ in our study, is inversely proportional to the square root of the Reynolds number (Re) of the medium ($\delta \propto Re^{-1/2}$). This distribution has found successful applications in fitting data from turbulent jet experiments in Beck [111] and environmental atmospheric turbulence studies in Rizzo et al. [152]. It is noteworthy that in both of these works, the velocity data adjusted by this model falls within the range of ± 10 thermal speeds (as illustrated in Figure 2 of Beck [111] and Figure 2 of Rizzo et al. [152]) and the obtained skewness parameters are small. Thus, the inherent mathematical challenges of the skew-Kappa distribution, discussed in Section 3.1, can be overlooked. Therefore, in both studies, the skew-Kappa model proves to be a useful tool for exploring the relevance and characteristics of skewed velocity distributions in turbulent flows.

As turbulence is also present in plasma systems, this suggests that these distributions can be more than an *ad-hoc* function for the solar wind electrons. The δ parameter can potentially be related to microscopic physical processes that allow the particles to exhibit a skew distribution. We strongly believe that rigorous theoretical works studying the underlying physics that allows particle distributions to present this suprathermal feature in plasma systems should be further explored. Recent studies by Gallo-Méndez and Moya [112, 153] have made significant strides in this direction. Notably, they have confirmed the validity of the relationship $\delta \propto Re^{-1/2}$ for plasma systems as well. Nonetheless, such first principle exploration falls beyond the scope of this work. Here, we focus on adopting and using heuristically the skew-Kappa function to describe the skewness and high-energy tails of the solar wind electron distribution, acknowledging the limitations mentioned earlier. This choice offers us an alternative to the conventional *core-halo-strahl* models, allowing us to describe the eVDF with fewer free parameters in both observational and theoretical works.

3.5 Discussion

In this chapter, we have introduced a novel approach for characterizing the electron population in the solar wind, named the *Core-Strahlo* model. In this description, the electron distribution is composed of two subpopulations: a quasithermal core described by a drifting bi-Maxwellian, and a suprathermal strahlo represented by a skew-Kappa function. We have demonstrated that the combination of Maxwellian and skew-Kappa distributions offers an effective framework for modeling three crucial features observed in solar wind electron distributions: the low-energy core, the enhanced energetic tails, and the magnetic field-aligned skewness.

It is important to emphasize that we thoroughly examined the behavior of the skew-Kappa function in velocity space, allowing us to establish a validity range for the CS model. Since this function always exhibits a singularity for any finite value of δ, the applicability of the CS model is limited to electron distributions with small skewness ($\delta^3 \ll 1$). In this context, the singularity is located sufficiently far from the main core of the distribution, measured in units of thermal speed. Under such conditions, all significant features of the CS distribution can be represented using a Taylor series approximation around $\delta = 0$, allowing us to circumvent the singularity. Therefore, we must impose the condition of small skewness, for this description to be applicable as a distribution function for solar wind electrons. Within this validity range, the skew-Kappa function can effectively reproduce the distinctive features of the halo and strahl subpopulations (energetic tails and skewness, respectively) in an integrated manner.

In the validity range, the parameter δ controls the field-aligned skewness of the distribution: higher δ values correspond to more skewed distributions, hence the term "skewness parameter". Additionally, the kappa parameter κ influences the slope of the high-energy tails, causing them to diminish as κ increases. Furthermore, the strahlo-to-core temperature ratio $T_{\|s}/T_{\|c}$ and the density of the strahlo subpopulation η_s also alter the tails of the CS distribution. The behavior is such that as these parameters increase, the high-energy tails get enhanced while maintaining the skewness of the distribution unaltered. With this, we conclude the study of all parameter space determining the shape of the total eVDF in the isotropic case.

Finally, using the CS description can simplify solar wind models by representing electrons as a superposition of core and strahlo populations, with the distribution skewness controlled by a single parameter. Additionally, considering a unified description of halo and strahl electrons may shed light on the significance of electron nonthermal features in solar wind heat transport dynamics [70]. This approach can also contribute to understanding the kinetic processes governing halo formation and its relationship with the strahl [109, 113, 131]. The field-aligned skewness, primarily governed by the skewness parameter δ in this representation, is the key suprathermal feature providing free energy for the excitation of WHFI. However, it is crucial not to overlook the influence of κ, η_s, and $T_{\|s}/T_{\|c}$ in shaping the eVDF. Given the wide range of values these parameters can take in the Heliosphere, the dependence of the CS distribution on them may also have implications for the excitation of the whistler mode. Our investigation in the following chapter will focus on WHFI and its dependence on all relevant parameter space for the isotropic case.

Chapter 4

Whistler heat flux instability & the Core-Strahlo model [†]

In the previous chapter, we showed that the Core-Strahlo (CS) provides us with a valuable tool for emulating crucial characteristics of observed electron distributions in the solar wind. In this chapter, our focus transitions towards utilizing the CS model as a heuristic approach to describe solar wind electrons in a theoretical exploration of the whistler heat flux instability (WHFI). Employing kinetic theory applied to non-collisional and magnetized plasmas, we investigate the influence of skewness and other non-Maxwellian features on the excitation of the parallel-propagating whistler mode associated with WHFI in a solar wind-like plasma.

[†] This chapter is based on information included in the articles: *Skew-Kappa Distribution Functions and Whistler Heat Flux Instability in the Solar Wind: The Core-Strahlo Model*, **Bea Zenteno-Quinteros**, Adolfo F. Viñas, & Pablo S. Moya, The Astrophysical Journal, 923(2):180 (2021) [140] and *The Role of Core and Strahlo Electron Properties on the Whistler Heat-Flux Instability Thresholds in the Solar Wind*, **Bea Zenteno-Quinteros** & Pablo S. Moya, Frontiers in Physics, 10:910193 (2022) [141].

4.1 Dispersion relation: parallel propagating wave modes

We initiate this process by deriving the dispersion relation for wave modes that can propagate in a magnetized, non-collisional, and initially uniform plasma using kinetic theory. The foundation for this kinetic treatment lies in the Vlasov equation:

$$\frac{\partial f_j}{\partial t} + \mathbf{v} \cdot \nabla_{\mathbf{r}}\, f_j + \frac{q_j}{m_j} \Big(\mathbf{E} + \frac{\mathbf{v}}{c} \times \mathbf{B} \Big) \cdot \nabla_{\mathbf{v}}\, f_j = 0 \tag{4.1}$$

and the Maxwell equations:

$$\begin{aligned} \nabla \cdot \mathbf{E} &= 4\pi\rho \ , \\ \nabla \times \mathbf{E} &= -\frac{1}{c}\frac{\partial \mathbf{B}}{\partial t} \ , \\ \nabla \cdot \mathbf{B} &= 0 \ , \\ \nabla \times \mathbf{B} &= \frac{4\pi}{c}\mathbf{J} + \frac{1}{c}\frac{\partial \mathbf{E}}{\partial t} \ . \end{aligned} \tag{4.2}$$

For a non-collisional plasma, the Vlasov equation (4.1) describes the time evolution in phase space of the distribution function f_j for species j. This evolution is driven by the self-consistent macroscopic electric and magnetic fields, denoted as **E** and **B**, respectively. These fields arise from the presence and motion of all charged particles within the plasma. In Equation (4.1), m_j and q_j represent the mass and charge of the particles composing species j, respectively, with c denoting the speed of light. On the other hand, the dynamics of the fields are dictated by the Maxwell equations, as shown in Equations (4.2). In these expressions, ρ and **J** correspond to the charge and current density inside the plasma, respectively. These quantities are linked to the distribution functions f_j:

$$
\begin{aligned}
\rho &= \sum_j q_j \int f_j d\mathbf{v} \ , \\
\mathbf{J} &= \sum_j q_j \int \mathbf{v} f_j d\mathbf{v} \, .
\end{aligned}
\tag{4.3}
$$

In the above expressions, the summation extends over all the different charged particle species present in the plasma. Consequently, Equations (4.1) and (4.2) form a complete and self-consistent set of equations.

The procedure for obtaining the dispersive properties of electromagnetic wave modes using plasma kinetic theory is a well-established technique [154, 155], involving the linearization of the Vlasov-Maxwell system of equations. To initiate this process, we start with a plasma system initially in equilibrium, a state characterized as neutral and current-free, where the macroscopic self-consistent electric and magnetic fields vanish throughout the plasma. In this equilibrium state, we assume that the distribution functions f_{0j} are independent of both time and space and that the plasma is immersed in a constant background magnetic field $\mathbf{B_0}$, produced by external sources. Next, we introduce small perturbations to the electromagnetic fields and the velocity distribution, deviating from the equilibrium state. As a result, we can express these quantities as follows:

$$
\begin{aligned}
&\mathbf{E} = \mathbf{E_1} \ , \\
&\mathbf{B} = \mathbf{B_0} + \mathbf{B_1} \ , \\
&f_j = f_{0j} + f_{1j} \, .
\end{aligned}
\tag{4.4}
$$

In the expressions above, the subscript 1 designates the first-order perturbed quantities, which are consistently assumed to be small in comparison to the equilibrium zero-order values represented by the subscript 0. By substituting these expressions into Equations (4.1) through (4.3) and neglecting the second-order terms, we derive the linearized Vlasov-Maxwell system. Next, we assume that the small-amplitude first-order perturbations of the relevant quantities take the form of plane waves, such as $A = A_k e^{i(\mathbf{k}\cdot\mathbf{r}-\omega t)}$. This formulation allows us to express the Vlasov-Maxwell system of equations as follows:

$$\mathcal{D}(\omega, \mathbf{k}, f_{0j}) \cdot \mathbf{E_k} = 0, \tag{4.5}$$

where $\mathbf{E_k}$ represents the complex amplitude of the electric field perturbation, and $\mathcal{D}(\omega, \mathbf{k}, f_j)$ denotes the dispersion tensor. This dispersion tensor is a 3×3 complex matrix depending on various factors, including the wave vector $\mathbf{k}$, the complex wave frequency $\omega = \omega_r + i\gamma$, and the background distribution functions f_{0j} of all plasma species j. The dispersion relation, $\omega = \omega(\mathbf{k})$, is determined by solving the condition $|\mathcal{D}(\omega, \mathbf{k}, f_{0j})| = 0$ so that Eq. (4.5) has non-trivial solutions for $\mathbf{E_k}$.

As an initial step in investigating the WHFI in the framework of the CS model, we focus on deriving the dispersion relation for wave modes propagating parallel to the background magnetic field, $\mathbf{B_0} = B_0\hat{z}$, resulting in the wave vector being expressed as $\mathbf{k} = k\hat{z}$. This restriction simplifies the mathematical analysis substantially compared to the oblique propagation case and aligns with previous research indicating larger growth rates for the field-aligned WHFI compared to the oblique case [63]. Additionally, we assume a plasma consisting solely of one ionic species, thus dealing with a proton-electron plasma. We employ the CS distribution (3.1) as the background distribution for the electrons ($j = e$), while the proton population ($j = p$) is described by an isotropic Maxwellian distribution, ensuring the fulfillment of both quasi-neutrality and zero-current conditions.

To facilitate the evaluation of the integrals required for the electron contribution to the dispersion tensor, we adopt the assumption that the electron skewness is small ($\delta^3 \ll 1$). This approximation is motivated by the mathematical constraints associated with the skew-Kappa distribution, as explained in Section 3.1. This assumption enables us to derive analytical expressions for the dispersion tensor elements, $D_i = D_i(\omega, k, pp)$, up to the second order in δ for parallel propagating modes while retaining all relevant physical properties of the function (3.3) in the calculations. The dispersion tensor elements depend on parameters such as the wavenumber k, the wave frequency ω, and the parameters describing the initial distribution functions, collectively denoted as pp. Moreover, since the electron distribution is a superposition of bi-Maxwellian and skew-Kappa functions, the elements D_i depend on the Fried and Conte plasma dispersion function $Z(\xi)$ [156] as well as the modified dispersion function $Z_\kappa(\xi)$ [90, 94, 150]. For detailed expressions of each element of the dispersion tensor, refer to Appendix B. Finally, throughout this study, we analyze the linear properties of the WHFI by solving the complex dispersion relation using our own developed dispersion solver.

4.2 Whistler heat flux instability

In this section, we present the results of our analysis of the excitation of the parallel-propagating whistler mode associated with the heat flux instability in an isotropic setting. To ensure consistency for comparison, we maintain specific parameters constant throughout our stability analysis. These parameters include fixing the proton distribution with $\beta_{\parallel p} = 0.1$ and $T_{\perp p}/T_{\parallel p} = 1.0$. Here, $\beta_{\parallel j}$ denotes the parallel plasma beta of population j, defined as $\beta_{\parallel j} = 8\pi n_j k_B T_{\parallel j}/B_0^2$. For the electrons, we maintain fixed temperatures for both components, the core and strahlo, with $T_{\perp s}/T_{\parallel s} = T_{\perp c}/T_{\parallel c} = 1.0$. This choice ensures that the subpopulations remain isotropic, eliminating any free energy associated with anisotropy in the electron velocity distribution (eVDF). Furthermore, our calculations assume a fixed ratio between the electron plasma frequency (ω_{pe}) and gyrofrequency (Ω_e) at $\omega_{pe}/|\Omega_e| = 200$, which aligns with typical solar wind conditions at 1 AU from the Sun. With this selection of parameters for protons and electrons, the only relevant suprathermal features in the study are the enhanced tails of the eVDF, represented by the κ parameter, and the electron skewness, represented by δ.

4.2.1 Influence of the skewness parameter on the WHFI

Considering the role of skewness as a source of free energy in exciting the WHFI, we initially focus on varying the δ parameter in our linear dispersion analysis to assess its impact on the stability of the whistler mode. For this initial exploration, we keep all other relevant parameters constant. These parameters include fixing the density of the strahlo suprathermal population at 10% ($n_s/n_e = 0.1$), maintaining the strahlo-to-core temperature ratio at $T_{\parallel s}/T_{\parallel c} = 7.0$, and setting $\beta_{\parallel s} = 1.0$ and $\kappa = 3.0$. These choices align with typical solar wind values [54, 58, 86]. In subsequent analyses, we will explore different values of these parameters to examine their influence on the dispersion relation.

Figure 4.1 illustrates the real (top) and imaginary (bottom) parts of the whistler mode frequency, for five different δ values while fixing $\kappa = 3.0$. Frequency and wavenumber are expressed in units of the electron gyrofrequency (Ω_e) and the elec-

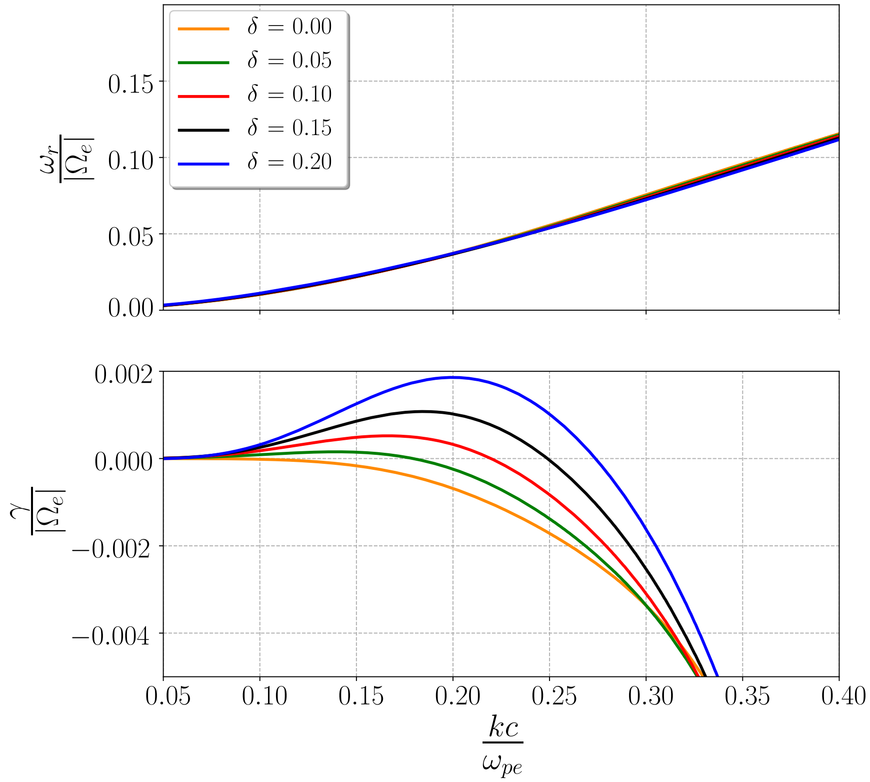

Figure 4.1: Real (top) and imaginary (bottom) parts of the dispersion relation $\omega = \omega(k)$ of the whistler mode for different δ values. We set the anisotropy for the electron core and strahlo populations equal to one, $n_s/n_e = 0.1$, $\beta_{\parallel s} = 1.0$, $T_{\parallel s}/T_{\parallel c} = 7.0$ and $\kappa = 3.0$.

tron inertial length $(c/|\omega_{pe}|)$. In the wavenumber range shown, we observe that the real part of the frequency remains relatively unchanged as δ increases. Conversely, the imaginary part exhibits a much stronger dependence on δ, and the wave mode becomes more unstable as δ increases. The range of wavenumbers over which the mode is unstable broadens, and both the maximum growth rate $\gamma_{\max}$ and the corresponding wavenumber rise with increasing δ. Note that this relationship is non-linear. For instance, at $\delta = 0.1$, the maximum growth rate reaches approximately $\gamma_{\max} \sim 5 \times 10^{-4}|\Omega_e|$, while at $\delta = 0.2$, it increases to around $\gamma_{\max} \sim 2 \times 10^{-3}|\Omega_e|$. This behavior aligns with our expectations since δ quantifies the free energy in the system associated with the distribution skewness. As δ increases, the distribution becomes more skewed, as illustrated in Figure 3.3(a) and 3.3(b). Therefore, it is anticipated that the wave mode becomes increasingly unstable with higher δ values, with the relationship between the maximum growth rate of the WHFI and the skewness parameter being non-linear.

4.2.2 Influence of power-law tails & and magnetization on the instability

Now, we turn our attention to the specific influence the strahlo parallel beta parameter ($\beta_{\|s}$) and the kappa parameter (κ) have on the linear stability of the parallel-propagating WHFI. Our goal is to comprehensively understand how variations in these parameters impact the excitation of the whistler mode. To achieve this, we examine the dispersion relation of this wave mode across a range of $\beta_{\|s}$ and κ values. Meanwhile, we keep the remaining key parameters at fixed values: the strahlo-to-core parallel temperature ratio is fixed at $T_{\|s}/T_{\|c} = 7.0$, and the strahlo density remains at $n_s/n_e = 0.1$. Importantly, we maintain a constant skewness parameter of $\delta = 0.15$ since, as demonstrated in Figure (4.1), this configuration corresponds to an unstable state for WHFI.

Figure 4.2 displays the normalized real and imaginary frequencies of the whistler mode (top and bottom, respectively) for various combinations of κ and $\beta_{\|s}$ values. In panel 4.2(a), we show the dispersion relation for different κ values while keeping a constant strahlo beta parameter at $\beta_{\|s} = 1.0$. It is clear that the real frequency remains nearly constant as κ changes, and the growth rates exhibit only weak dependence on this parameter, with a slight decreases as κ increases and $\kappa = 3.0$ the most unstable scenario. It is important to note that κ does not influence the sym-

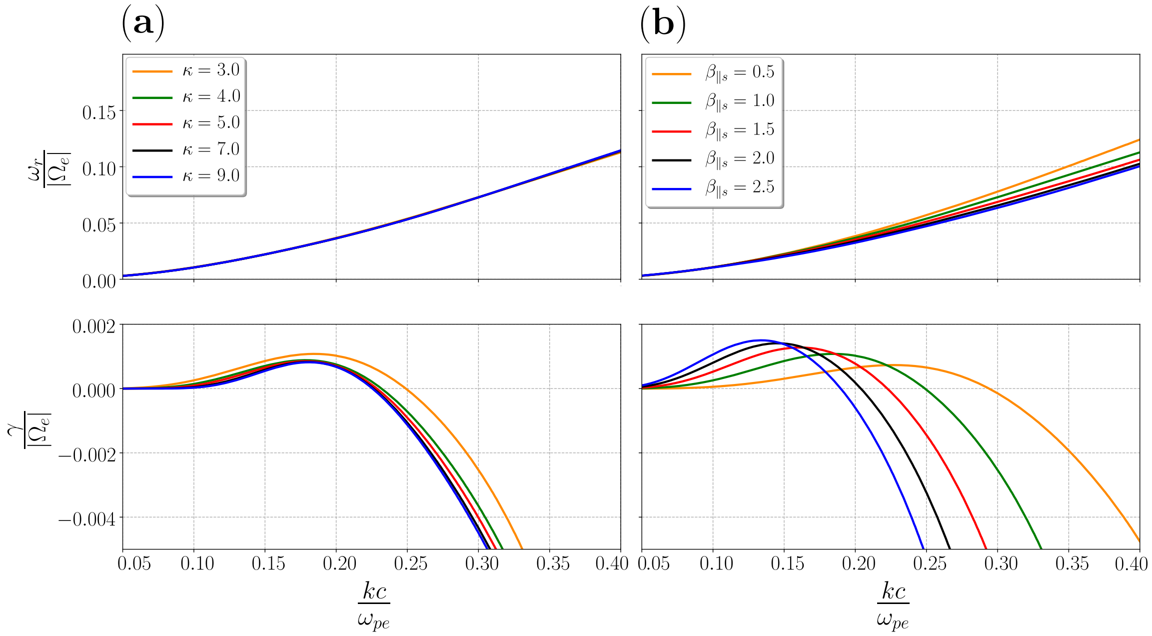

Figure 4.2: Real (top) and imaginary (bottom) parts of the dispersion relation $\omega = \omega(k)$ for the whistler mode for (a) $\beta_{\parallel s} = 1.0$ and different κ values; (b) $\kappa = 3.0$ and different $\beta_{\parallel s}$ values. In all cases, we set the anisotropy for the electron core and strahlo equal to one, $n_s/n_e = 0.1$, $T_{\parallel s}/T_{\parallel c} = 7.0$ and $\delta = 0.15$.

metry of the CS distribution, as demonstrated in panels (c) and (d) from Figure 3.3. Consequently, the observed minor dependence of the whistler mode stability on κ is an expected behavior.

On the other hand, with regard to the plasma beta parameter, panel 4.2(b) displays the dispersion relation of the whistler mode for various values of $\beta_{\parallel s}$ while keeping $\kappa = 3.0$ constant. In this case, within the displayed wavenumber range, we observe that the real part of the frequency exhibits more noticeable variations with this parameter compared to the previous two cases. Specifically, ω_r shows a slight decrease as $\beta_{\parallel s}$ increases. As expected, the growth rates exhibit a stronger dependence on the strahlo plasma beta. In all cases shown in the plot, there exists a range where the growth rate is positive, indicating the plasma is unstable to the whistler mode under these conditions. Notably, for higher $\beta_{\parallel s}$ values, the maximum growth rate also increases. However, with increasing $\beta_{\parallel s}$, the wavenumber at which the growth rate transitions from positive to negative values shifts to the left. In other words, the wavenumber range where the mode is unstable narrows with increasing $\beta_{\parallel s}$. Consequently, as a general guideline, for a given value of k, the growth rates increase with $\beta_{\parallel s}$, leading to faster wave amplitude growth. Simultaneously, as $\beta_{\parallel s}$ increases, the wave becomes stable for lower wavenumber values. This dependence of the maximum growth rates on beta aligns with expectations since higher β values imply a less magnetized plasma, making it more susceptible to destabilization due to electromagnetic fluctuations [90, 94].

4.2.3 Influence of density and temperature on the instability

Now, we shift our focus to investigating the impact of variations in the strahlo-to-core temperature ratio ($T_{\parallel s}/T_{\parallel c}$) and the relative density of the strahlo component ($\eta_s = n_s/n_e$) on the behavior of WHFI. Our aim is to gain a comprehensive understanding of how these parameter changes influence the excitation of the whistler mode. Thus, this analysis represents the final component in our examination of the instability as a function of all relevant parameters in the isotropic scenario. To examine the alterations in the dispersion relation, we explore a range of values for the strahlo-to-core parallel temperature ratio, spanning from $T_{\parallel s}/T_{\parallel c} = 3.0$ to $T_{\parallel s}/T_{\parallel c} = 11.0$, and investigate variations in the relative density extending up to 12% (i.e., $\eta_s = 0.12$). All these values have been measured in the solar wind as reported by Lazar et al. [86]. Furthermore, we maintain constant values for the remaining key parameters: the kappa parameter is held at $\kappa = 3.0$, and the strength of the background magnetic field is fixed to ensure $\beta_{\parallel s} = 1.0$. We also retain a consistent skewness parameter of $\delta = 0.2$, a configuration previously shown to yield positive growth rates for the whistler mode, as indicated in Figure 4.1.

Figure 4.3 presents the dispersion relation of the parallel-propagating whistler mode. The left panel maintains a constant value of $T_{\parallel s}/T_{\parallel c} = 7.0$ while varying η_s. In the right panel, we fix $\eta_s = 0.08$ and explore different values of $T_{\parallel s}/T_{\parallel c}$. Top and bottom panels display, respectively, the real frequency, ω_r, and the imaginary frequency, γ, expressed in units of the electron cyclotron frequency $|\Omega_e|$ and plotted against the normalized wavenumber kc/ω_{pe}. In panel 4.3(a), we observe a weak dependence of the real part of the frequency, ω_r, on the strahlo relative density η_s within the displayed wavenumber range. It results in a slight increase as η_s increases. For reference, we have included the cold plasma dispersion relation, which exhibits higher real frequencies, which is expected and consistent with previous studies (see for example Kuzichev et al. [72]). Shifting our focus to the imaginary part of the frequency, γ, we notice a significant trend. As the relative density of the strahlo component (η_s) increases, the waves become more unstable. Specifically, the wavenumber range over which $\gamma > 0$ expands, and the maximum growth rate ($\gamma_{\max}$) for this mode also increases with higher η_s. Considering the strahlo component is responsible for providing the free energy necessary for radiation, this behavior aligns with expectations, as a higher η_s value signifies a more significant suprathermal subpopulation relative to the core, as depicted in Figure 3.4(a). This trend is consistent with similar findings reported in previous studies, particularly in models featuring two drifting Maxwellian for the eVDF (see for example, Figure 3 in Gary [157]).

Panel 4.3(b) reveals that the real part of the frequency also exhibits a weak dependence on $T_{\parallel s}/T_{\parallel c}$, showing a decreasing trend as the strahlo-to-core temperature ratio diminishes. In contrast, the imaginary part of the frequency γ does not have such a straightforward behavior. For lower values of $T_{\parallel s}/T_{\parallel c}$, the wave mode be-

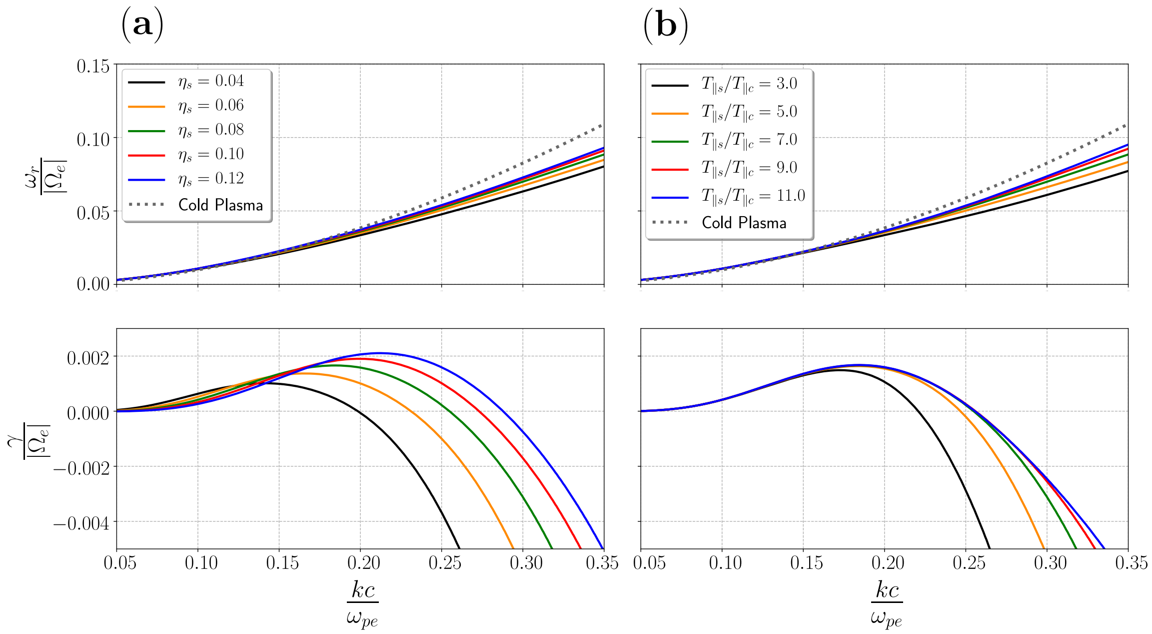

Figure 4.3: Real (top) and imaginary (bottom) parts of the dispersion relation $\omega = \omega(k)$ for the whistler mode for (a) $T_{\|s}/T_{\|c} = 7.0$ and different η_s values; (b) $\eta_s = 0.08$ and different $T_{\|s}/T_{\|c}$ values. In all cases, we set the anisotropy for the electron core and strahlo equal to one, $\beta_{\|s} = 1.0$, $\kappa = 3.0$ and $\delta = 0.2$.

comes increasingly unstable as this parameter increases. This effect is evident in the solutions corresponding to $T_{\|s}/T_{\|c} = 3.0$ and $T_{\|s}/T_{\|c} = 5.0$ (represented by the black and yellow curves, respectively). In these cases, the wavenumber range with positive growth rates widens, and $\gamma_{\max}$ exhibits a slight increase with higher $T_{\|s}/T_{\|c}$. However, starting from $T_{\|s}/T_{\|c} = 5.0$ onward, the changes in γ due to variations in the temperature ratio become negligible, and the curves remain nearly unchanged. This behavior persists even for higher $T_{\|s}/T_{\|c}$ values beyond those depicted in this plot. Consequently, a higher temperature, relative to the core, for the suprathermal subpopulation responsible for providing the free energy (the strahlo) does not lead to further destabilization of the plasma once it surpasses the saturation point at $T_{\|s}/T_{\|c} \approx 5.0$. This saturation phenomenon is also evident when considering other plasma parameters. For instance, when a skewness parameter of $\delta = 0.15$ and a strahlo relative density of $\eta_s = 0.1$ are employed, the growth rates also saturate at approximately $T_{\parallel s}/T_{\parallel c} \approx 5.0$. While a complete characterization of this saturation point is intriguing, especially in light of the absence of this feature in other models (see Figure 4 in [157], for instance), it requires a more extensive analysis that falls beyond the scope of this study.

4.3 The role of the heat flux moment on the instability

We are particularly interested in understanding the role of the WHFI in regulating the electron heat flux via non-collisional wave-particle interactions in the solar wind. In this context, we extend our stability analysis to investigate how the dispersion relation of whistler waves responds to variations in the field-aligned electron heat flux moment of the eVDF. In the small skewness approximation, the relationship between the parallel electron heat flux ($q_{\parallel e}$) and the parameters characterizing the CS electron distribution can be expressed as follows (up to second order in δ):

$$q_{\parallel e} = \frac{m_e \; n_s \; \theta_\parallel^3}{4} \; \delta \left[A_s \Psi_6(\kappa) + \Psi_7(\kappa) + \frac{1}{4} \left(\frac{\alpha_\parallel}{\theta_\parallel} \right)^2 (3 + 2A_c) \right] . \tag{4.6}$$

Here, the functions Ψ_6 and Ψ_7 depend solely on κ and are given by:

$$\Psi_6(\kappa) = \frac{1}{2} \left(\frac{2\kappa - 3}{2\kappa - 5} \right) - 1 \; , \tag{4.7}$$

and

$$\Psi_7(\kappa) = \frac{5}{4}\left(\frac{2\kappa - 3}{2\kappa - 5}\right) - \frac{3}{2} \ . \tag{4.8}$$

Additionally, A_c and A_s represent the intrinsic anisotropies for the core and strahlo populations, defined as $A_s = \left(\frac{\theta_\perp}{\theta_\parallel}\right)^2$ and $A_c = \left(\frac{\alpha_\perp}{\alpha_\parallel}\right)^2$, respectively (for detailed information, refer to Appendix A). To express the heat flux as a dimensionless quantity, it is customary to normalize $q_{\parallel e}$ to the free-streaming or saturation heat flux, denoted as $q_0 = (3/2) n_e k_B T_{\parallel c} \alpha_\parallel$ [for reference, see e.g 68]. Taking this normalization into account, the normalized heat flux, up to second order in δ, is expressed as follows:

$$\frac{q_{\parallel e}}{q_0} = \frac{\delta}{3}\frac{n_s}{n_e}\left(\frac{T_{\parallel s}}{T_{\parallel c}}\right)^{\frac{3}{2}} \left[\mu_s \Psi_6(\kappa) + \Psi_7(\kappa) + \frac{1}{4}\frac{T_{\parallel c}}{T_{\parallel s}}\left(3 + 2\mu_c\right)\right] \ . \tag{4.9}$$

In this expression, we have represented the normalized heat flux in terms of the kinetic temperatures $T_{\parallel j}$, as well as the associated temperature anisotropies, $\mu_j = T_{\perp j}/T_{\parallel j}$. From equation (4.9), it becomes evident that the normalized electron heat flux increases linearly with the skewness parameter δ. When all other parameters are held constant, an increase in δ results in a corresponding increase in $q_{\parallel e}/q_0$. Further, as illustrated in Figure 4.1, the increase in δ also reflects in the plasma becoming more unstable to the whistler mode. In this scenario, the linear relationship implies that a larger $q_{\parallel e}/q_0$ corresponds to a more skewed distribution, indicating a higher level of free energy available to excite the WHFI. Conversely, the functions $\Psi_6(\kappa)$ and $\Psi_7(\kappa)$ indicate that the electron heat flux decreases as κ increases. In this scenario, when we observe an increase in $q_{\parallel e}/q_0$, the plasma's stability to the whistler mode remains essentially unaltered, as observed in Figure 4.2(a). This means that when changes in heat flux values are attributable to variations in κ, such modifications result from adjustments in the high-energy tails, which are enhanced when κ decreases but do not alter the symmetry of the eVDF.

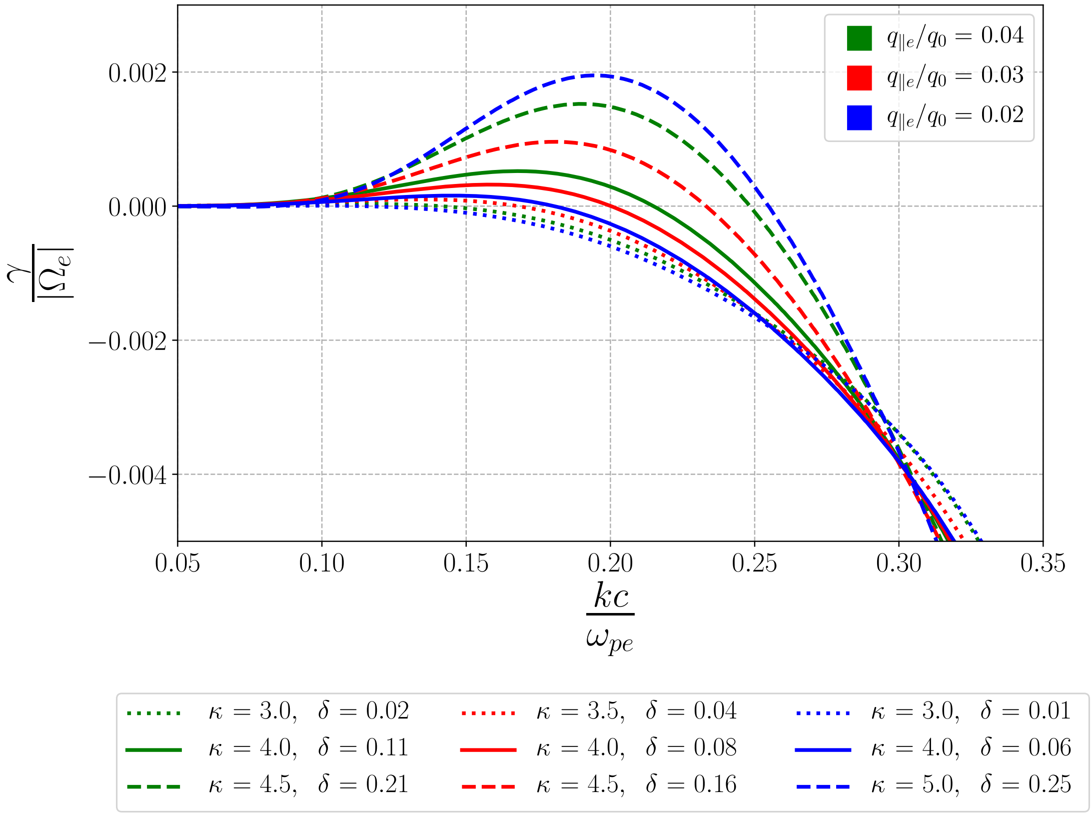

Figure 4.4: Growth rates of the whistler mode under specific plasma conditions: $\beta_{\parallel s} = 1.0$, $\mu_c = \mu_s = 1.0$, $T_{\parallel s}/T_{\parallel c} = 7$, and $n_s/n_e = 0.1$, with varying normalized heat flux values: $q_{\parallel e}/q_0 = 0.02$ (blue lines), $q_{\parallel e}/q_0 = 0.03$ (red lines), and $q_{\parallel e}/q_0 = 0.04$ (green lines). As the same heat flux can be achieved by multiple combinations of electron parameters, for each value of the heat flux the growth rates have been derived using 3 distinct sets of parameters (κ, δ), distinguished by line style (solid, dashed and dotted lines).

To gain deeper insights into the behavior of the heat flux parameter and its influence on the stability of the whistler mode, Figure 4.4 illustrates the normalized growth rates $\gamma/|\Omega_e|$ of this wave mode as a function of the normalized wave number for various initial normalized electron heat flux values $q_{\parallel e}/q_0$. We calculate this parameter using different combinations of κ and δ to examine the interplay between these two suprathermal features: skewness and energetic tails of the eVDF. All other relevant parameters are held constant, with values consistent with those used in Figure 4.1. Specifically, we consider isotropic electron populations ($\mu_c = \mu_s = 1.0$), a strahlo density of 10% ($n_s/n_e = 0.1$), $\beta_{\parallel s} = 1.0$, and $T_{\parallel s}/T_{\parallel c} = 7.0$. In Figure 4.4, the blue, green and red lines represent $q_{\parallel e}/q_0 = 0.02$, $q_{\parallel e}/q_0 = 0.03$, and $q_{\parallel e}/q_0 = 0.04$, respectively. Different line styles distinguish between the parameter combinations used. We can see that, for the same value of q_e/q_0, the stability of the whistler mode varies depending on the selected parameters. Combinations with higher δ values (indicated by dashed lines) consistently exhibit greater instability in this mode, with positive growth rates sustained over a wider wavenumber range and higher maximum growth rates. Additionally, it is worth noting that achieving the same heat flux value requires higher δ values when κ is increased.

From the analysis of Figure 4.4, a valuable conclusion can be drawn regarding the interplay between the heat flux parameter and plasma stability. When κ remains fixed, the heat flux parameter serves as a direct measurement of the skewness of the distribution function and, consequently, the plasma stability (as seen in the solid lines in Figure 4.4). In this scenario, a higher initial heat flux value unequivocally corresponds to increased whistler mode instability. Conversely, when δ is held constant, establishing a straightforward connection between the heat flux and plasma stability becomes more complex. Altering the heat flux value under these conditions may not necessarily impact the stability of the whistler mode, especially when considering that the growth rates only weakly depend on the κ parameter.

The situation becomes more intriguing when both parameters can vary in calculating the initial electron heat flux. In such cases, the same value of $q_{\parallel e}/q_0$ can be achieved using different combinations of κ and δ. Since only the latter parameter significantly influences the skewness of the distribution, different combinations result in varying stabilities for the whistler mode. In other words, systems with different levels of distribution asymmetry and, consequently, varying degrees of stability to the whistler mode, can share identical heat flux values. Therefore, the heat flux parameter can no longer be considered a direct measure of this suprathermal feature (the skewness of the eVDF), which provides the free energy necessary to radiate electromagnetic waves. As a result, it is inconclusive to claim that higher heat flux values exclusively indicate more unstable states. Further, when we take into account the other parameters involved in the calculation of the normalized heat flux macroscopic parameter, specifically $T_{\|s}/T_{\|c}$ and η_s, as outlined in Eq. (4.9), this assertion gains further support. This is because *in-situ* measurements show that these parameters exhibit several values as a function of heliocentric distance and solar wind speed [58, 86] and, as discussed in Section 4.2.3, they impact the stability of the parallel-propagating whistler mode in varying degrees. Thus, the heat flux alone may not be the best indicator of stability for this wave mode.

4.4 Comparison with Core-Strahl model

In this section, we perform a comparative analysis of dispersion properties between a core-strahl model based on drifting Maxwellian distributions and the skew-Kappa CS model. Our primary objectives are to provide theoretical support for the CS model used throughout this chapter to describe the electron distribution and to reaffirm the validity of the second-order expansion (A.1) of the distribution function (3.1), as well as the results obtained from the dispersion relation analysis regarding the WHFI in the preceding sections.

Accordingly, Figure 4.5(a) shows the dispersion relation of the parallel-propagating whistler mode considering a core-strahl model. We use a drifting isotropic Maxwellian distribution, as described in Eq. (4.10) with $\alpha_{\perp j} = \alpha_{\parallel j}$, to represent both the core subpopulation ($j = c$) and the strahl (beam) component ($j = b$), ensuring the electrons follow a current-free model, as outlined in Gary et al. [68].

$$f_j(v_\perp, v_\parallel) = \frac{n_j}{\pi^{3/2}\alpha_{\perp j}^2 \alpha_{\parallel j}} \exp\left(-\frac{v_\perp^2}{\alpha_{\perp j}^2} - \frac{(v_{\parallel j} - U_j)^2}{\alpha_{\parallel j}^2}\right). \tag{4.10}$$

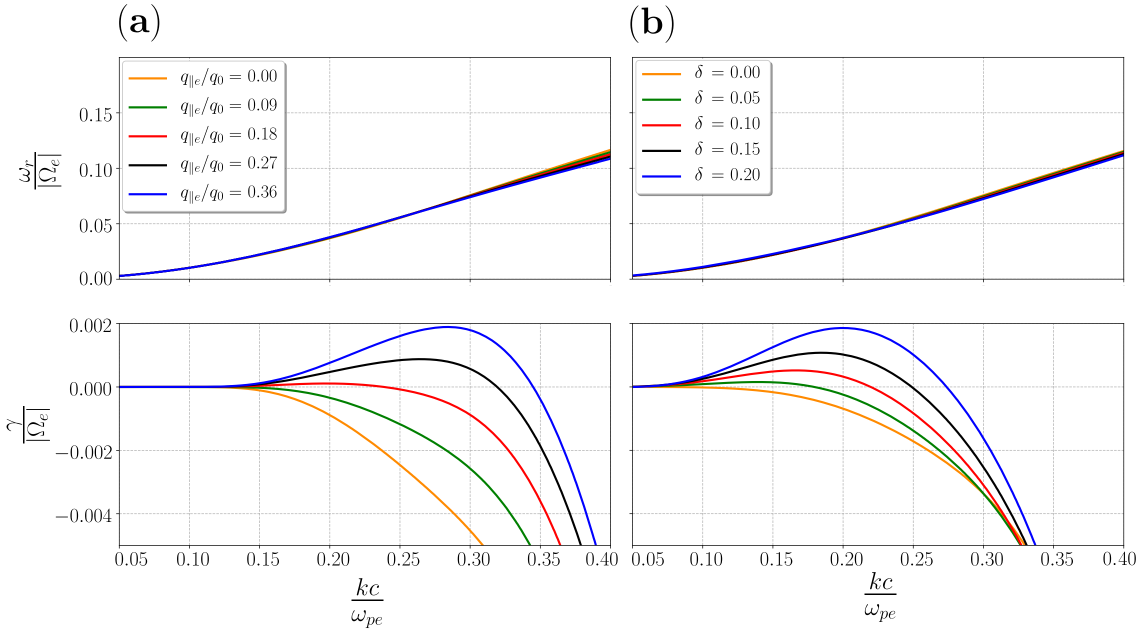

Figure 4.5: Dispersion relation for the whistler mode showing the real (top) and imaginary (bottom) parts for (a) core-strahl model consisting of two drifting Maxwellian distributions with varying heat flux moment values; (b) a CS distribution with $\kappa = 3.0$ and different δ values. In all cases, anisotropy for the electron core and strahlo (or core and beam) is set to one, $n_s/n_e = n_b/n_e = 0.1$, $\beta_{\parallel s} = \beta_b = 1.0$, and $T_{\parallel s}/T_{\parallel c} = T_b/T_c = 7.0$. Furthermore, identical line colors in both plots represent the same heat flux moment value.

The top and bottom panels display the normalized real frequency, $\omega_r/|\Omega_e|$, and the normalized imaginary frequency, $\gamma/|\Omega_e|$, respectively. These quantities are plotted as functions of the normalized wavenumber kc/ω_{pe} for five different values of the electron heat flux parameter. For the core-strahl representation, the normalized electron heat flux along the magnetic field $q_{\parallel e}/q_0$ can be approximated as follows:

$$q_{\parallel e}/q_0 \simeq (5/3)(n_c n_b/n_e^2)(\Delta U_{cb}/\alpha_c)(T_b/T_c - 1) \ , \tag{4.11}$$

where T_b and T_c represent the temperatures of the beam and core, respectively, n_b denotes the beam number density, and ΔU_{cb} denotes the relative drift between these subpopulations [68]. To facilitate a meaningful comparison, panel (b) of Figure 4.5 replicates the plot from Figure 4.1, where we used the CS distribution (3.1) to describe the electron population and derived the dispersion relation for different values of δ. It is important to note that, to ensure a fair comparison between both models, we maintained the same density, temperatures, and plasma beta for the core and beam as for the core and strahlo. Specifically, we set the beta parameter for the suprathermal component to $\beta_{\parallel h} = \beta_{\parallel s} = 1.0$, maintained a suprathermal-to-core temperature ratio of $T_b/T_c = T_{\parallel s}/T_{\parallel c} = 7.0$, and kept the relative density of the suprathermal population at 10%. Additionally, when solving for the dispersion relation of the whistler mode, we adjusted ΔU_{ch} such that, for each δ value shown in Figure 4.5(b), both models yielded the same heat flux moment.

Comparing Figures 4.5(a) and 4.5(b), it is evident that the dispersion relations obtained using the skew-Kappa CS and Maxwellian core-strahl models are qualitatively the same. Both models produce an identical real part of the dispersion relation and demonstrate similar stability levels regarding the WHFI. Nevertheless, subtle distinctions do exist. Notably, for an equivalent heat flux moment, the Maxwellian core-strahl model exhibits a shift towards larger wavenumbers compared to the CS model in terms of the maximum growth rate. These differences can be attributed to the models being based on different mathematical functions with distinct shapes and velocity gradients within the valid domain. It is important to emphasize that the dispersion relation inherently depends on these gradients. Additionally, this variance may also be attributed to the Taylor expansion to second order on the skewness parameter, present in the CS model but absent in the Maxwellian description of the plasma. Furthermore, it is worth noting that these subtle distinctions in the dispersion profiles between models have been previously discussed. Studies such as Abraham-Shrauner and Feldman [158] and Shrauner and Feldman [159], and possibly dating back to the early work on Bernstein modes [160], have explored these distinctions in the context of whistler and electromagnetic ion cyclotron waves in the solar wind. They have indicated that wave dispersion characteristics depend not only on physical moment parameters (density, temperature, drifts, heat flux, etc.) but also on the shape of the distribution function. In this case, the disparities arise from the absence of suprathermal tails in the Maxwellian model and the fact that, in the CS model, the source of asymmetry is strongly dominated by the skewness parameter, which is not present in the Maxwellian core-strahl approach. However, as illustrated in Figures 4.5(a) and 4.5(b), these differences are minor. Both models can adequately describe the WHFI in the small skewness regime. In conclusion, the results of the CS model closely align with previously reported behavior, reaffirming the validity of the model and its applicability to the heat flux instability problem (see Section 3.1).

4.5 Discussion

In this chapter, we used linear kinetic theory to conduct a stability analysis of the parallel-propagating whistler mode associated with the heat flux instability in a non-collisional, magnetized plasma. We employed the CS model to describe the solar wind eVDF, assuming a small electron skewness ($\delta^3 \ll 1$) and considering parameters typical of the solar wind. Utilizing the validity range of the model and the Vlasov-Maxwell system, we calculated the dispersion tensor for parallel-propagating waves and numerically solved the dispersion relation $\omega = \omega(k)$ for the whistler mode.

We investigated the sensitivity of various plasma parameters on the excitation of the parallel-propagating WHFI, specifically focusing on the skewness parameter δ, κ, $\beta_{\|s}$, the strahlo relative density η_s, and the strahlo-to-core temperature ratio $T_{\|s}/T_{\|c}$. Our findings demonstrated that for $\delta > 0$, the plasma is susceptible to the parallel-propagating WHFI. The growth rates of the mode increase with an increase in δ, which is the parameter that governs the skewness of the eVDF. Notably, these results from the CS model closely align with those obtained using more established models for the solar wind eVDF, providing support for its application in studying heat flux instability phenomena. Additionally, we observed that κ, controlling the extent of the high-energy power-law tails of the distribution, has a weak effect on the stability of this mode: as its value increases, the mode becomes slightly more stable. Regarding the other three parameters, as $\beta_{\|s}$, η_s, and $T_{\|s}/T_{\|c}$ increase, the plasma becomes more unstable to the WHFI. However, the dependence on $T_{\|s}/T_{\|c}$ is much weaker, and beyond a certain level ($T_{\|s}/T_{\|c} \sim 5$), changes in growth rates are no longer noticeable. Furthermore, while an increase in $\beta_{\|s}$ leads to a higher maximum growth rate for the whistler mode, it also narrows the unstable wave number range, in contrast to what occurs with the other two parameters.

With these results, we have examined how the stability of the whistler mode depends on all the parameters that shape the eVDF in the isotropic case. Utilizing the CS model has allowed us to thoroughly explore WHFI across the relevant parameter space in a manageable way, maintaining a realistic representation of the solar wind electron population, including quasi-thermal core, high-energy tails, and field-aligned skewness, all in a single comprehensive analysis. Furthermore, it is crucial to emphasize the significance of our findings in the context of solar wind plasma. The alterations induced by the parameters investigated in this section, however subtle they may seem, could notably impact the thresholds we use for comparisons with observational data. This consideration holds particular significance when evaluating the role of the WHFI in the non-collisional regulation of electron heat flux in the solar wind.

In addition, we presented the analytical expression for the normalized electron heat flux macroscopic parameter $q_{\|e}/q_0$ and analyzed its influence on the stability of the whistler mode. Traditionally, this parameter has served as a measure of the eVDF skewness, the suprathermal feature providing the energy that excites the WHFI. The key conclusion is that it is challenging to definitively predict how growth rates will be modified with an increase in the electron heat flux. This complexity arises because a specific $q_{\|e}/q_0$ value can be achieved through multiple combinations of key parameters. Consequently, the stability of the whistler mode greatly depends on how $q_{\|e}/q_0$ is calculated in terms of these parameters. Considering that, in this model, only δ controls the distribution skewness, and higher δ values (rather than higher $q_{\|e}/q_0$ values) are associated with more unstable states, our results imply that studies on WHFI excitation should primarily focus on distribution skewness, a purely kinetic property of the velocity distribution, rather than the heat flux moment, which represents a fluid quantity of the plasma.

Chapter 5

Marginal stability thresholds [†]

In the preceding chapter, we highlighted one of the primary objectives of this research: understanding the conditions under which the whistler heat flux instability (WHFI) develops in a plasma system. We explored this aspect using the Core-Strahlo (CS) model as a heuristic approach to describe solar wind electrons and investigated the influence of suprathermal electrons on the excitation of the parallel propagating WHFI. Specifically, we analyzed the dependency of the stability of the whistler mode on all relevant parameters for the isotropic case. However, our focus was limited to a few selected examples of dispersion relations, for specific plasma parameter values across the complete parameter space. In this chapter, our goal is to expand on the previous analysis and provide a framework for comparing theoretical predictions regarding WHFI excitation with observational data. Such a comparative

---

[†] This chapter is based on information included in the articles: *Skew-Kappa Distribution Functions and Whistler Heat Flux Instability in the Solar Wind: The Core-Strahlo Model*, **Bea Zenteno-Quinteros**, Adolfo F. Viñas, & Pablo S. Moya, The Astrophysical Journal, 923(2):180 (2021) [140] and *The Role of Core and Strahlo Electron Properties on the Whistler heat flux Instability Thresholds in the Solar Wind*, **Bea Zenteno-Quinteros** & Pablo S. Moya, Frontiers in Physics, 10:910193 (2022) [141].

analysis may offer valuable insights into how this instability contributes to regulating the final plasma state through wave-particle interaction and shed light on its role in the non-collisional regulation of electron heat flux in the solar wind. Accordingly, we now concentrate on systematizing our linear dispersion findings and computing the marginal stability thresholds for the parallel propagating whistler mode. These thresholds serve as a common benchmark for comparison with solar wind data. Our aim is to understand their dependence on all relevant plasma parameters, thus establishing a comprehensive framework for comparing theoretical results on the stability of this wave mode with electron measurements in the solar wind.

To determine the marginal stability thresholds for the parallel-propagating WHFI, we employ our custom-developed dispersion solver algorithm to calculate the normalized maximum growth rate, $\gamma_{\max}/|\Omega_e|$, of the whistler mode. Similar to our approach in the previous chapter, we consider a plasma comprising protons and electrons. We describe the electron population using the CS distribution given by Equation 3.1. On the other hand, the proton population is modeled using an isotropic Maxwellian distribution, ensuring quasi-neutrality and zero-current conditions. Concerning the plasma parameters, we maintain the same proton parameter values as detailed in Chapter 4, specifically setting $\beta_{\parallel p} = 0.1$ and $T_{\perp p}/T_{\parallel p} = 1.0$. For the electrons, we once again consider isotropic subpopulations, ensuring $\mu_s = T_{\perp s}/T_{\parallel s} = \mu_c = T_{\perp c}/T_{\parallel c} = 1.0$. This choice allows us to focus specifically on the electron skewness and energetic tails as the relevant suprathermal features in this study. Additionally, in our calculations, we set the ratio between the electron plasma frequency (ω_{pe}) and gyrofrequency (Ω_e) to $\omega_{pe}/|\Omega_e| = 200$.

The dispersion properties of wave modes in the isotropic case are controlled by several critical parameters, namely δ, κ, $\beta_{\parallel s}$, $\eta_s = n_s/n_e$, and $T_{\parallel s}/T_{\parallel c}$, as thoroughly discussed in the preceding chapter. However, instead of focusing on them directly, we initially concentrate on deriving $\gamma_{\max}/|\Omega_e|$ as a function of the normalized electron heat flux macroscopic parameter $q_{\parallel e}/q_0$, where q_0 represents the free-streaming heat flux. This parameter is the one that has traditionally been used to establish WHFI thresholds for comparison with observations. As $q_{\parallel e}$ is a moment of the distribution function, its expression depends on all the parameters that determine its shape in velocity space. For the validity range of the CS model, the relationship between $q_{\parallel e}/q_0$ and those crucial plasma parameters in the isotropic case is given by:

$$\frac{q_{\parallel e}}{q_0} = \frac{\delta}{3}\frac{n_s}{n_e}\left(\frac{T_{\parallel s}}{T_{\parallel c}}\right)^{\frac{3}{2}}\left[\frac{7}{4\kappa - 10} + \frac{5}{4}\frac{T_{\parallel c}}{T_{\parallel s}} - \frac{3}{4}\right] . \tag{5.1}$$

Equation (5.1) forms the basis for determining the marginal stability thresholds of the whistler wave in the $q_{\parallel e}/q_0$ vs $\beta_{\parallel s}$ space. Since δ is the primary driving parameter for the excitation of the WHFI, we calculate the thresholds while keeping the kappa parameter fixed at $\kappa = 3.0$ and the density of the strahlo population at 10% ($n_s/n_e = 0.1$). Additionally, we set $T_{\parallel s}/T_{\parallel c} = 7.0$. In this parameter configuration, $q_{\parallel e}/q_0$ directly measures the distribution skewness, as evident in Eq. (5.1). Accordingly, Figure 5.1 presents a contour plot displaying the normalized maximum growth rate $\gamma_{\max}/|\Omega_e|$ of the WHFI for a range of strahlo parallel beta and normalized heat flux parameters: $0.1 \leq \beta_{\parallel s} \leq 10$ and $1.8 \times 10^{-3} \leq q_{\parallel e}/q_0 \leq 0.45$, which corresponds roughly to $0.001 \leq \delta \leq 0.25$ based on Eq. (5.1). The plot shows a clear trend, where $\gamma_{\max}$ generally increases towards the right and upwards on the plot. In other words, as anticipated, the waves become more unstable in terms of the maximum growth rate achieved as both $\beta_{\parallel s}$ and $q_{\parallel e}/q_0$ increase. This behavior aligns with the patterns observed in figures 4.1 and 4.2(b). Moreover, this general shape of the threshold is consistent with the behavior observed in previous studies [133].

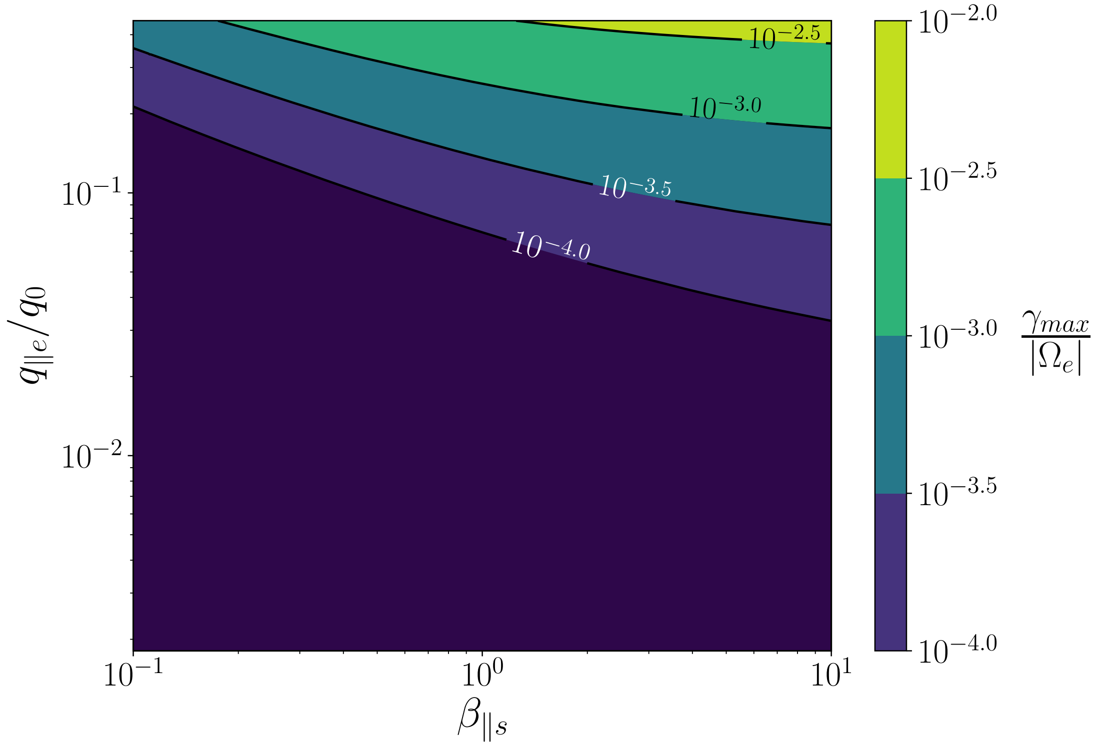

Figure 5.1: Maximum growth rate of the WHFI, normalized to the electron gyrofrequency ($\gamma_{\max}/|\Omega_e|$), for $\kappa = 3.0$, as a function of the parallel beta of the strahlo electrons ($\beta_{\|s}$) and the normalized parallel electron heat flux ($q_{\|e}$). The contours correspond to the thresholds $\gamma_{\max}/|\Omega_e| = 10^{-2.5}$, $10^{-3.0}$, $10^{-3.5}$, $10^{-4.0}$. These calculations were conducted with $\mu_c = \mu_s = 1.0$, $T_{\|s}/T_{\|c} = 7.0$, and $n_s/n_e = 0.1$.

To further investigate the influence of κ on the marginal stability thresholds, we conducted calculations for three specific κ values: $\kappa = 3.0$, 4.0, and 5.0. For each value, we computed the maximum growth rate within the same δ and $\beta_{\|s}$ ranges, utilizing the same proton and electron parameters as previously established. Additionally, since the core population constitutes the majority of solar wind electrons, we expressed the growth rates as a function of the core parallel beta parameter, $\beta_{\|c}$, to facilitate direct comparisons with observational data. Moreover, to model the stability thresholds for each κ value, we applied a fitting procedure using a generalized Lorentzian function, as outlined in Equation (5.2).

$$\frac{q_{\parallel e}}{q_0} = A_0 + \frac{B_0}{\left(\beta_{\parallel c} - \epsilon^2\right)^{\alpha}} \,. \tag{5.2}$$

This function was used to match the contour $\gamma_{\max}/|\Omega_e| = 10^{-3.0}$ and the resulting best-fit values for A_0, B_0, ϵ, and α, corresponding to each κ value, are presented in Table 5.1. The inclusion of these parameters is aimed at facilitating a straightforward comparison between these instability thresholds and solar wind observations.

Table 5.1: Best fit parameters for the $\gamma_{\max}/|\Omega_e| = 10^{-3}$ threshold of the whistler heat flux instability.

	A_0	B_0	A_1	B_1	ϵ	α
$\kappa = 3.0$	0.141	0.137	0.078	0.0760	8.7×10^{-6}	0.553
$\kappa = 4.0$	0.031	0.033	0.086	0.089	2.8×10^{-5}	0.630
$\kappa = 5.0$	0.007	0.008	0.085	0.095	1.7×10^{-5}	0.651

Note. The curve fitting for these thresholds was performed using the functions shown in Eqs. (5.2) (A_0, B_0) and (5.3) (A_1, B_1) for different κ values, and fixing $\mu_c = \mu_s = 1.0$, $T_{\parallel s}/T_{\parallel c} = 7.0$ and $n_s/n_e = 0.1$.

Figure 5.2 displays the fits representing the threshold behavior for different κ values. The blue, red, and green lines correspond to $\kappa = 3.0$, $\kappa = 4.0$, and $\kappa = 5.0$, respectively. The plot illustrates that, for a fixed $q_{\parallel e}$, the plasma becomes increasingly unstable as κ increases. This pattern aligns with the findings from Section 4.2. As κ increases, higher δ values are required to attain the same heat flux. In other words, as κ rises, more skewed distributions are necessary to achieve a given $q_{\parallel e}/q_0$. Consequently, a greater amount of free energy is available in the system to excite waves, resulting in higher growth rates, as observed in Figure 4.1. These observations further strengthen our earlier conclusion: it is not possible to establish a direct relationship between the heat flux moment and plasma stability concerning the WHFI. Thus, studies regarding the excitation of the WHFI should primarily focus on distribution skewness rather than the heat flux moment, since δ is the main driving parameter for the instability.

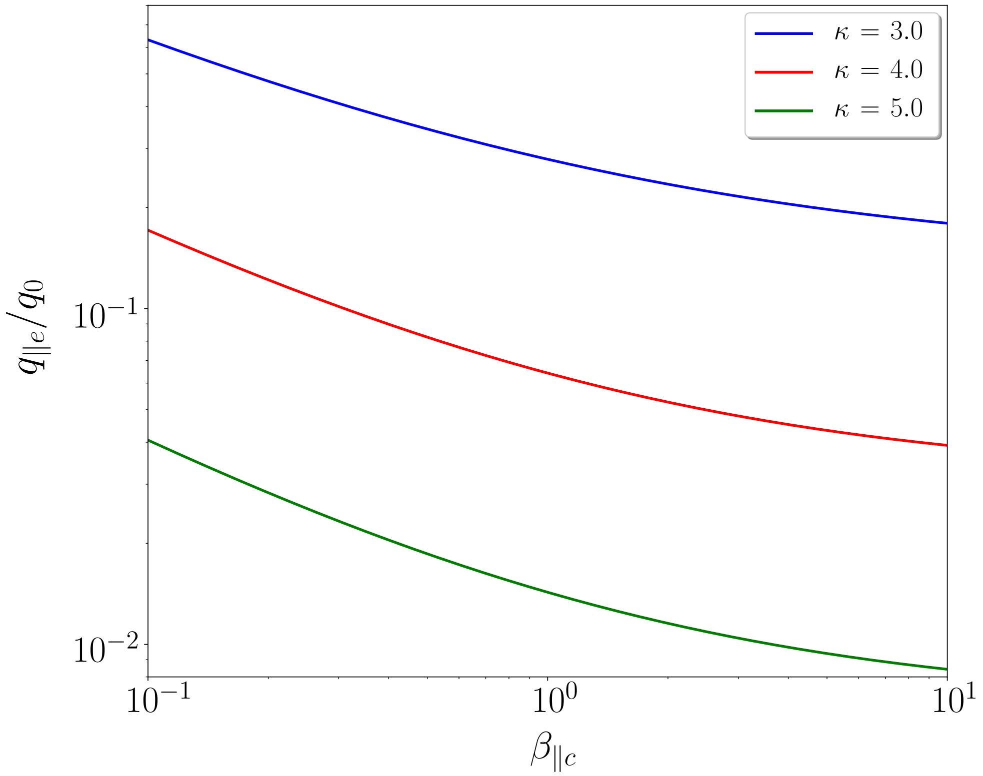

Figure 5.2: Fits for the instability thresholds of the whistler heat flux instability for $\kappa = 3.0$ (blue line), $\kappa = 4.0$ (red line) and $\kappa = 5.0$ (green line). The thresholds shown here correspond to maximum growth rates $\gamma_{\max}/|\Omega_e| = 10^{-3}$. All calculations were performed using $\mu_c = \mu_s = 1.0$ and $T_{\parallel s}/T_{\parallel c} = 7.0$, and $n_s/n_e = 0.1$.

Taking this suggestion into consideration, we also present the stability thresholds $\gamma_{\max}/|\Omega_e| = 10^{-3}$ in the $\delta - \beta_{\parallel c}$ space, for the same κ values previously mentioned ($\kappa = 3.0$, 4.0, and 5.0). These thresholds were fitted using a generalized Lorentzian function, as described in Equation (5.3):

$$\delta = A_1 + \frac{B_1}{\left(\beta_{\parallel c} - \epsilon^2\right)^{\alpha}}. \tag{5.3}$$

The best-fit values for parameters A_1 and B_1 are also presented in Table 5.1. Note that the best-fit values for ϵ and α remain the same as in the previous case using expression (5.2). Additionally, Figure 5.3 illustrates these fits, providing insight into the threshold behavior as κ varies. It is evident that the thresholds exhibit minimal changes as we vary κ, consistent with our earlier findings in the preceding section, confirming the weak dependence of the mode stability on this parameter.

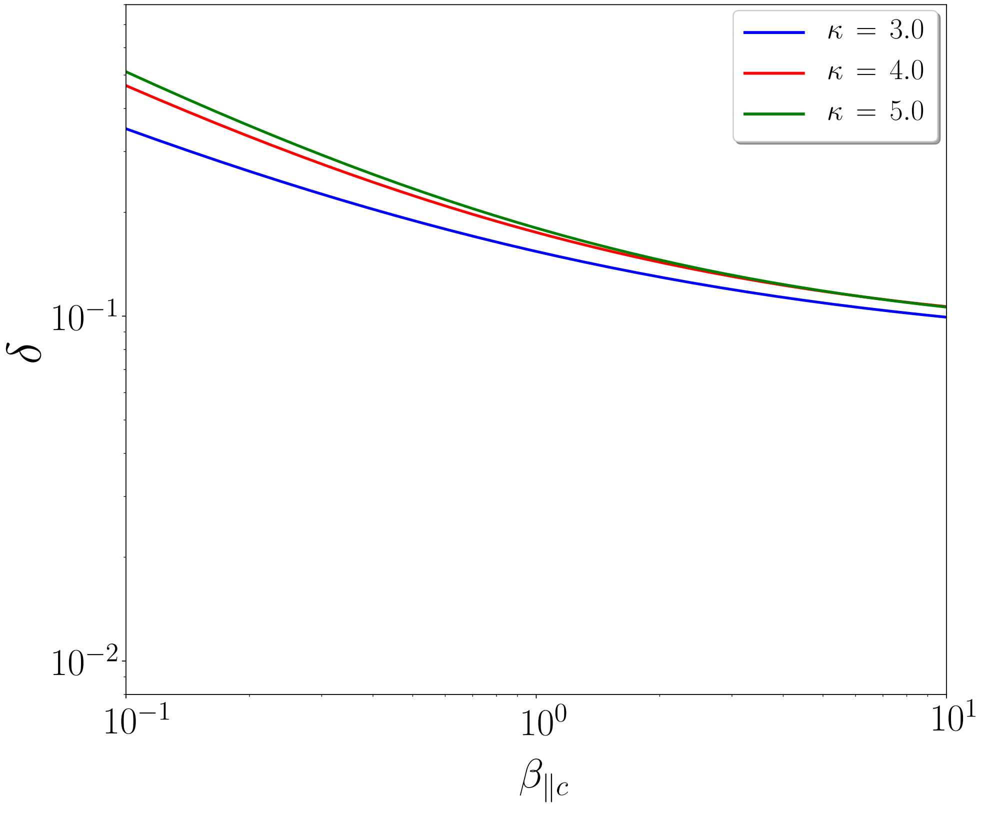

Figure 5.3: Fits for the instability thresholds of the whistler heat flux instability for $\kappa = 3.0$ (blue line), $\kappa = 4.0$ (red line), and $\kappa = 5.0$ (green line) as a function of δ. The thresholds shown here correspond to maximum growth rates $\gamma_{\max}/|\Omega_e| = 10^{-3}$. All calculations were performed using $\mu_c = \mu_s = 1.0$ and $T_{\parallel s}/T_{\parallel c} = 7.0$, and $n_s/n_e = 0.1$.

5.1 Influence of density and temperature on the thresholds

In this section, our focus shifts towards examining the influence of the last two key parameters: the strahlo-to-core temperature ratio ($T_{\|s}/T_{\|c}$) and the relative density of the strahlo component ($\eta_s = n_s/n_e$), on the behavior of marginal stability thresholds. To obtain these thresholds, we maintain the same plasma population descriptions as earlier: a Maxwellian distribution for protons with $\beta_{\|p} = 0.1$, and the CS distribution (3.1) with isotropic subpopulations for electrons. Furthermore, we fix the kappa parameter at $\kappa = 3.0$. With these parameters held constant, we calculate the normalized maximum growth rate $\gamma_{\max}/|\Omega_e|$ of the parallel-propagating whistler mode in the $\delta - \beta_{\|c}$ parameter space. This procedure is repeated for different values of η_s and $T_{\|s}/T_{\|c}$ within specified ranges ($0.04 < \eta_s < 0.12$ and $3.0 < T_{\|s}/T_{\|c} < 11.0$, based on solar wind electron measurements).

Consistent with the suggestion from the previous section, we have chosen to present the stability thresholds solely as a function of the skewness parameter δ, departing from the conventional representation using the electron heat flux macroscopic parameter $q_{\|e}$. As demonstrated in Eq. (5.1), for a fixed κ, the heat flux moment is dependent on all relevant parameters that determine the shape of the distribution, and can have the same value for different combinations of these parameters. To mitigate this ambiguity, we analyze the dispersion relation within the $\delta - \beta_{\|c}$ space. However, it is worth noting that using Eq. (5.1), it is not difficult to derive these thresholds in terms of $q_{\|e}/q_0$. Figure 5.4 shows the contour levels of $\gamma_{\max}/|\Omega_e| = 10^{-3}$ (red lines) and $\gamma_{\max}/|\Omega_e| = 10^{-4}$ (blue lines) for the normalized maximum growth rate under different values of η_s (left panel) and $T_{\|s}/T_{\|c}$ (right panel). In panel

5.4(a), we present these thresholds for a fixed value of $T_{\parallel s}/T_{\parallel c} = 7.0$, considering $\eta_s = 0.04,\ 0.08$, and 0.12 (indicated by solid, dashed, and dotted lines, respectively). Notably, as we increase the strahlo relative density, the thresholds shift downwards and to the left. As anticipated, the plasma becomes more susceptible to destabilization for higher η_s values. In other words, as we increase η_s, lower values of δ or $\beta_{\parallel c}$ are needed to produce the same growth rate of the WHFI. On the other hand, panel 5.4(b) shows the contours for $T_{\parallel s}/T_{\parallel c} = 3.0,\ 7.0$, and 11.0 (represented by solid, dashed, and dotted lines, respectively) while keeping $\eta_s = 0.08$ constant. Consistent with the trend observed in the previous plot, the plasma becomes more unstable to the parallel-propagating WHFI as $T_{\parallel s}/T_{\parallel c}$ increases, leading to a downward and leftward shift in the thresholds.

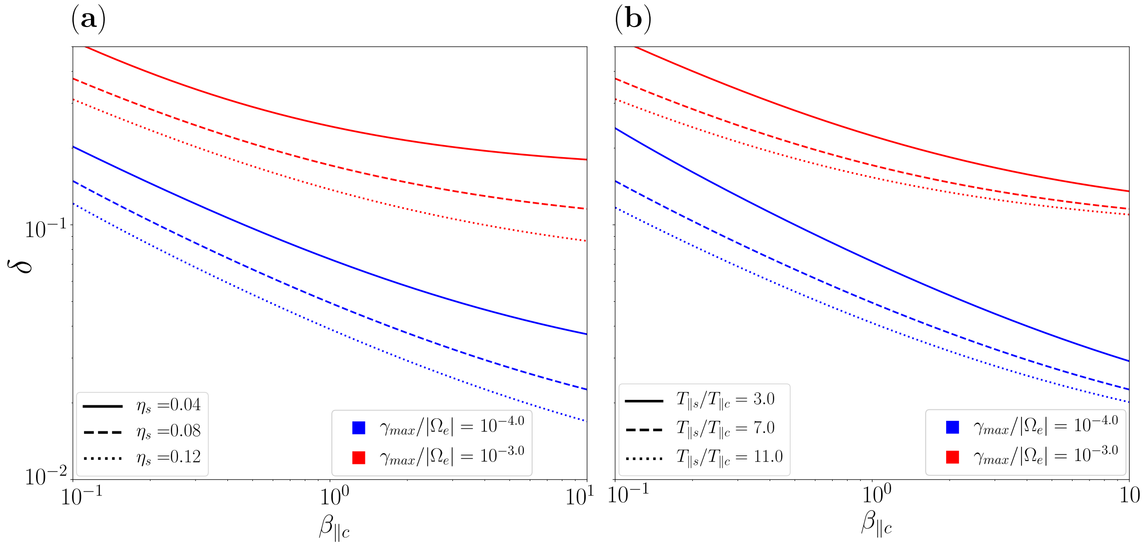

Figure 5.4: Instability thresholds $\gamma_{\max}/|\Omega_e| = 10^{-3}$ (red lines) and $\gamma_{\max}/|\Omega_e| = 10^{-4}$ (blue lines) of the whistler heat flux instability for (a) $T_{\parallel s}/T_{\parallel c} = 7.0$ and different η_s values; (b) $\eta_s = 0.08$ and different $T_{\parallel s}/T_{\parallel c}$ values. All calculations were performed using isotropic subpopulations and $\kappa = 3.0$.

Lastly, to enhance the comparability between observational data and the linear prediction for WHFI stability, we employ a fitting approach for the contour lines corresponding to $\gamma_{\max}/|\Omega_e| = 10^{-3}$ and 10^{-4}, utilizing the generalized Lorentzian function depicted in Eq. (5.3). The best-fit values for the parameters A_1, B_1, ϵ, and α pertaining to each threshold presented in Figure 5.4 are detailed in Table 5.2, facilitating a direct comparison with data in the beta range shown.

Table 5.2: Best fit parameters for the $\gamma_{\max}/|\Omega_e| = 10^{-3}$ and 10^{-4} thresholds of the whistler heat flux instability.

			A_1	B_1	ϵ	α
$\gamma_{\max} = 10^{-3}$	$\eta_s = 0.04$	$T_{\parallel s}/T_{\parallel c} = 7.0$	0.162	0.082	2.4×10^{-4}	0.648
	$\eta_s = 0.08$	$T_{\parallel s}/T_{\parallel c} = 3.0$	0.102	0.122	4.9×10^{-6}	0.559
		$T_{\parallel s}/T_{\parallel c} = 7.0$	0.094	0.077	4.8×10^{-6}	0.562
		$T_{\parallel s}/T_{\parallel c} = 11.0$	0.093	0.061	7.1×10^{-5}	0.557
	$\eta_s = 0.12$	$T_{\parallel s}/T_{\parallel c} = 7.0$	0.065	0.073	3.2×10^{-6}	0.530
$\gamma_{\max} = 10^{-4}$	$\eta_s = 0.04$	$T_{\parallel s}/T_{\parallel c} = 7.0$	0.023	0.050	1.5×10^{-5}	0.554
	$\eta_s = 0.08$	$T_{\parallel s}/T_{\parallel c} = 3.0$	0.013	0.059	0.117	0.553
		$T_{\parallel s}/T_{\parallel c} = 7.0$	0.012	0.037	0.094	0.541
		$T_{\parallel s}/T_{\parallel c} = 11.0$	0.012	0.029	0.076	0.540
	$\eta_s = 0.12$	$T_{\parallel s}/T_{\parallel c} = 7.0$	0.008	0.031	0.107	0.538

Note. The curve fitting for these thresholds was performed using the function shown in Eq. (5.3), fixing $\mu_c = \mu_s = 1.0$ and $\kappa = 3.0$.

5.2 Discussion

In this chapter, we employed linear kinetic theory to characterize the β-dependent linear stability thresholds of the parallel propagating WHFI in a non-collisional, magnetized plasma. We utilized the Core-Strahlo (CS) model to describe the solar wind electron distribution within its validity range ($\delta^3 \ll 1$) and considered typical solar wind parameters. We numerically solved the dispersion relation $\omega = \omega(k)$ for the whistler mode triggered by eVDF skewness and determined the maximum growth rate of the mode, initially as a function of the parallel electron heat flux and subsequently as a function of the skewness parameter δ. Additionally, we investigated how variations in κ, the strahlo relative density, and the strahlo-to-core temperature ratio influence the stability thresholds. Our analysis demonstrated the enhancing effect of η_s and $T_{\|s}/T_{\|c}$, as well as the weak dependence of these thresholds on κ in the $\delta - \beta$ space. Finally, for comparison with observational data, we presented the best-fit parameters, employing a generalized Lorentzian function for curve fitting and modeling these stability thresholds.

With the results presented in this chapter and the previous one regarding the influence of κ, η_s, and $T_{\|s}/T_{\|c}$ on the behavior of the whistler mode, we have demonstrated that each of these parameters distinctly and with varying strength alters the stability of the mode and, consequently, the thresholds we used for comparison with observations. It has been reported in several reports that these parameters characterizing the suprathermal population (the *strahlo* in the CS description) are not constant in the solar wind [54, 86, 105]. For instance, Lazar et al. [86] demonstrated that the average temperature ratio between the suprathermal halo and core subpopulations varies from $T_h/T_c \sim 8$ at 1 AU to $T_h/T_c \sim 3$ at 0.3 AU. Moreover, there are variations depending on solar wind conditions (slow and fast wind), resulting in substantial differences even at a specific radial distance. The temperature ratio ranges between approximately $T_h/T_c \sim 2$ and $T_h/T_c \sim 15$ at 1 AU, and the relative density of the halo varies from less than 1% to 15% (see Figure 2 and 3 in Lazar et al. [86]). Hence, we stress the importance of considering their real impact on the stability of the WHFI in solar wind scenarios. Furthermore, this reaffirms the conclusion that assessing the stability of a plasma state to the WHFI based solely on $q_{\|e}$ is inadequate. Additional information about the shape of the distribution and its dependence on all plasma parameters is crucial. Therefore, we believe that studying the role of WHFI in the relaxation process of plasma states should focus on the kinetic parameters that determine the eVDF, rather than exclusively relying on macroscopic moments.

It is essential to note that besides skewness, temperature anisotropy also plays a crucial role in wave emission. Nonetheless, various studies have shown that, among anisotropic states, the isotropic state is also prevalent in the solar wind at different solar distances and wind speeds (see for instance, Adrian et al. [85], Lazar et al. [86]). Up to this point in our work, we have focused on the effect of skewness in triggering the whistler mode. In the next chapter, we will provide a systematic study on the combined effect of both sources of free energy (skewness and anisotropy) and explore the subsequent interplay between the WHFI and the whistler-cyclotron instability.

Chapter 6

Interplay between skewness and strahlo anisotropy [†].

In the preceding chapters, our exploration was dedicated to investigating the conditions under which the whistler heat flux instability manifests in a plasma system, within the framework of the Core-Strahlo (CS) model. Employing Eq. (3.1) as a heuristic tool, we modeled the electron population in the solar wind and investigated the impact of suprathermal electrons on WHFI behavior. Specifically, our study meticulously examined the stability of the parallel propagating whistler mode and its dependency on the key parameters in the isotropic scenario: η_s, $\beta_{\|s}$, κ, δ, and $T_{\|s}/T_{\|c}$. However, empirical evidence from observations of the solar wind has consistently indicated that electron populations do not always exhibit isotropic temperatures [48, 53, 54, 85, 86]. Temperature anisotropies represent an additional source of free energy, capable of exciting electromagnetic radiation, and can be associated

---

[†] This chapter is based on information included in the article: *Interplay between Anisotropy- and Skewness-driven Whistler Instabilities in the Solar Wind under the Core–Strahlo Model.*, **Bea Zenteno-Quinteros**, Pablo S. Moya, Marian Lazar, Adolfo F. Viñas, & Stefaan Poedts. The Astrophysical Journal, 954(2):184 (2023) [161]

not only with suprathermal electrons but also with the core subpopulation. Thus, to comprehensively understand the kinetic processes influencing the dynamics of electron populations in the solar wind, it is essential to develop a theoretical framework that incorporates the interplay between these sources of instabilities, rather than isolating them for analysis. Consequently, our current focus shifts towards expanding our previous work by employing an extended CS model that incorporates both sources of free energy: the skewness and the intrinsic anisotropies of the strahlo or core populations. These anisotropies are quantified by $A_s = \left(\frac{\theta_\perp}{\theta_\parallel}\right)^2$ and $A_c = \left(\frac{\alpha_\perp}{\alpha_\parallel}\right)^2$. This approach enables us to analyze the impact of anisotropy and skewness on the whistler heat flux instability (WHFI) and whistler-cyclotron instabilities (WCIs).

In this chapter, we initiate the linear dispersion analysis directing our focus toward the excitation of the parallel propagating whistler mode driven unstable by a skewed electron distribution with an anisotropic strahlo subpopulation. To distinctly examine the influence of the suprathermal subpopulation, we fix the anisotropy of the core at $A_c = 1.0$, to ensure the instabilities are driven solely by the interplay between skewness and strahlo anisotropy, controlled by δ and A_s, respectively. To conduct our stability analysis, we numerically solve the dispersion relation $\omega = \omega(k)$, utilizing the Core-Strahlo (CS) model to describe the electrons and a Maxwellian distribution with $\beta_{\parallel p} = 0.01$ for characterizing the proton population. This approach ensures that only the electrons contribute free energy to the system. Our considerations in this analysis are inspired by parameters observed in the solar wind. The strahlo-to-core parallel temperature ratio and the kappa parameter are set to $T_{\parallel s}/T_{\parallel c} = 7.0$ and $\kappa = 3.0$, respectively [54, 86]. The relative density of the strahlo is set to either 5% or 10% ($\eta_s = 0.05, 0.1$). Additionally, the skewness parameter δ ranges from 0.0 to 0.25, while the anisotropy varies between $0.8 \leq A_s \leq 3.0$ for the suprathermal population. We adjust the magnetic field to fix the electron frequency ratio at $\omega_{pe}/|\Omega_e| = 200$ and the beta parameter for the strahlo to either $\beta_{\parallel} = 0.05$ or $\beta_{\parallel} = 0.1$. Although these values of $\beta_{\parallel s}$ are frequently observed in the solar wind for the suprathermal population, they tend to lean toward the lower end [86]. Given the strong dependence of the WCI on beta, we deliberately chose these values to effectively study the interplay between the anisotropy and skewness of the electron distribution.

6.1 Strahlo-driven whistler-cyclotron instability

Considering that the WCI has never been studied within the framework of the CS model, our initial step is to investigate this instability in the symmetric case ($\delta = 0$), where the free energy is provided solely by the strahlo anisotropy. We regard this case as a reference point to subsequently analyze the modifications introduced by skewness to the stability of the whistler mode. Consequently, in Figure 6.1, we observe the well-known WCI. Panel 6.1(a) illustrates the dispersion relation of the whistler mode for various values of the strahlo anisotropy ($A_s = 0.8, 1.0, 1.2$, and 1.3). The top and bottom plots display the real and imaginary parts of the frequency (ω_r and γ, respectively) as functions of the wave number (k). Frequencies are presented in units of the electron gyrofrequency ($|\Omega_e|$), and wavenumbers are in units of the electron inertial length (c/ω_{pe}). For these plots, we fixed the strahlo density at 10% and the strahlo beta parameter at $\beta_{\parallel s} = 0.1$. In this plot, we observe that the real part of the frequency remains essentially unchanged as we modify the value of A_s. On the other hand, the imaginary part is more sensitive to this parameter. The whistler mode only becomes unstable ($\gamma > 0$) for $A_s > 1$, and the trend is that the instability intensifies with higher values of strahlo anisotropy, as expected. The maximum growth rate $\gamma_{\max}$ increases, and the range of wavenumbers where the mode is unstable widens as A_s increases. Furthermore, for the cases presented, positive growth rates are observed for $kc/\omega_{pe} < 0.6$, which aligns with the wavenumber range where the WHFI develops. Additionally, this range is narrower compared to the core-driven WCI, as we will discuss in the subsequent chapter.

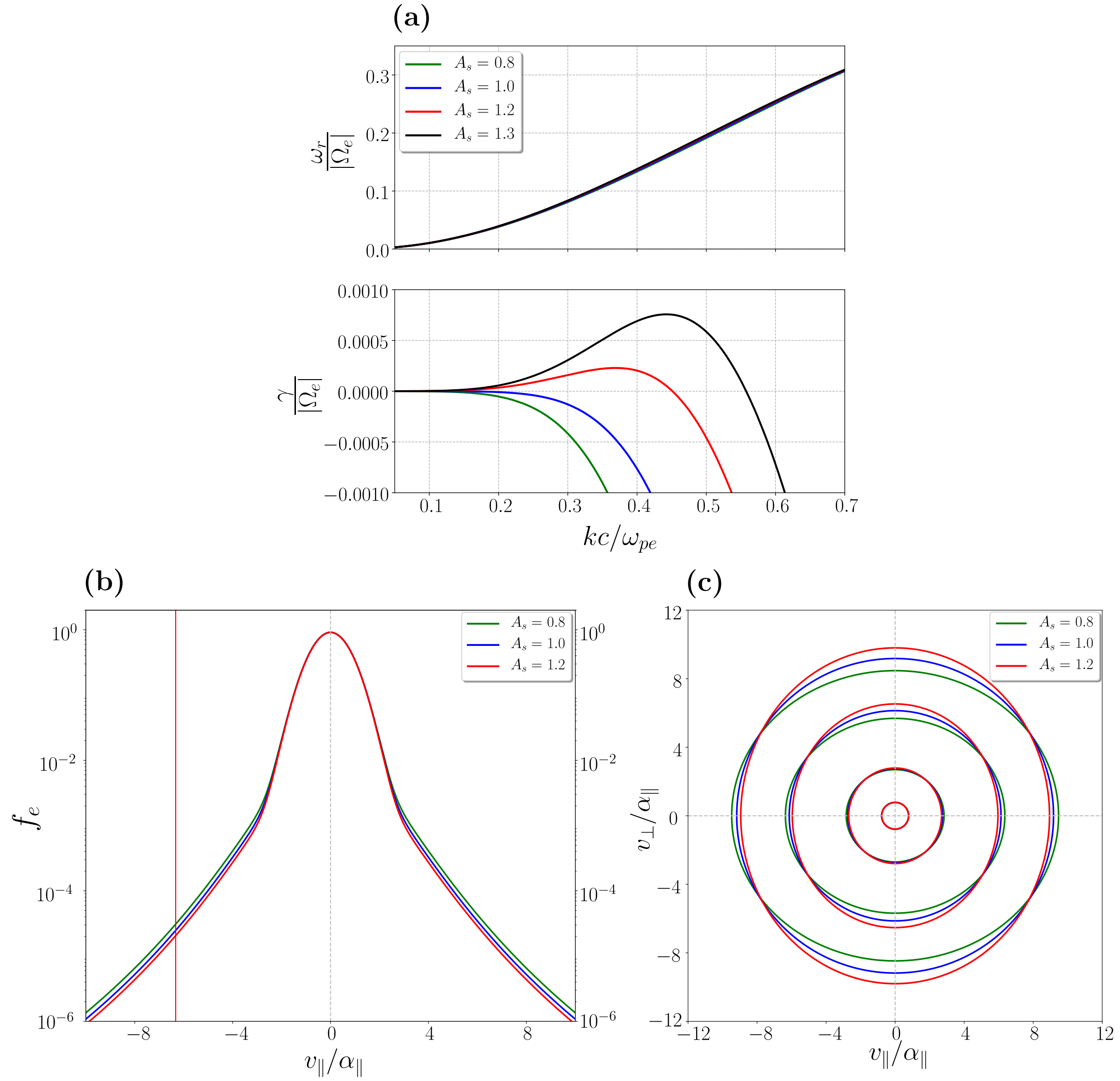

Figure 6.1: (a) Dispersion relation of the whistler mode (b) Parallel cuts at $v_\perp = 0$ of the CS distribution function. (c) Contours of the eVDF. In all panels we use $\eta_s = 0.1$, $\beta_{\parallel s} = 0.1$, $\delta = 0.0$, $A_c = 1.0$, and varying strahlo anisotropy A_s. Different colors represent distinct A_s values: $A_s = 0.8$ (green), 1.0 (blue), 1.2 (red), and 1.3 (black).

To understand the electron configurations that lead to unstable states for the whistler mode, we present in panels 6.1(b) and 6.1(c) a parallel cut at $v_\perp = 0$ and a contour plot of the CS distribution (3.1), respectively, for three different values of the strahlo anisotropy: $A_s = 0.8$ (green), $A_s = 1.0$ (blue), and $A_s = 1.2$ (red). The parallel and perpendicular velocity components (with respect to the background magnetic field) are expressed in units of the core parallel thermal speed $\alpha_\parallel$. We can see that as A_s is modified, keeping A_c constant, the inner contours in the 2D plot remain basically unchanged. However, the outer contours get elongated for $A_s \neq 1$. Only one of these cases is able to excite the whistler mode, corresponding to $A_s = 1.2$, where the distribution shape elongates in the $v_\perp$ direction (indicated by red lines). The same pattern is observed in the 1D plot (panel b in the figure), where changing A_s modifies only the tails of the distribution, while the core portion remains unchanged. Furthermore, in the 1D plot, we also depict the resonant velocity of the most unstable mode, calculated using Eq. (6.1). For the case with $A_s = 1.2$, the most unstable wave configuration occurs at $kc/\omega_{pe} = 0.37$, corresponding to a maximum growth rate of $\gamma_{\max}/|\Omega_e| = 2.3 \times 10^{-4}$. The respective real part of the frequency for this configuration is $\omega_r/|\Omega_e| = 0.12$. Therefore, the resonant velocity (v_{res}), given by:

$$v_{\text{res}} = \frac{\omega_r + \Omega_e}{k} \tag{6.1}$$

has a value of $v_{\text{res}} = -6.33\,\alpha_\parallel$, which lies in the strahlo part of the distribution. This aligns with expectations as the strahlo is the population providing the free energy for radiation. We also calculated the resonance term, ξ, for the most unstable mode in the $A_s = 1.2$ case according to:

$$\xi = \frac{v_{\text{res}}}{\theta_\parallel} = \frac{\omega_r + \Omega_e}{k\theta_\parallel}, \tag{6.2}$$

which has a value of $\xi = -2.39$. Hence, we are describing a resonant interaction [133], which is expected for the WCI.

6.2 Effect of skewness on the strahlo-driven WCI

In this section, we explore how the previously observed behavior is modified by the skewness parameter, focusing on cases where $\delta > 0$. In other words, we now study how the strahlo-driven WCI changes when the electron distribution also exhibits field-aligned skewness, thus introducing an extra source of free energy into the system. Figure 6.2 illustrates the normalized growth rates of the parallel propagating whistler mode, driven unstable by the strahlo anisotropy. Throughout the panels, we consider a fixed anisotropy of $A_s = 1.5$, a triggering value for the WCI, often observed in the solar wind for the suprathermal subpopulation. In this figure, we observe how the growth rates are modified as the skewness parameter δ increases from the baseline $\delta = 0$ to $\delta = 0.25$, represented by black and blue lines, correspondingly. To generate these plots, we considered different combinations of η_s and β_s to also observe the dependency of the dispersion properties on these parameters. In the upper and bottom panels, we set the strahlo beta parameter to $\beta_{\|s} = 0.05$ and $\beta_{\|s} = 0.1$, respectively. In the left and right panels, we show the growth rates for $\eta_s = 0.05$ and $\eta_s = 0.1$, respectively. The real part of the frequencies is not presented here, as they remain practically unaffected by changes in skewness. The effect of $\delta > 0$ is to enhance the growth rates in such a way that the higher the δ value, the more unstable the wave mode becomes, a pattern observed across all panels. As δ increases, the maximum growth rate achieved also increases, however, it is important to note that the range of unstable wave numbers remains essentially the same. Zooming into the left and right panels, we observe that, for a constant strahlo relative density, increasing the strahlo beta parameter amplifies the growth rates, making the plasma more unstable in the whistler mode. The maximum growth rate achieved by the mode increases almost two times when we double the value of $\beta_{\parallel s}$. Nonetheless, the range of wavenumbers where the mode is unstable ($\gamma > 0$) narrows with increasing beta.

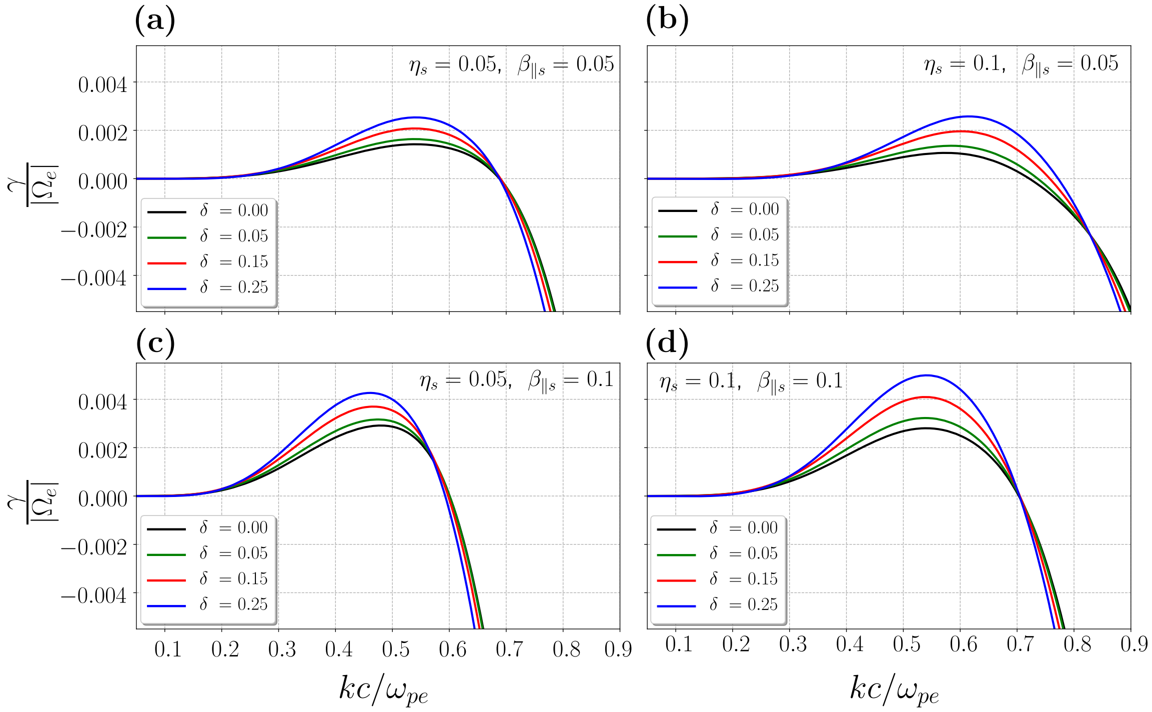

Figure 6.2: Growth rates of the whistler mode for given parameters: $A_c = 1.0$, $A_s = 1.5$, and various skewness parameters: $\delta = 0.0$ (black), $\delta = 0.05$ (green), $\delta = 0.15$ (red) and $\delta = 0.25$ (blue). Each panel corresponds to a specific combination of strahlo density ratio and beta parameter: (a) $\eta_s = 0.05$ and $\beta_{\parallel s} = 0.05$, (b) $\eta_s = 0.1$ and $\beta_{\parallel s} = 0.05$, (c) $\eta_s = 0.05$ and $\beta_{\parallel s} = 0.1$, and d) $\eta_s = 0.1$ and $\beta_{\parallel s} = 0.1$.

Examining the upper panels in Figure 6.2, it is evident that for $\beta_{\parallel s} = 0.05$, the lowest beta value depicted, the strahlo number density plays a small role on the stability of the wave mode. Doubling the value of η_s barely alters the maximum growth rate for higher δ values. However, for the lowest δ values shown, specifically $\delta = 0.0$ and

$\delta = 0.05$, there is a slight decrease in growth rates. This is an unexpected behavior because we are increasing the number density of the population that gives the free energy to the waves and could be attributed to the dominance of the magnetic field in the dynamics of the system at low beta. Shifting our attention to the bottom panels and focusing on $\beta_{\|s} = 0.1$, we observe the expected behavior. The mode becomes increasingly unstable with η_s, resulting in higher maximum growth rates and a broader range of unstable wavenumbers as the strahlo density ratio increases. In summary, considering eVDFs with $\delta > 0$ amplifies the strahlo-driven WCI, which was already present in the system due to the anisotropic distribution of the suprathermal population, as shown in Figure 6.1. This contrasts with the behavior of the core-driven WCI, as we will explore in the next chapter.

To understand how skewness ($\delta > 0$) affects an eVDF already unstable to the strahlo-driven WCI, we examine in Figure 6.3 the changes introduced by an increasing skewness parameter δ on the CS distribution. The corresponding dispersion relations are also presented, in a similar style to Figure 6.1. For these plots, we consider a fixed anisotropic electron configuration with $A_s = 1.5$, a relative strahlo density of 10% ($\eta_s = 0.1$), and a strahlo beta parameter of $\beta_{\|s} = 0.1$. In panel 6.3(a), we display the dispersion relation for three distinct skewness parameter values: $\delta = 0.0$ (green lines), $\delta = 0.1$ (blue lines), and $\delta = 0.2$ (red lines). Here, we observe that skewness amplifies the WCI, resulting in increased growth rates. Remarkably, the real part of the frequency remains nearly unaffected as we modify this parameter.

Panels 6.3(b) and 6.3(c) illustrate the corresponding electron distributions responsible for the dispersion relations depicted in 6.3(a). Specifically, panel 6.3(b) displays a parallel cut at $v_\perp = 0$ of the CS distribution (3.1). Again, the parallel velocity is expressed in units of the core parallel thermal speed $\alpha_\|$. As expected, we

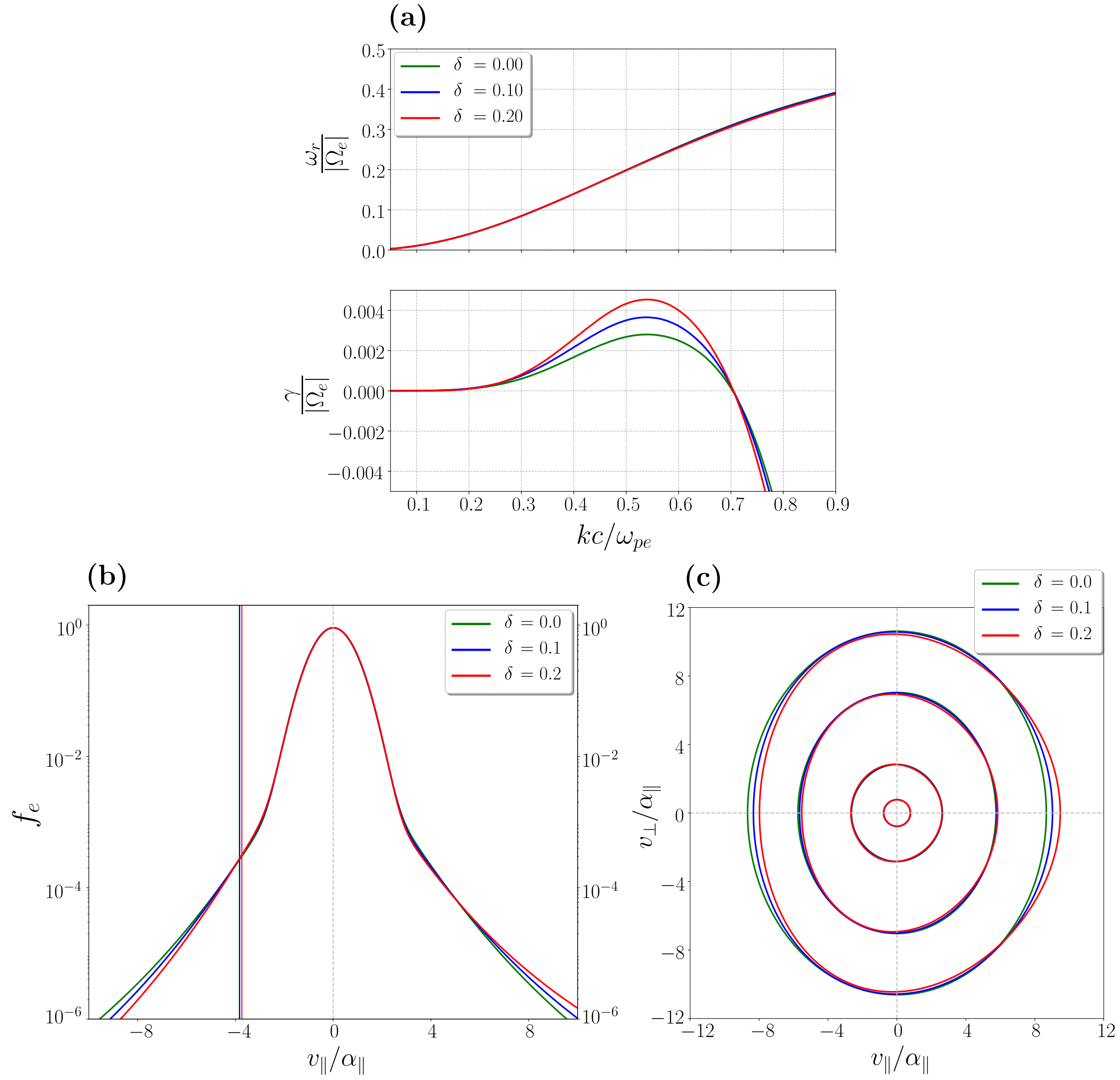

Figure 6.3: (a) Dispersion relation of the whistler mode (b) Parallel cuts at $v_\perp = 0$ of the CS distribution function. (c) Contours of the eVDF. In all panels we use $\eta_s = 0.1$, $\beta_{\parallel s} = 0.1$, $A_s = 1.5$ and $A_c = 1.0$ and different values of the skewness parameter δ. Different colors represent distinct δ values: $\delta = 0.0$ (green), 0.1 (blue) and 0.2 (red).

observe a clear trend: as δ increases, the overall distribution f_e becomes progressively more skewed. In addition, we have plotted the resonant velocity v_{res} of the most unstable mode, calculated using Eq. (6.1), for all three unstable electron configurations. These resonant velocities lie on the strahlo part of the distribution, given that this is the subpopulation providing the necessary free energy to excite the whistler mode. Moreover, the value of $v_{\rm res}$ exhibits minimal variation with increasing δ, primarily due to the weak dependency of both ω_r and the unstable wavenumber range on the skewness parameter. For $\delta = 0.2$, the maximum growth rate peaks at $\gamma_{\rm max}/|\Omega_e| = 4.5 \times 10^{-3}$ with $kc/\omega_{pe} = 0.54$. The corresponding real frequency is $\omega_r/|\Omega_e| = 0.22$. Consequently, the resonant velocity is determined as $v_{\rm res} = -3.74\,\alpha_\parallel$, and the resonant term is $\xi = -1.45$, indicating a resonant interaction.

On the other hand, panel 6.3(c) presents a contour plot of the total electron distribution (3.1). Velocity values are once again expressed in units of the core parallel thermal speed $\alpha_\parallel$. Notably, δ affects only the outer contours, resulting in a progressively skewed distribution as this parameter increases. Furthermore, in the outer contours of this plot, we can distinctly identify the two nonthermal features crucial to this analysis: strahlo anisotropy and skewness, both contributing to the instability of the whistler mode.

6.3 Effect of strahlo anisotropy on the WHFI

To further investigate the combined effect of the skewness parameter δ and the strahlo anisotropy A_s on the stability of the whistler mode, we shift our focus to the influence A_s has on the WHFI, which we know is triggered by skewed electron distributions. In other words, we now examine how the WHFI is modified when the suprathermal electron population also exhibits temperature anisotropy, introducing an additional source of free energy. The WHFI instability was extensively analyzed for the isotropic case within the context of the CS model in Chapter 4 and 5. In those chapters, it was demonstrated that the plasma becomes unstable to the whistler mode when $\delta > 0$, with the growth rates increasing as δ values rise.

To observe how this behavior is altered with an anisotropic electron configuration, we present in Figure 6.4 the normalized growth rates of the whistler mode, driven unstable by the strahlo skewness with $\delta = 0.25$, a triggering value for the WHFI. Across all panels, we observe the changes in γ as the strahlo anisotropy A_s varies from $A_s = 0.8$ to $A_s = 1.2$. The plots are generated using various combinations of η_s and $\beta_{\|s}$, allowing us to also analyze how the dispersion properties depend on these key plasma parameters. In the upper panels, $\beta_{\|s}$ is set to 0.05, while in the bottom panels, we showcase the growth rates for $\beta_{\|s} = 0.1$. Furthermore, in the left and right panels, we fix the relative strahlo number density at 5% and 10%, respectively. A notable observation in all panels is that the effect of the strahlo anisotropy is to inhibit the instability in cases where $A_s < 1$. It is known that such anisotropic cases alone cannot excite the whistler mode, so it is reasonable that they do not enhance the WHFI either. Conversely, plasma states with strahlo anisotropies $A_s > 1$ exhibit the opposite effect, significantly enhancing the WHFI. For these specific electron configurations, we observe that as A_s increases, the whistler mode becomes increasingly unstable. Both the maximum growth rates achieved and the range of unstable wavenumbers expand with increasing A_s, aligning with the behavior reported in Shaaban et al. [107].

Moreover, when focusing on the upper and bottom panels and comparing growth rates for different strahlo densities while keeping $\beta_{\|s}$ fixed, we observe a weak dependence of the instability on η_s, aligning with the trend seen in Figure 6.2. This suggests that, at these low beta values, plasma dynamics are primarily influenced by magnetization. For $\beta_{\|s} = 0.05$, we notice a slight decrease in growth rate values when doubling the density of the suprathermal population. However, this change is

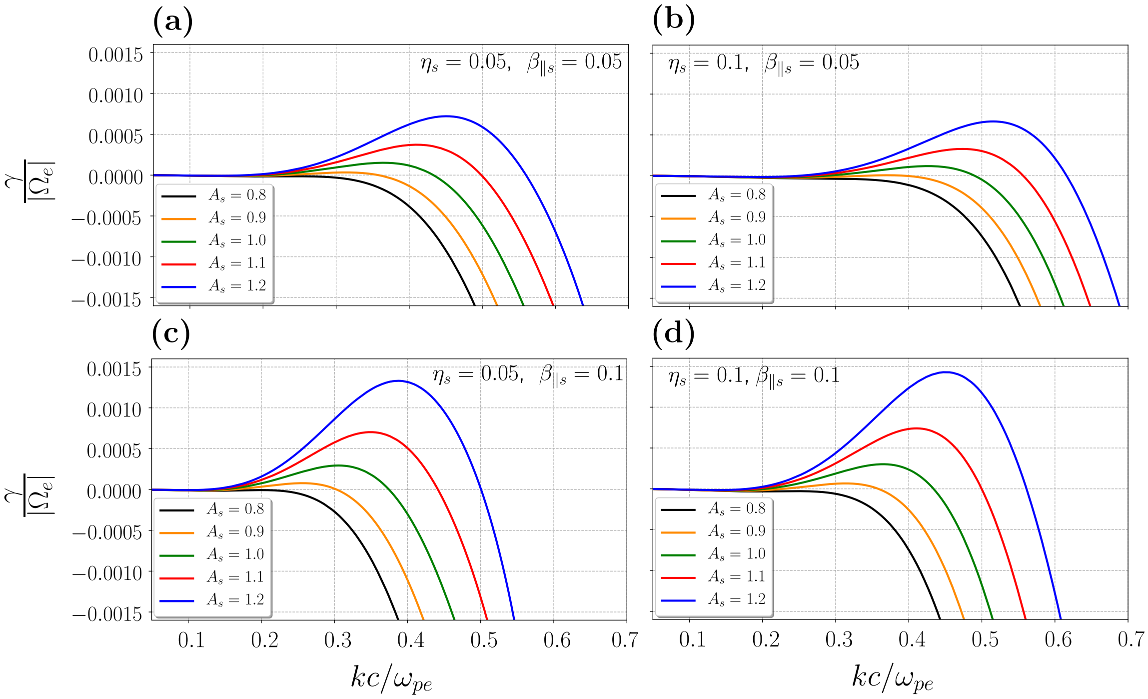

Figure 6.4: Growth rates of the whistler mode for given parameters: $A_c = 1.0$, $\delta = 0.25$ and different strahlo anisotropy: $A_s = 0.8$ (black lines), $A_s = 0.9$ (orange lines), $A_s = 1.0$ (green lines), $A_s = 1.1$ (red lines) and $A_s = 1.2$ (blue lines). Each panel corresponds to a specific combination of strahlo density ratio and beta parameter: (a) $\eta_s = 0.05$ and $\beta_{\parallel s} = 0.05$, (b) $\eta_s = 0.1$ and $\beta_{\parallel s} = 0.05$, (c) $\eta_s = 0.05$ and $\beta_{\parallel s} = 0.1$, and (d) $\eta_s = 0.1$ and $\beta_{\parallel s} = 0.1$.

nearly imperceptible for all considered anisotropy values. This behavior is also observed for $\beta_{\parallel s} = 0.02$ (not shown here). In contrast, for $\beta_{\parallel s} = 0.1$, we observe a minor increase in the maximum growth rate achieved, primarily noticeable in the blue lines ($A_s = 1.2$). Additionally, when comparing different values of $\beta_{\parallel s}$ for a fixed strahlo density, we note that the mode becomes more unstable as $\beta_{\parallel s}$ increases. The maximum growth rates increase with beta, while the unstable wavenumber range narrows, aligning with the behavior observed in Figure 6.2 and the expected dependence on this parameter as the plasma becomes less magnetized.

To explore deeper the interplay between strahlo anisotropy and field-aligned skewness, Figure 6.5 and 6.6 presents a comprehensive analysis of how alterations in A_s

influence both the dispersion relation of the parallel propagating whistler mode and the underlying electron distribution, initially susceptible to the WHFI. In the upper panels, we illustrate the real and imaginary parts of the normalized frequency as functions of the normalized wavenumber for various strahlo anisotropy values. The bottom left and bottom right panels provide parallel cuts at $v_\perp = 0$ and contour plots of the total electron distributions, respectively. These distributions supply the energy to excite the whistler mode and produce the corresponding dispersion relations in the upper panel. For these plots, we set the strahlo relative density to 10%, the strahlo beta parameter to $\beta_{\| s} = 0.1$, and $\delta = 0.2$. Figure 6.5 focus on moderate strahlo anisotropy values typically observed in the solar wind [86], specifically $A_s = 0.8$ (green lines), $A_s = 1.0$ (blue lines), and $A_s = 1.2$ (red lines). In panel 6.5(a), we observe that plasma states with $A_s > 1$ significantly enhance the instability, while states with $A_s < 1$ inhibit the growth rates, consistent with the behavior observed in the previous plot. Notably, the instability disappears entirely for the case $A_s = 0.8$.

In the 1D plot of panel 6.5(b), the electron distribution clearly exhibits skewness. Further, the effect of changing A_s on the distribution shape is to slightly enhance the tails while maintaining the core unchanged. Additionally, we include the resonant velocity v_{res} of the most unstable wave mode, derived from Eq. (6.1), for the two unstable cases presented ($A_s = 1.0$ and $A_s = 1.2$). These resonant velocities consistently align with the strahlo part of the distribution. For $A_s = 1.2$, v_{res} is closer to 0, indicating a greater number of particles available for interaction with the wave. In the most unstable case, $A_s = 1.2$, the maximum growth rate achieved is $\gamma_{\max}/|\Omega_e| = 1.2 \times 10^{-3}$ at $kc/\omega_{pe} = 0.44$. The corresponding real part of the frequency is $\omega_r/|\Omega_e| = 0.16$, resulting in a resonant velocity of $v_{\mathrm{res}} = -4.9\,\alpha_\|$ and a resonant term $\xi = -1.92$, indicating a resonant interaction. In panel 6.5(c), the 2D

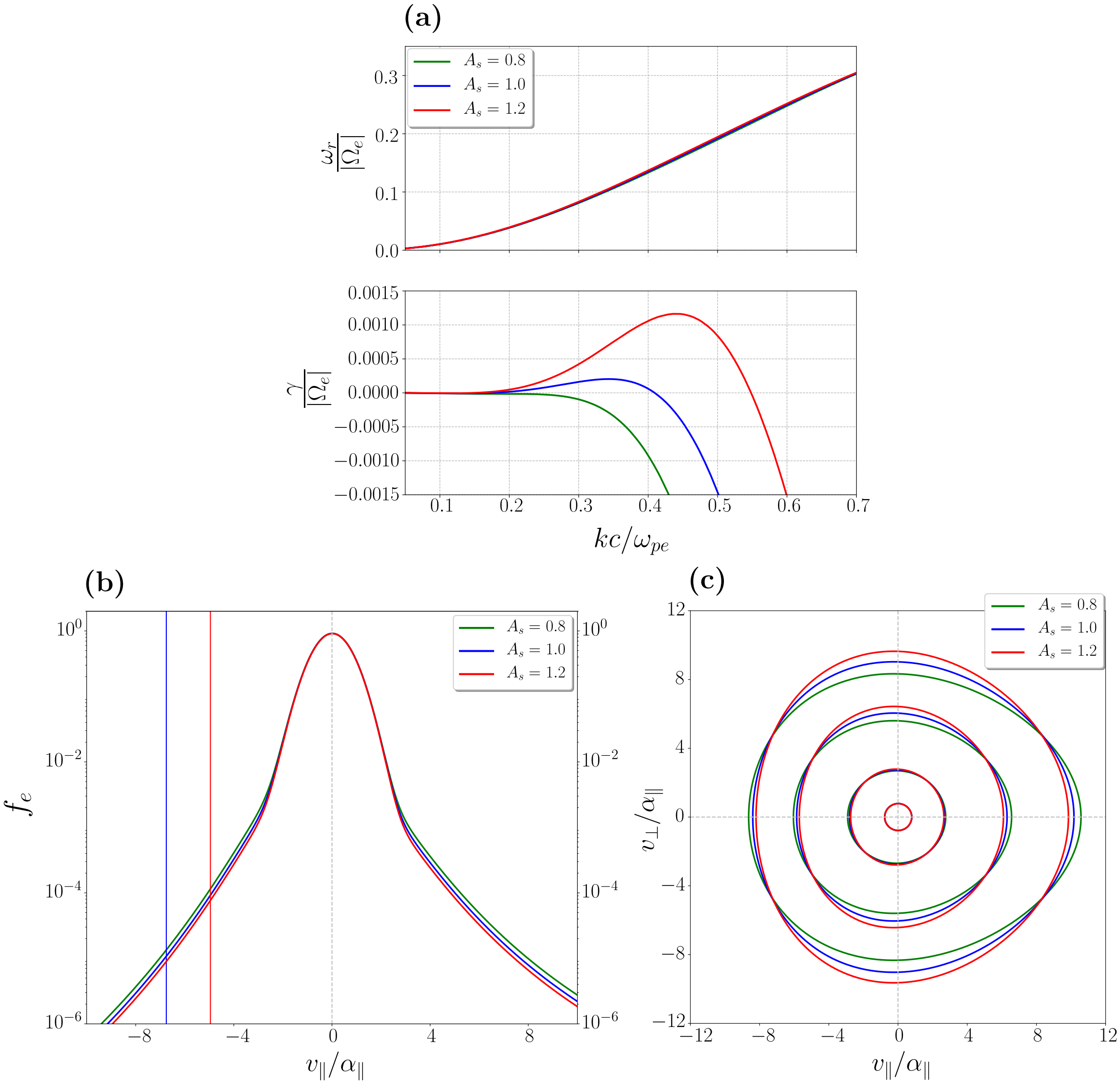

Figure 6.5: (a) Dispersion relation of the whistler mode (b) Parallel cuts at $v_\perp = 0$ of the CS distribution function. (c) Contours of the eVDF. In all panels we use $\eta_s = 0.1$, $\beta_{\parallel s} = 0.1$, $\delta = 0.2$, $A_c = 1.0$, and varying strahlo anisotropy A_s. Different colors represent distinct A_s values: $A_s = 0.8$ (green), 1.0 (blue) and 1.2 (red).

plot demonstrates that varying A_s predominantly modifies the outer contours while leaving the inner contours, describing the core part of the distribution, almost unchanged. Furthermore, for these moderate A_s values, it is still possible to distinguish both kinetic features at play in this scenario: field-aligned skewness and anisotropy.

In Figure 6.6, we present analogous information as shown in Figure 6.5, but this

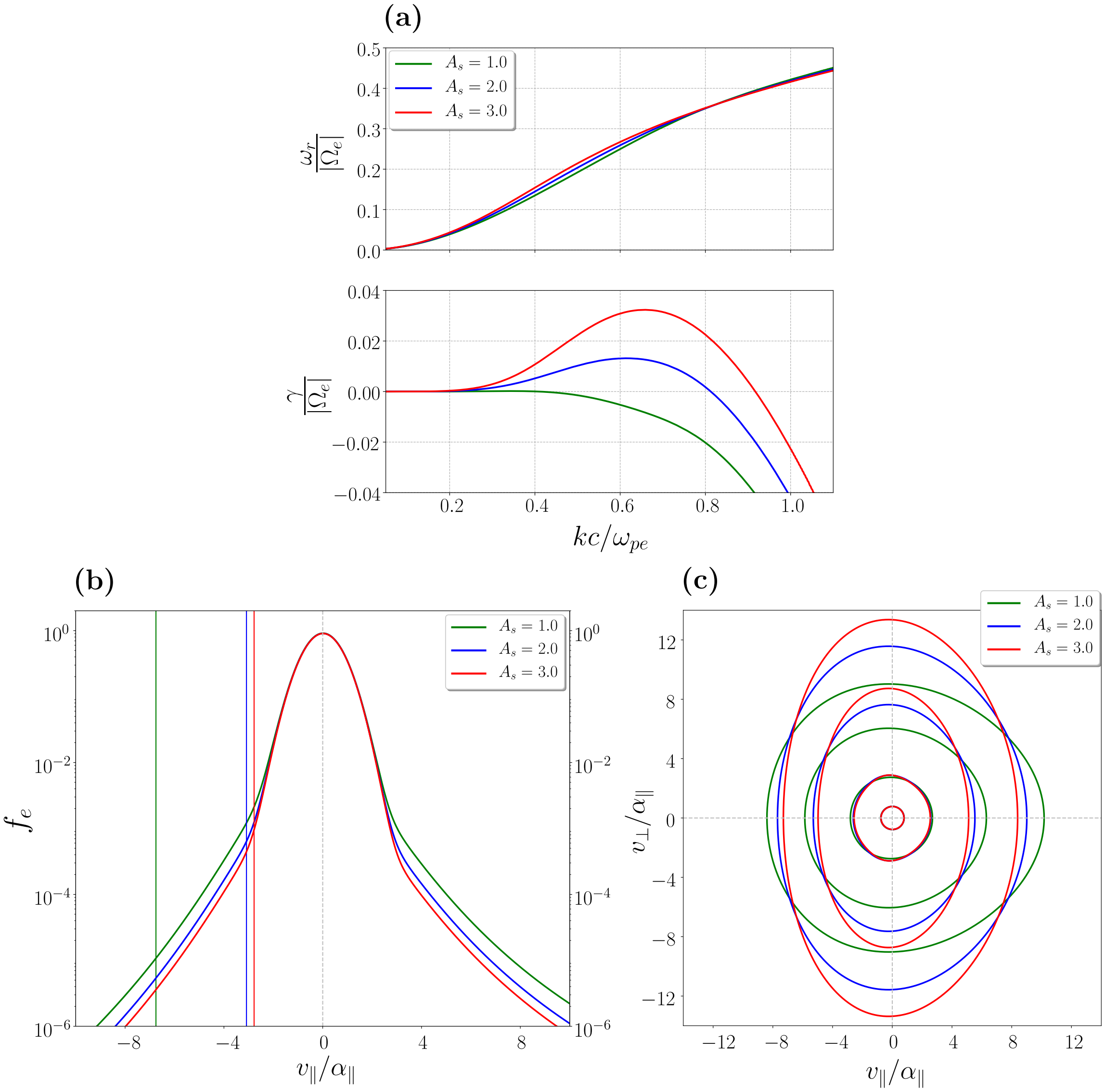

Figure 6.6: (a) Dispersion relation of the whistler mode (b) Parallel cuts at $v_\perp = 0$ of the CS distribution function. (c) Contours of the eVDF. In all panels we use $\eta_s = 0.1$, $\beta_{\parallel s} = 0.1$, $\delta = 0.2$, $A_c = 1.0$, and varying strahlo anisotropy A_s. Different colors represent distinct A_s values: $A_s = 1.0$ (green), 2.0 (blue) and 3.0 (red).

time for higher strahlo anisotropy values: $A_s = 1.0$ (green lines), $A_s = 2.0$ (blue lines), and $A_s = 3.0$ (red lines). Panel 6.6(a) illustrates that the growth rates are significantly amplified by the strahlo anisotropy, with both the maximum growth rate and the unstable wavenumber range exhibiting a strong dependence on this parameter. Doubling the value of A_s from $A_s = 1.0$ to $A_s = 2.0$ increases the maximum growth rate $\gamma_{\max}$ almost 65 times. The 1D plot in panel 6.6(b) once again highlights the skewness of the distribution. Notably, increasing A_s tends to reduce the energetic tails while maintaining their slope, with these changes being more pronounced this time. For the three unstable configurations presented, vertical lines representing the resonant velocity v_{res} of the most unstable wave mode are overplot. It is evident that as A_s increases and the wave becomes more unstable, v_{res} moves to the right, even closer to 0 than in the previous case, signifying a greater number of particles available for interaction with the wave. For the most unstable case shown, $A_s = 3.0$, the peak growth rate is achieved at $kc/\omega_{pe} = 0.66$. The corresponding real and imaginary parts of the frequency are $\omega_r/|\Omega_e| = 0.29$ and $\gamma_{\max}/|\Omega_e| = 3.23 \times 10^{-2}$. Consequently, the resonant velocity is $v/\alpha_{\parallel} = -2.78$, and the resonant term is $\xi = -1.08$. Lastly, the 2D plot in panel 6.6(c), shows the pronounced influence of changing A_s, which now extremely modifies the outer contours of the distribution. For $A_s = 2.0,\ 3.0$, the shape is distinctly dominated by strahlo anisotropy, overshadowing the skewness, which is barely noticeable.

6.4 Discussion

In this chapter, we employed linear kinetic theory to conduct a thorough investigation into the excitation of the parallel-propagating whistler mode, triggered by electron populations exhibiting both skewness and anisotropy, in a non-collisional and magnetized plasma. Our goal was to explore the interplay between these suprathermal features and their combined impact on the stability of the whistler mode. To achieve this, we utilized the CS model for the electron population, assuming a small electron skewness ($\delta^3 \ll 1$). We numerically solved the dispersion relation $\omega = \omega(k)$ of the whistler mode, considering typical solar wind conditions for the remaining relevant plasma parameters. Furthermore, we systematically isolated the effect of the strahlo by analyzing dispersion properties while maintaining a fixed value for the intrinsic anisotropy of the core, $A_c = 1.0$. This approach ensured that the excitation of the whistler mode was solely driven by the interplay between δ and A_s.

It is important to note that in most works where stability analyses are performed, plots depicting the shape of the unstable distributions are not provided. Therefore, it becomes difficult to observe how they change with different values of relevant plasma parameters affecting the system dynamics. Distributions are crucial in understanding when a mode becomes unstable under given plasma conditions. Hence, having a visual representation of the suprathermal features at play within the system, providing the free energy necessary for wave radiation, aids in developing an intuitive understanding of the system, regardless of the theoretical model chosen to describe the distributions. Consequently, throughout this study, we presented the total electron distribution for a representative number of unstable configurations, allowing us to illustrate how the shape of the electron distribution changes with variations in δ and A_s. This allowed us to gain insight into visually identifying which nonthermal feature is more relevant in exciting the whistler mode.

Our investigation into the combined influence of A_s and δ on the linear stability of the whistler mode has revealed that both strahlo-driven instabilities, the WCI, and the WHFI, exhibit positive growth rates within similar wavenumber ranges, making it challenging to distinguish the suprathermal feature acting as the primary source of free energy in the system, whether it be strahlo anisotropy or skewness. However, for reasonable values of $A_s > 1$, commonly observed in the solar wind, strahlo anisotropy is shown to induce higher growth rates over a broader wavenumber range when compared to instabilities driven by skewness. For instance, the WCI triggered by a plasma state with $A_s = 1.25$ and $\delta = 0$ yields a maximum growth rate of $\gamma/|\Omega_e| = 4.49 \times 10^{-4}$, which is 2.2 times higher than the growth rate produced by the WHFI triggered by a plasma state with a strong skewness of $\delta = 0.2$ and $A_s = 1.0$.

Moreover, for these $A_s > 1$ values typically observed in the solar wind, the changes induced by δ on the strahlo-driven WCI are relatively minor and negligible when considering higher values of A_s. For an anisotropic plasma with $A_s = 1.5$, the maximum growth rate of the instability increases 1.6 times when transitioning from the symmetric case $\delta = 0$ to a scenario with a strong skewness $\delta = 0.2$. On the contrary, the effect of strahlo anisotropy (A_s) on the WHFI is more pronounced. For a skewed plasma configuration with $\delta = 0.2$, the maximum growth rate of the instability increases by a factor of 2.8 when transitioning from the isotropic case ($A_s = 1.0$) to a plasma configuration with a slightly higher anisotropy of $A_s = 1.1$. These results highlight that the anisotropy of the suprathermal population is a more effective and potent source of free energy, significantly destabilizing the whistler mode compared to the field-aligned skewness. Given that both sources of free energy coexist in the solar wind [86], our initial exploration through linear kinetic theory suggests that whistler waves observed in the solar wind are more likely to arise from anisotropy rather than skewness, a trend that seems to align with existing observational findings [103]. This conclusion is particularly relevant for the slow solar wind, which is known to exhibit less pronounced skewness in the electron distributions.

This concludes our exploration of the interplay between anisotropy and skewness as sources of free energy, with the anisotropy solely attributed to the suprathermal population. In the following chapter, we will invert our analysis and focus on studying the interplay between the skewness and the intrinsic core anisotropy as a source of free energy for the excitation of the parallel propagating whistler mode.

Chapter 7

Interplay between skewness and core anisotropy [†]

In this chapter, we extend the linear dispersion analysis initiated in the previous chapter by focusing on the role of an anisotropic core population. Our primary goal is to explore the interplay between core anisotropy and field-aligned skewness in driving the excitation of the parallel propagating whistler mode. To conduct a comprehensive stability analysis, we maintain the same plasma configuration established in the preceding chapter for both protons and electrons. However, this time we fix the intrinsic anisotropy of the strahlo population at $A_s = 1.0$ and vary the anisotropy of the core population in the range $0.5 \leq A_c \leq 3.0$. This ensures that the whistler mode is driven unstable solely by the free energy contributed by the core anisotropy and skewness of the electron distribution, features controlled by δ and A_c, respectively.

[†] This chapter is based on information included in the article: *Interplay between Anisotropy- and Skewness-driven Whistler Instabilities in the Solar Wind under the Core–Strahlo Model.*, **Bea Zenteno-Quinteros**, Pablo S. Moya, Marian Lazar, Adolfo F. Viñas, & Stefaan Poedts. The Astrophysical Journal, 954(2):184 (2023) [161].

7.1 Core-driven whistler-cyclotron instability

Building upon the approach from the previous chapter, we start our investigation by exploring the whistler-cyclotron instability (WCI) in the symmetric scenario, where $\delta = 0$, and the free energy is exclusively provided by the anisotropy of the core ($A_c \neq 1$). This preliminary analysis establishes a baseline for our subsequent examination of how skewness influences the stability of the whistler mode.

Figure 7.1 provides an overview of the core-driven WCI. Panel 7.1(a) displays the dispersion relation of the whistler mode, varying the core anisotropy A_c. The top and bottom panels illustrate the real and imaginary parts of the frequency, respectively, both normalized to the electron gyrofrequency $|\Omega_e|$ and presented as a function of the normalized wavenumber kc/ω_{pe}. For these plots, we maintain the strahlo density ratio at $\eta_s = 0.1$ and the strahlo beta parameter at $\beta_{\|s} = 0.1$. This panel distinctly showcases that changes in A_c significantly influence ω_r compared to other parameters, resulting in an enhancement of the real frequency with increasing core anisotropy. Moreover, the real frequencies achieved with an anisotropic core are notably higher than those resulting from the strahlo-driven WCI (see Figure 6.1(a) for comparison), which may help in the differentiation of the subpopulation providing the energy to excite the whistler mode. For instance, in two anisotropic configurations generating similar maximum growth rates ($A_s = 2.0$ and $A_c = 2.4$), the respective real parts of the frequency are nearly twice as high when the anisotropy arises from the core ($\omega_r/|\Omega_e| = 0.27$ and $\omega_r/|\Omega_e| = 0.50$, respectively).

Regarding growth rates, significantly higher levels of anisotropy are required to trigger the WCI when the energy originates from the core population instead of the strahlo. The transition from stability to instability occurs at approximately $A_c \approx 2.2$.

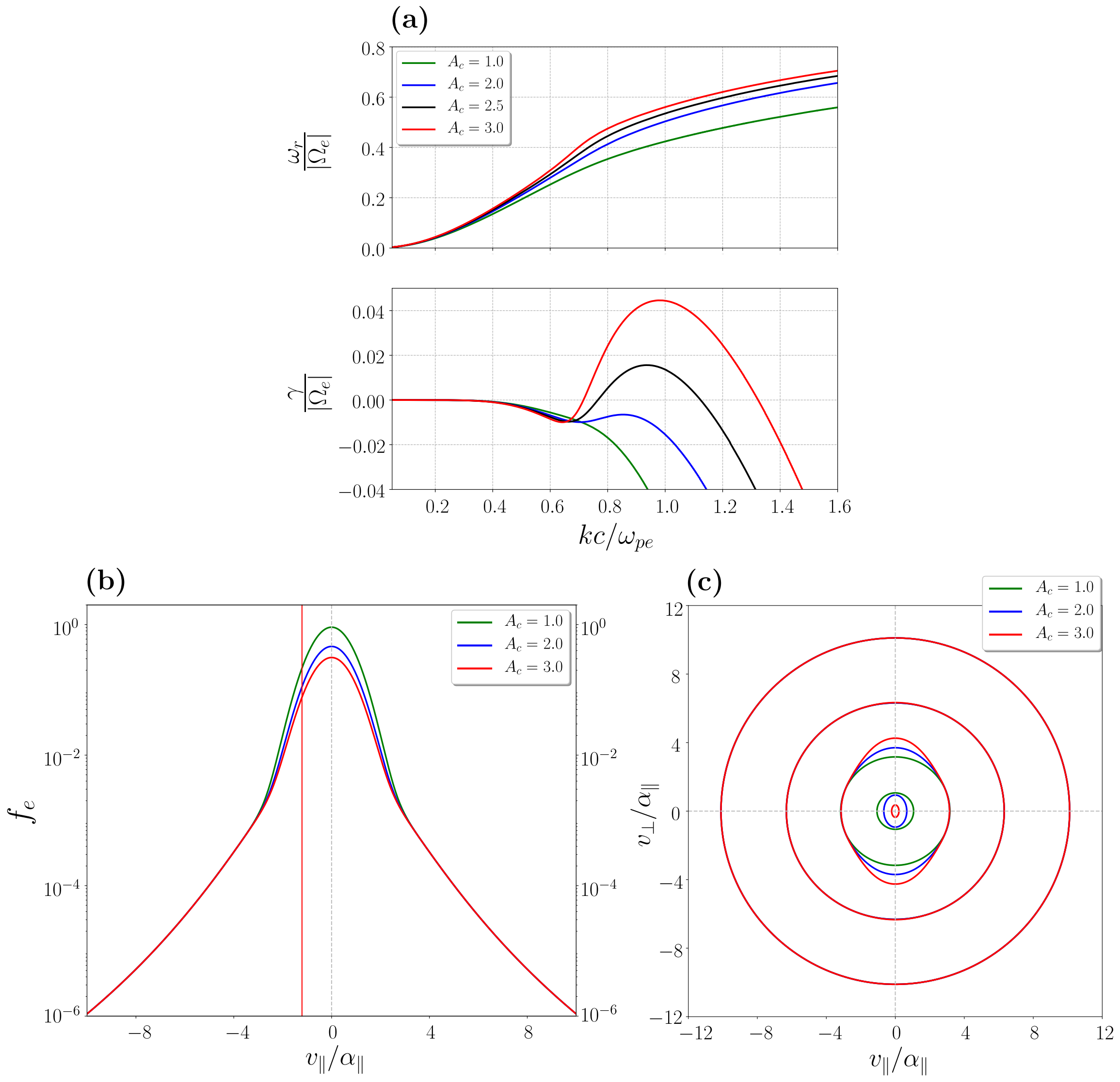

Figure 7.1: (a) Dispersion relation of the whistler mode (b) Parallel cuts at $v_\perp = 0$ of the CS distribution function. (c) Contours of the eVDF. In all panels we use $\eta_s = 0.1$, $\beta_{\parallel s} = 0.1$, $\delta = 0.0$, $A_s = 1.0$, and varying core anisotropy A_c. Different colors represent distinct A_c values: $A_c = 1.0$ (green), 2.0 (blue), 2.5 (black), and 3.0 (red).

For lower anisotropy values, including cases where $A_c < 1$, the whistler mode remains stable across all wavenumbers. Notably, a similar transition point for the core-driven WCI is observed in a core-strahl model employing two drifting bi-Maxwellians to describe the electron distribution. This suggests that the presence of high-energy tails is not a significant factor for this instability. Furthermore, the wavenumber range where the mode exhibits positive growth rates is broader for the core-driven instability compared to the strahlo-driven one. For example, for $A_s = 3.0$, the growth rates cross the axis at $kc/\omega_{pe} \approx 0.9$, while for $A_c = 3.0$, this occurs at $kc/\omega_{pe} \approx 1.35$.

To determine the electron configurations that are unstable states for the whistler mode when considering an anisotropic core we present parallel cuts at $v_\perp = 0$ and contour plots of the CS distribution in panels 7.1(b) and 7.1(c). We showcase this information for three different core anisotropy values: $A_c = 1.0$ (green), $A_c = 2.0$ (blue), and $A_c = 3.0$ (red). In the 1D plot, we observe that the effect of A_c on the shape of the distribution is to elevate the core portion as A_c decreases, while mostly maintaining the high-energy tails unchanged. Additionally, we show the resonant velocity v_{res} of the most unstable wave mode, calculated using Eq. (6.1), for the only unstable state depicted ($A_c = 3.0$). In this case, the most unstable wave configuration occurs at $kc/\omega_{pe} = 0.98$, corresponding to a maximum growth rate of $\gamma_{\text{max}}/|\Omega_e| = 4.5 \times 10^{-2}$ and a frequency of $\omega_r/|\Omega_e| = 0.55$. Consequently, the resonant velocity is $v_{\text{res}} = -1.21\alpha_\parallel$, positioning it in the core of the distribution. Furthermore, the resonant term has the value of $\xi = -0.46$, as determined by Eq. (6.2), indicating a resonant interaction. On the other hand, the 2D plot reveals that changes in A_c primarily impact the innermost contours, elongating them in the $v_\perp$ direction as A_c increases. Conversely, the outer contours remain mostly unchanged. This behavior is reasonable considering that we are modifying a parameter specific to the core subpopulation. It is crucial to note that only when the inner contours undergo significant distortion and deviate from their oval shape does the plasma assume an unstable configuration for the whistler mode.

7.2 Effect of skewness on the core-driven WCI

In this section, our focus shifts to investigating how the previously observed behavior is altered with the inclusion of field-aligned skewness as an additional source of free energy. Specifically, we analyze cases where $A_c \neq 1$ and $\delta > 0$. In Figures 7.2 and 7.3, we present the dispersion relation and the total electron distribution (3.1) for an increasing value of the skewness parameter δ, aiming to study the modifications it introduces to the core-driven WCI. The upper panels display the real and imaginary parts of the frequency, normalized to the electron gyrofrequency $|\Omega_e|$, as functions of the normalized wavenumber and for different values of δ. The bottom left and bottom right panels showcase, respectively parallel cuts at $v_\perp = 0$ and contour plots of the electron distributions providing the energy to excite the parallel propagating whistler mode, and producing the dispersion relations shown in the upper panels. To generate these plots, we consider a plasma state with a relative density of the suprathermal population set at 10% ($\eta_s = 0.1$) and a strahlo beta parameter of $\beta_{\|s} = 0.1$.

In Figure 7.2, we present this information for a low value of the core anisotropy A_c. Specifically, we select a value for A_c where, in the symmetric case ($\delta = 0$), the whistler mode remains stable for any k value. Considering the transition point occurs at $A_c \approx 2.2$, we opt for a representative value of $A_c = 1.6$. Panel 7.2(a) illustrates that for this low value of A_c, the initially stable whistler mode (green lines) starts developing positive growth rates as δ increases, becoming increasingly unstable. Furthermore, the wavenumbers at which $\gamma > 0$ are at least half the value of those typical for the core-driven WCI in the symmetric case (compare with Figure 7.1(a)). Therefore, we observe the distinctive behavior of the WHFI within a wavenumber range typical of this instability driven by the strahlo skewness. Importantly, no onset or enhancement of the WCI driven by the core is triggered by the skewness in this scenario.

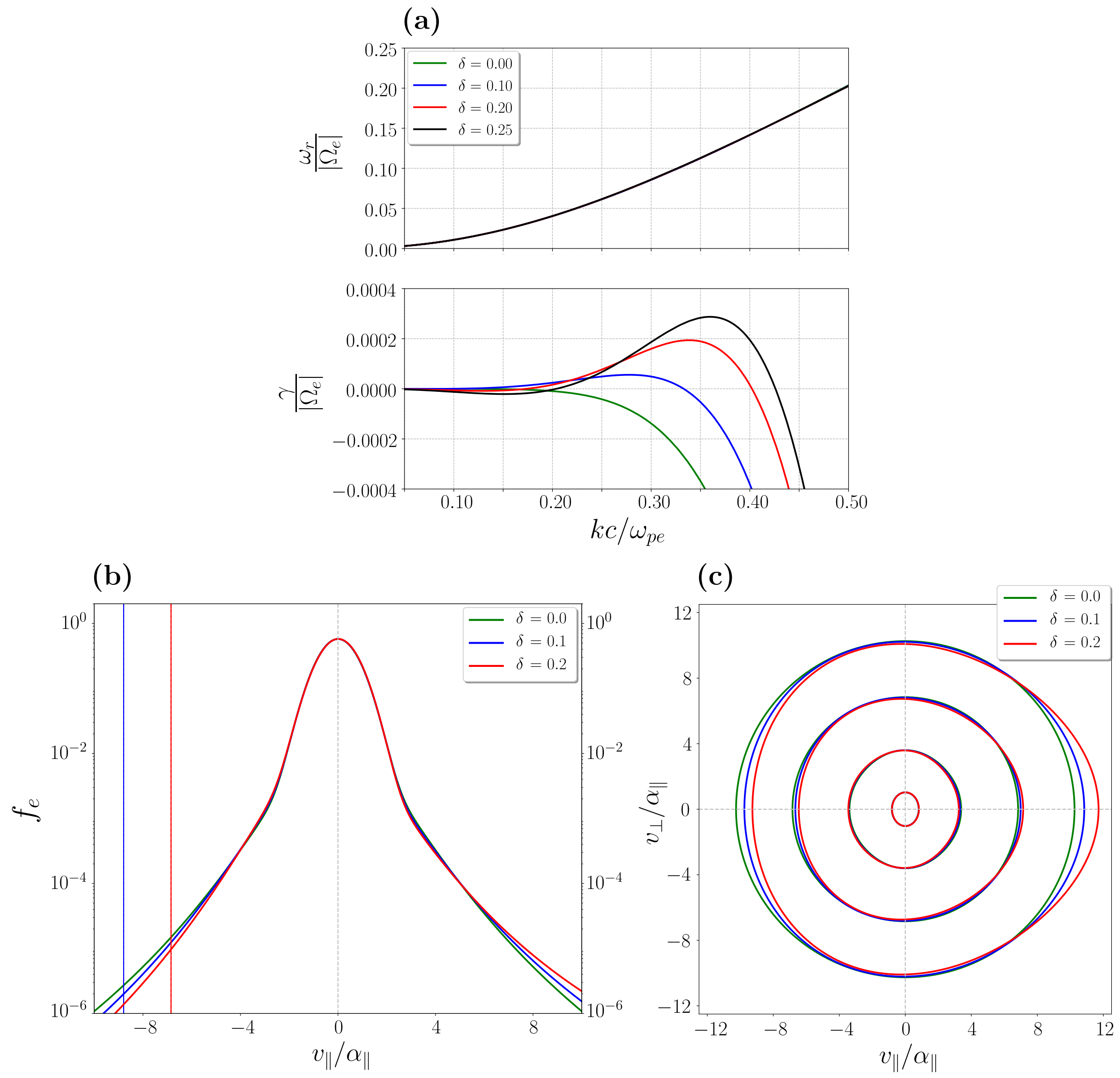

Figure 7.2: (a) Dispersion relation of the whistler mode (b) Parallel cuts at $v_\perp = 0$ of the CS distribution function. (c) Contours of the eVDF. In all panels we use $\eta_s = 0.1$, $\beta_{\parallel s} = 0.1$, $A_s = 1.0$, and $A_c = 1.6$ and different values of the skewness parameter δ. Different colors represent distinct δ values: $\delta = 0.00$ (green), 0.10 (blue), 0.20 (red) and 0.25 (black).

In panel 7.2(b), it is evident that variations in δ lead to modifications in the skewness of the distribution. As expected, the distribution becomes more skewed with increasing δ while the core remains unchanged. We have also included in this plot the resonant velocities v_{res} for the most unstable wave configurations for two unstable states: $\delta = 0.1$ and $\delta = 0.2$. As anticipated, these velocities reside within the strahlo part of the distribution. Thus, for low values of A_c, the instability is completely triggered by the skewness of the strahlo. Notably, at $\delta = 0.2$, the maximum growth rate, the corresponding wavenumber, and real part of the frequency are, respectively, $\gamma_{\max}/|\Omega_e| = 1.9\times 10^{-4}$, $kc/\omega_{pe} = 0.34$, and $\omega_r/|\Omega_e| = 0.11$. This results in a resonant velocity of $v_{\text{res}} = -6.85\alpha_{\|}$ and a resonant term of $\xi = -2.66$, indicating a resonant interaction. Additionally, as the plasma becomes more unstable to the mode, the resonant velocity shifts to higher values of f_e, thus increasing the density of particles capable of interacting with the wave as δ increases. Furthermore, the 2D plot in panel 7.2(c) clearly illustrates that as δ increases, the outer contours of the CS distribution become more skewed, while the inner contours remain unaffected. Also, the elongated inner contours in the $v_{\perp}$ direction indicate a core anisotropy $A_c > 1$. However, these contours are not distorted enough, compared to the isotropic case, to effectively excite the WCI.

To further our analysis, Figure 7.3 presents a similar exploration of the effect of the skewness parameter on the dispersion relation and the total electron distribution. However, in this case, we consider a higher value of the core anisotropy, $A_c = 2.5$ (greater than 2.2), representing an unstable plasma state for the core-driven WCI in the symmetric case ($\delta = 0$). From the dispersion relations depicted in panel 7.3(a), it is evident that δ does not significantly influence the real frequency (ω_r) of the whistler mode. Conversely, the imaginary part exhibits a stronger dependence on this parameter. In this particular case, we present the growth rates on a logarithmic scale, facilitating the distinction of the two peaks with $\gamma > 0$ corresponding to the same mode. The peak at higher wavenumbers is notably more intense, surpassing the one observed at lower wavenumbers by at least two orders of magnitude. This intense

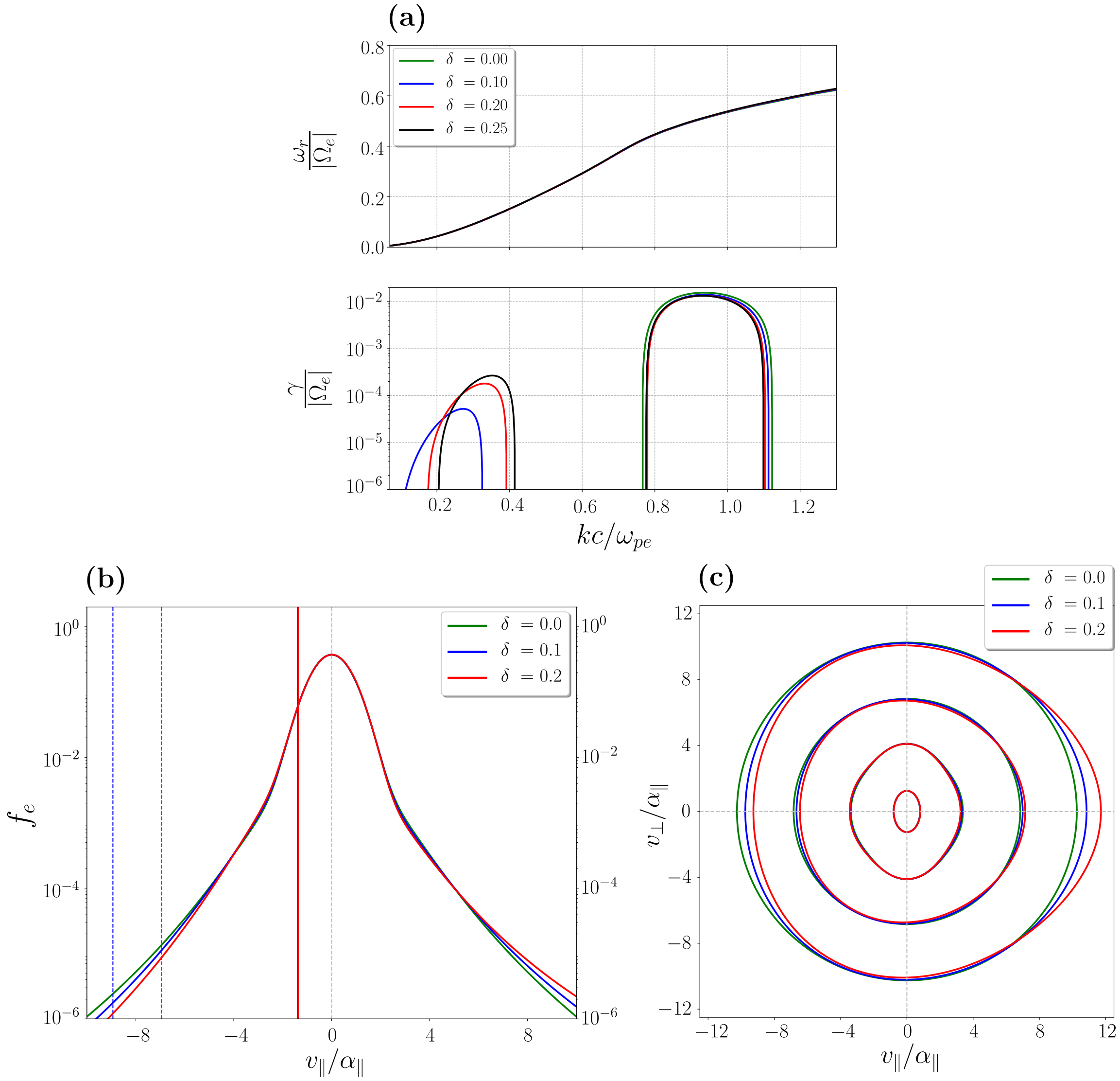

Figure 7.3: (a) Dispersion relation of the whistler mode (b) Parallel cuts at $v_\perp = 0$ of the CS distribution function. (c) Contours of the eVDF. In all panels we use $\eta_s = 0.1$, $\beta_{\parallel s} = 0.1$, $A_s = 1.0$, and $A_c = 2.5$ and different values of the skewness parameter δ. Different colors represent distinct δ values: $\delta = 0.00$ (green), 0.10 (blue), 0.20 (red) and 0.25 (black).

peak aligns with a wavenumber range characteristic of core-driven WCI. Furthermore, modifications in the δ parameter do not significantly impact the growth rate values within this specific k range. On the other hand, the secondary peak appears in a wavenumber range typical of instabilities driven by the strahlo subpopulation.

The mode becomes more unstable as δ increases, a characteristic behavior of the WHFI. Notably, the real frequencies corresponding to the higher wavenumber peak (associated with core-driven WCI) are at least four times higher than those linked to the secondary peak (associated with the WHFI). For $\delta = 0.25$, the respective real frequencies of the most unstable wave configuration are $\omega_r/|\Omega_e| = 0.51$ and $\omega_r/|\Omega_e| = 0.12$, respectively. This distinction offers a potential observational means to identify the subpopulation providing the free energy to excite the whistler mode.

Furthermore, in the 1D plot of panel 7.3(b), we observe a pattern similar to that in panel 7.2(b): the distribution shape becomes increasingly skewed as δ increases, while the core remains unchanged. Resonant velocities (6.1) for the most unstable wave configurations of each peak for two selected unstable states, $\delta = 0.1$ (blue) and $\delta = 0.2$ (red), have been included in the plot. Solid lines represent the resonant velocity of the WCI, which consistently lies in the core portion of the distribution with minimal changes as the skewness of the distribution varies. For $\delta = 0.2$, the most unstable wave configuration for the dominant peak is positioned at $kc/\omega_{pe} = 0.93$, displaying a maximum growth rate of $\gamma_{\max}/|\Omega_e| = 1.3 \times 10^{-2}$ and a frequency of $\omega_r/|\Omega_e| = 0.51$. This translates to a resonant velocity of $v_{\text{res}} = -1.36\alpha_{\|}$ and a resonant term of $\xi = -0.52$. In contrast, dashed lines correspond to the resonant velocities of the WHFI, aligning with the tails of the distribution corresponding to the strahlo subpopulation. Their behavior mirrors that of panel 7.2(b): the resonant velocity shifts to the right as the plasma becomes more unstable, indicating a higher density of particles capable of interacting with the wave as δ increases. For $\delta = 0.2$, the secondary peak occurs at $kc/\omega_{pe} = 0.33$, displaying a maximum growth rate of $\gamma/|\Omega_e| = 1.8 \times 10^{-4}$ and a frequency of $\omega_r/|\Omega_e| = 0.11$. Consequently, the resonant velocity is $v_{\text{res}} = -6.95\alpha_{\|}$, with a resonant term $\xi = -2.7$. These resonant terms confirm that the instability arises from a resonant interaction, proving that it should not be confused with the firehose instability.

Finally, in the 2D plot of panel 7.3(c), we distinctly distinguish the two sources of free energy in this system. The distribution displays elongated and distorted inner contours, responsible for the core-driven WCI. Interestingly, these contours undergo minimal change as δ increases, aligning with the stability of the mode remaining largely unaffected by variations in δ. On the other hand, in the outer contours, we clearly observe the skewness of the CS distribution, providing energy for the less intense WHFI. Thus, we witness the typical behavior of the WHFI: as δ increases, the distribution becomes more skewed, and the plasma becomes more unstable, as evident in the second peak in panel 7.3(a).

7.3 Effect of core anisotropy on the WHFI

To conclude our exploration of the interplay between the skewness parameter δ and the core anisotropy A_c, we now turn our attention to examining the effect A_c has on the WHFI, which we know is triggered by a skewed electron distribution ($\delta \neq 0$). Specifically, we aim to comprehend how the WHFI is altered in the presence of an anisotropic core distribution, which serves as an additional source of free energy in the system. In the isotropic case ($A_c = 1$), the plasma becomes unstable when $\delta > 0$. As this parameter increases, the electron distribution becomes more skewed and the plasma becomes increasingly unstable to the parallel propagating whistler mode. To observe how this behavior is modified, Figure 7.4 illustrates how changes in A_c influence both the dispersion relation and the electron distribution initially susceptible to WHFI. For these plots, we maintain the strahlo density at 10%, set the strahlo beta parameter to $\beta_{\parallel s} = 0.1$, and consider a skewed distribution with $\delta = 0.2$. Panel

7.4(a) displays the real and imaginary components of the normalized frequency as functions of the normalized wavenumber for various A_c values. Notably, ω_r is significantly influenced by A_c, more so than by δ, with frequencies increasing as the core anisotropy increases. Regarding the growth rates, we observe that this time cases with $A_c < 1$ amplify the instability. Both the maximum growth rate and the range of unstable wavenumbers where $\gamma > 0$ increase for anisotropy values less than one. Conversely, cases with $A_c > 1$ exhibit the opposite effect, diminishing the instability as A_c rises. Both the maximum growth rate and the unstable wavenumber range diminish for increasing core anisotropy. However, it is important to highlight that these alterations introduced by the core anisotropy are minor, especially considering the high A_c values presented in this plot. Hence, the WHFI is not as strongly dependent on A_c as it is on the strahlo anisotropy A_s. Therefore, we can conclude that anisotropic core populations do not significantly enhance or diminish the WHFI. Furthermore, we omit higher wavenumber k values in this representation, where the WCI appears, as we already know their dependence on A_c. Additionally, as seen in Figure 7.3, δ does not significantly affect its stability.

To further investigate this interplay, we analyze the electron distribution functions triggering the excitation of the whistler mode and observe how they evolve with changes in A_c. In panels 7.4(b) and 7.4(c), we present parallel cuts at $v_\perp = 0$ and contour plots of the total electron distributions, which provide the energy to excite the whistler mode producing the dispersion relations depicted in the upper panel of Figure 7.4. The curves in green, blue, and red correspond to $A_c = 0.5$, 1.0, and 2.0, respectively. The 1D plot in the middle panel reveals that reducing the core anisotropy raises the core portion of the distribution while leaving the tails mostly unchanged. Additionally, we display the resonant velocities of the most unstable wave configuration for the three unstable cases shown. These velocities

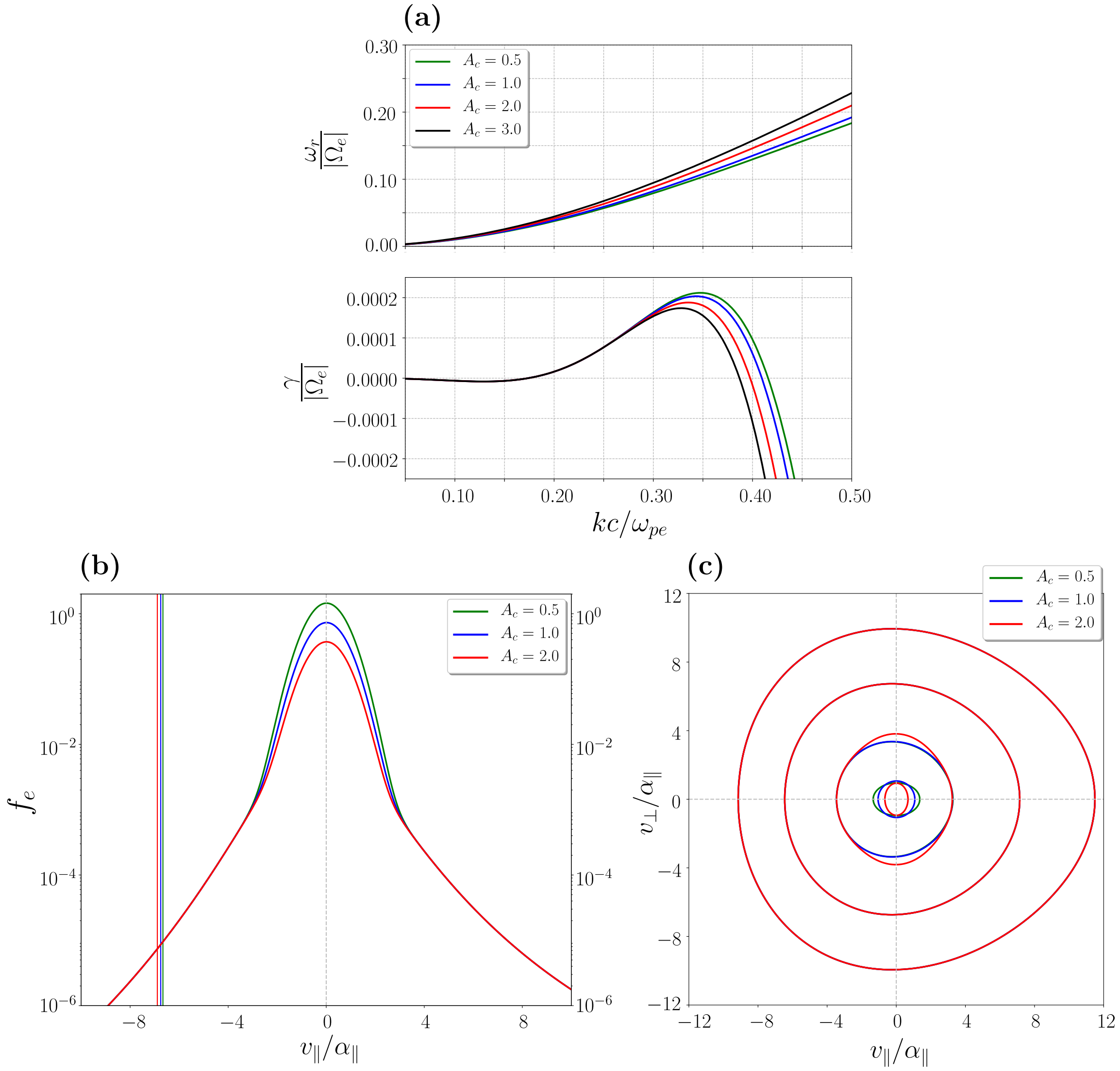

Figure 7.4: (a) Dispersion relation of the whistler mode (b) Parallel cuts at $v_\perp = 0$ of the CS distribution function. (c) Contours of the eVDF. In all panels we use $\eta_s = 0.1$, $\beta_{\parallel s} = 0.1$, $\delta = 0.2$, $A_s = 1.0$, and varying core anisotropy A_c. Different colors represent distinct A_c values: $A_c = 0.5$ (green), 1.0 (blue), 2.0 (red), and 3.0 (black).

predominantly reside in the strahlo part of the distribution and exhibit minimal variation as A_c increases. For $A_c = 2.0$, the maximum growth rate, the corresponding wavenumber, and the real part of the frequency are $\gamma_{\max}/|\Omega_e| = 1.8 \times 10^{-4}$, $kc/\omega_{pe} = 0.33$, and $\omega_r/|\Omega_e| = 0.11$, respectively. This results in a resonant velocity of $v_{\text{res}} = -6.89\alpha_\parallel$ and a resonant term of $\xi = -2.67$. Furthermore, examining the 2D plot of the CS distributions presented in the right panel, we confirm the anticipated behavior: alterations in A_c mainly affect the innermost contours associated with the core subpopulation, while the outer contours remain largely unaffected. This aligns with the limited impact of A_c on the WHFI.

7.4 Comparison with core-strahl model

It is important to highlight that the observed trend regarding the impact of A_c on the WHFI (Figure 7.4), as obtained in the previous section using the skew-Kappa CS model, contrasts directly with the findings reported in Shaaban et al. [107], as illustrated in their Figure 2. In their study, the authors utilized a core-strahl model for the electron population, with each component described by a drifting bi-Maxwellian distribution. Now, we will explore deeper into this inconsistency, providing further insights into the underlying electron distributions at play.

Figure 7.5 illustrates how changes in core anisotropy influence both the growth rates of the whistler mode and the electron distribution initially susceptible to the WHFI. This figure replicates, to the best of our ability, the growth rates shown in Figure 2 of Shaaban et al. [107]. We used the same core-strahl model and closely matched parameters to the ones used by the authors. Following the methodology of the previous sections, we additionally included plots of the underlying electron distributions. Specifically, to obtain these plots, we describe the electron distribution using a drifting bi-Maxwellian, as per Eq. (4.10), to represent both the core subpopulation ($j = c$) and the strahl beaming component ($j = b$), ensuring that the electrons follow a current-free core-strahl model. In this representation, the skewness of the eVDF is exclusively provided by the relative drift velocity between the core

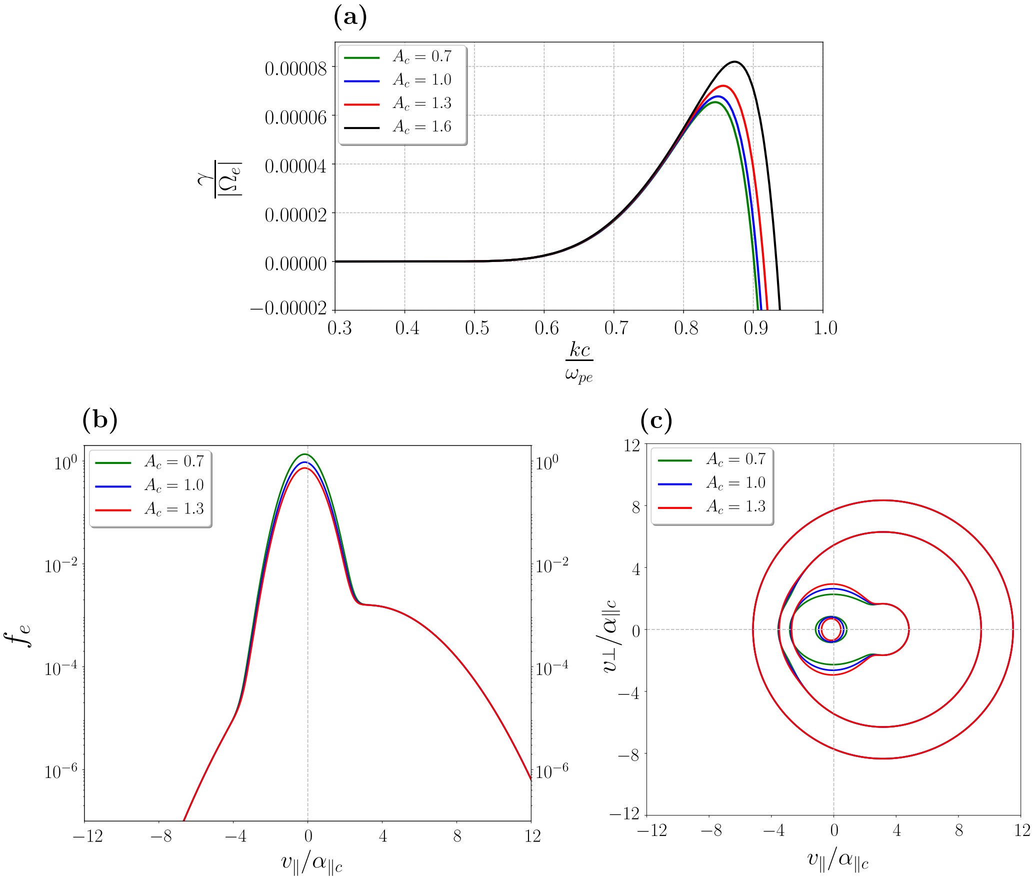

Figure 7.5: (a) Growth rates of the whistler mode (b) Parallel cuts at $v_\perp = 0$ of the core-strahl electron distribution function. (c) Contours of the eVDF. In all panels we use $\eta_b = 0.05$, $\beta_{\parallel b} = 0.02$, $w_b = 1.0$, $A_b = 1.0$, and varying core anisotropy A_c. Different colors represent distinct A_c values: $A_c = 0.7$ (green), 1.0 (blue), 1.3 (red), and 1.6 (black).

and beam. We also used a Maxwellian distribution with $\beta_{\parallel p} = 0.04$ to characterize the proton population. We fixed all other relevant parameters, including the density of the beaming population $n_b/n_e = 0.05$, the beam-to-core temperature ratio $T_{\parallel b}/T_{\parallel c} = 10.0$, $\beta_{\parallel b} = 0.02$, and the beam anisotropy $A_b = 1.0$ so that anisotropy is only provided by the core. Lastly, we fixed the normalized beam drift velocity at $w_b = U_b/\alpha_{\parallel b} = 1.0$, where $\alpha_{\parallel b}$ is the thermal velocity of the beaming subpopulation.

Panel 7.5(a) displays the imaginary part of the whistler mode frequency, normalized to the electron gyrofrequency $|\Omega_e|$, as a function of the normalized wavenumber for different values of $A_c = \left(\frac{\alpha_{\perp c}}{\alpha_{\parallel c}}\right)^2$. We can clearly observe the opposite behavior as the one reported in Figure 7.4. In this plasma configuration, cases with $A_c > 1$ enhance the growth rates, while those with $A_c < 1$ diminish the instability. Furthermore, panels 7.5(b) and 7.5(c) display, respectively, parallel cuts at $v_\perp = 0$ and contour plots of the eVDFs that trigger the mode excitation, producing the growth rates shown in the upper panel. Both plots clearly reveal an electron configuration that cannot be replicated by the CS model. Therefore, it is not surprising to observe some qualitative discrepancies between the models. The selected value for the drift of the beaming population results in the electron distribution presenting two distinct peaks, representing another suprathermal feature at play in the system, in addition to the skewness and anisotropy. Moreover, another notable difference that might contribute to these discrepancies is the absence of energetic tails in the core-strahl description, a feature well-captured by the CS model.

To further investigate this behavior, Figure 7.6 provides analogous information to that in Figure 7.6, but this time for a lower value of the normalized drift velocity, $w_b = 0.7$, while keeping all other parameters fixed at their previous values. In panel 7.6(a), we illustrate the normalized growth rates for various values of A_c, and panel 7.6(b) displays parallel cuts at $v_\perp = 0$ of the eVDFs providing the free energy for wave excitation. Interestingly, a recovery of the behavior shown in Figure 7.4(a) is observed when utilizing the core-strahl description. In this plasma configuration, cases with $A_c < 1$ enhance the growth rates of the whistler mode, while cases with $A_c > 1$ diminish the instability. The chosen drift in this case is such that the peak due to the beam is not visible in the electron distribution. However, it could be argued that it is still high enough that this electron configuration could not be reproduced using the CS model. Nevertheless, from this figure, we can conclude that for low values of the drift, we find qualitative agreement between both models.

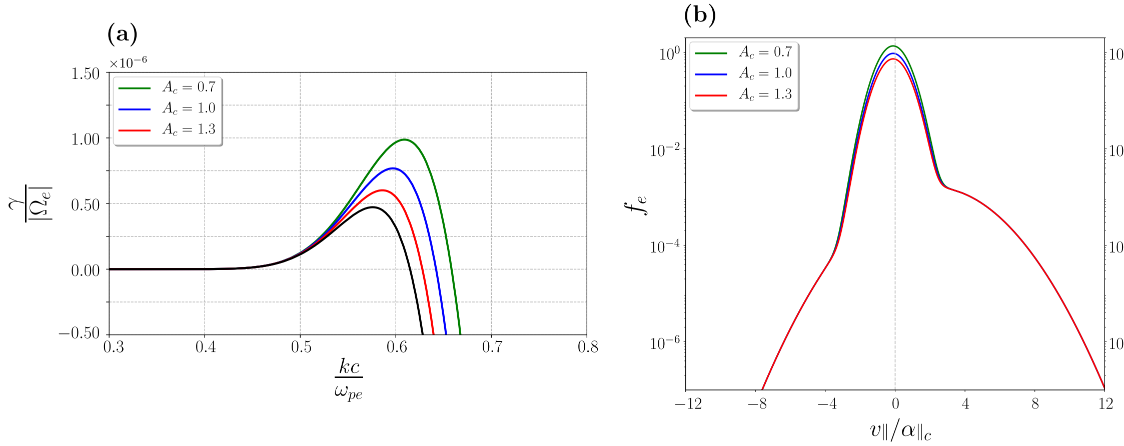

Figure 7.6: (a) Growth rates of the whistler mode (b) Parallel cuts at $v_\perp = 0$ of the core-strahl electron distribution function. In both panels we use $\eta_b = 0.05$, $\beta_{\|b} = 0.02$, $w_b = 0.7$, $A_b = 1.0$, and varying core anisotropy A_c. Different colors represent distinct A_c values: $A_c = 0.7$ (green), 1.0 (blue), 1.3 (red), and 1.6 (black).

It is worth noting that in this description with drifting bi-Maxwellians for the core and beam, these low values of drift are only capable of triggering the WHFI for sufficiently large $\beta_{\|b}$ values. This is demonstrated in Figure 7.7, where we depict the normalized growth rates for different drift values. The parameters used for this plot are consistent with those employed throughout this chapter: the density of the beaming population fixed at 10% ($n_b/n_e = 0.1$), $T_{\|b}/T_{\|c} = 7.0$, $\beta_{\|b} = 0.1$, $\beta_{\|p} = 0.01$, and $A_b = 1.0$. Additionally, we maintained an isotropic core with $A_c = 1.0$. The plot clearly indicates that the whistler mode does not become unstable for all drift values satisfying $U_h > 0$. Instead, there exists a threshold that must be exceeded to excite the WHFI. In this particular case, the threshold appears to be around $U_b \approx 3.3\ \alpha_{\|b}$, such that below this value, $\gamma < 0$ for all wave numbers. Furthermore, the threshold value for w_b is highly dependent on β. For instance, when considering β values used consistently in this chapter for the suprathermal population, $\beta_{\|b} = 0.02,\ 0.05,\ 0.1$, the respective threshold values are $U_b/\alpha_{\|b} = 0.66,\ 0.55,\ 0.33$. Hence, in Figure 7.6, where we closely approach the threshold drift value, the growth rates are notably low. In contrast, in the CS description, the WHFI is triggered for all $\delta > 0$, even with low beta values. This suggests that for the WHFI, the enhanced high-energy tails present in the CS description are a crucial feature to consider. Therefore, they should be included for a realistic assessment of the WHFI in the solar wind. A comparison with a core-halo type of model employing a drifting Kappa function to replicate the energetic tails is a necessary step to confirm this hypothesis.

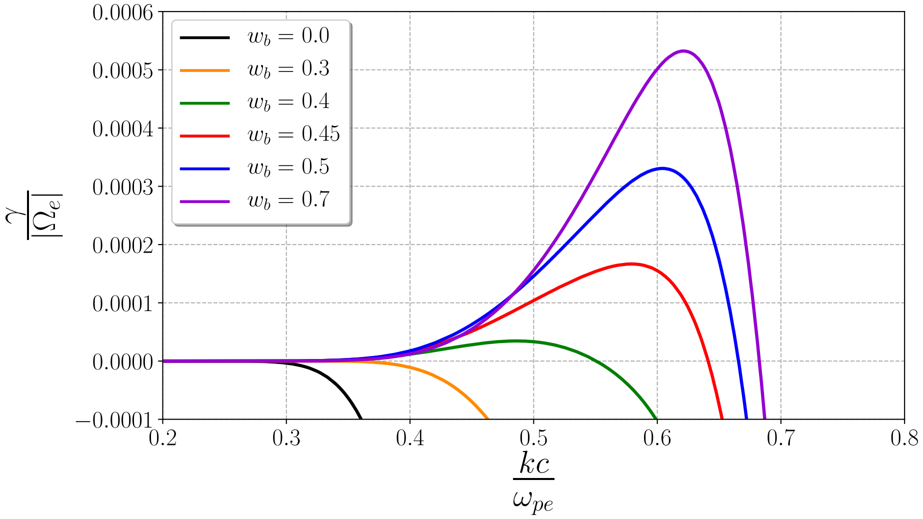

Figure 7.7: Growth rates of the whistler mode obtained using the core-strahl electron distribution function and fixing $\eta_b = 0.1$, $\beta_{\parallel b} = 0.1$, $A_b = 1.0$, and $A_c = 1.0$. Different colors represent distinct w_b values.

Furthermore, for $\beta_{\parallel b} = 0.1$, we also observe a dual behavior concerning the impact of core anisotropy, depending on the drift of the beam population. This behavior is illustrated in Figure 7.8, where we depict the normalized growth rates of the whistler mode for two different drift values: $w_b = 0.4$ (solid lines) and $w_b = 0.7$ (dashed lines), considering various core anisotropies ($A_c = 0.7$ in green, $A_c = 1.0$ in red, and $A_c = 1.6$ in blue). For the lower drift value, the observed behavior aligns with the CS description, where cases with $A_c < 1$ enhance the growth rates, while those with $A_c > 1$ diminish them. However, for the higher drift value, we observe the opposite effect. It is noteworthy that the transition point between these behaviors, in terms of w_b, seems to be highly dependent on $\beta_{\parallel b}$. Moreover, at $w_b = 0.7$, the range of wavenumbers where γ is positive is significantly wider compared to the WHFI ranges in the CS model, almost reaching wavenumbers typical of the core-driven WCI (see Figure 7.3 for comparison). This overlap does not occur when the CS description is used for the electrons in cases of small skewness, and it may be another crucial factor to consider in understanding the disparities between both models.

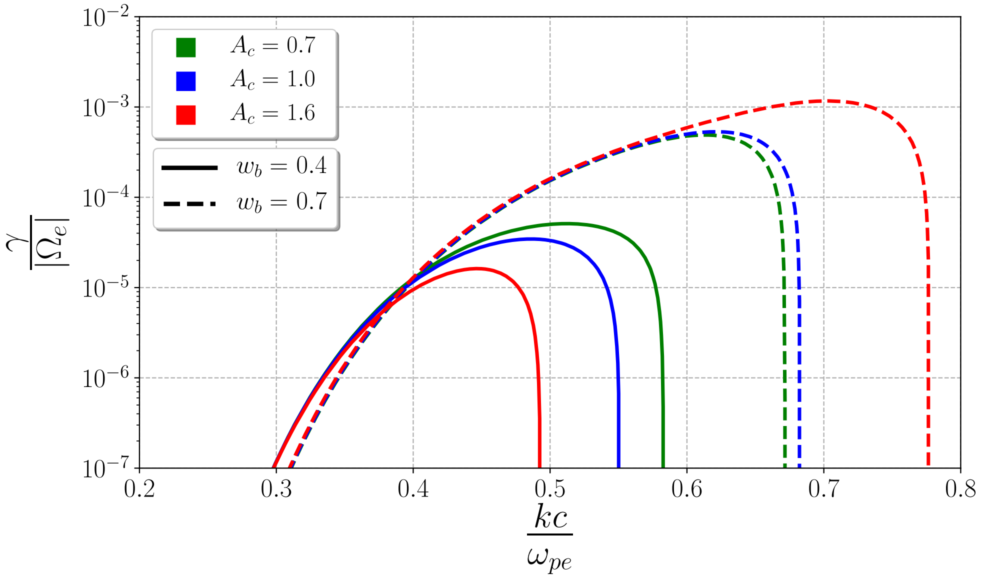

Figure 7.8: Growth rates of the whistler mode obtained using the core-strahl electron distribution function and fixing $\eta_b = 0.1$, $\beta_{\parallel b} = 0.1$ and $A_b = 1.0$. Different colors represent distinct A_c values: $A_c = 0.7$ (green), 1.0 (blue) and 1.6 (red). Different line styles represent distinct w_b values: $w_b = 0.4$ (solid line) and $w_b = 0.7$ (dashed line)

Understanding the underlying reasons for this dual effect of core anisotropy in terms of the suprathermal features of electron distributions and also the parameters governing the transition within the core-strahl description is an intriguing pursuit. However, it goes beyond the scope of this work. A more comprehensive comparison between various models is also necessary to assess the role of energetic tails in this process, given their ubiquitous presence in electron distribution measurements in the solar wind. Hence, evaluating how significant these energetic tails are in the interplay between skewness and anisotropy as sources of free energy is crucial for selecting models that effectively capture the relevant aspects of the system in theoretical investigations. Additionally, investigating the prevalence of plasma configurations where skewness is provided by a pronounced beam, as illustrated in Figure 7.5, could help in the judicious application of theoretical models to realistic solar wind scenarios. This would ensure that the conclusions drawn from this study are not only robust but also relevant to the actual solar wind system.

In conclusion, we want to emphasize that for low values of the drift of the beaming component, we observe qualitative agreement between the core-strahl description using drifting bi-Maxwellians and the skew-Kappa CS model. This finding adds evidence to the applicability of the CS model as a useful description of the solar wind electron population in cases of small skewness.

7.5 Discussion

Following the methodology from the previous chapter, we investigated the interplay between anisotropy and skewness as sources of free energy, analyzing their combined impact on exciting the parallel-propagating whistler mode. To achieve this, we employed the CS model for the electron population, assuming a small electron skewness ($\delta^3 \ll 1$), and considered typical solar wind conditions for the remaining relevant plasma parameters. In this chapter, anisotropy was attributed specifically to the core population. We isolated the effect of the core by analyzing dispersion relations using a fixed value for the intrinsic anisotropy of the suprathermal population, set at $A_s = A_b = 1.0$. This approach ensured that the excitation of the whistler mode was driven solely by the interplay between δ and A_c. As in the previous chapter, we presented the total electron distribution for representative cases of unstable configurations, illustrating how the distribution shape changes with variations in δ and A_c. This visual representation of the suprathermal features operating in the system facilitated the understanding of how different suprathermal features influence the excitation of the whistler mode. This aspect was particularly relevant when comparing the CS and core-strahl drifting bi-Maxwellians models, enabling us to elucidate the apparent behavioral discrepancies observed when utilizing each model to describe the solar wind electron distribution.

Our investigation has revealed that the WCI triggered by the core population manifests as positive growth rates at larger wavenumbers when compared with strahlo-driven instabilities (induced by the anisotropy or skewness of the strahlo). This distinction provides valuable insights to identify the subpopulation that contributes free energy to the system. Furthermore, the real part of the frequency, ω_r, for the strahlo-driven instabilities consistently displays lower values than those generated by the core-driven WCI. This difference could serve as an additional means to distinguish the energy source in observational data. Interestingly, we observed that significantly higher values of A_c are necessary to excite the whistler mode in comparison to A_s. The transition from consistently stable to unstable wave modes occurs at approximately $A_c \approx 2.2$ when the energy is provided by the core. Conversely, when the energy is sourced from the strahlo, all cases with $A_s > 1$ exhibit instability. Beyond this point, similar values of anisotropy yield comparable growth rates for both cases. For instance, in a plasma system with an anisotropic strahlo (core) where $A_s = 2.5$ ($A_c = 2.5$), the maximum growth rate is $\gamma/|\Omega_e| = 1.92 \times 10^{-2}$ ($\gamma/|\Omega_e| = 1.56 \times 10^{-2}$).

Furthermore, the investigation into the combined influence of core anisotropy and skewness on the linear stability of the whistler mode within the CS model context revealed that the strahlo skewness (controlled by δ) does not significantly impact the core-driven WCI. Increasing this parameter hardly affects both the unstable wavenumber range and the maximum growth rates achieved by the instability. Conversely, changes introduced by the core anisotropy, $A_c \neq 1$, on the growth rates of the WHFI are also minor. For instance, for a skewed distribution with $\delta = 0.2$, the maximum growth rate achieved increases by a factor of 1.08 when we halve the value of the core anisotropy from $A_c = 2.0$ to $A_c = 1.0$. These findings suggest that we can reasonably neglect the contribution of core anisotropy when evaluating the significance of different instabilities driven by the suprathermal population and, conversely, we can ignore the skewness of the eVDF for studies focusing on the core-driven WCI.

The analysis and results presented in this chapter mark the culmination of our exploration into the interplay between anisotropy and skewness as sources of free energy in the excitation of the whistler mode within the context of the CS model.

Chapter 8

Conclusions

In this research, we conducted an extensive theoretical study using tools from kinetic theory to investigate the significance of suprathermal electron populations on the excitation of the parallel-propagating whistler mode in non-collisional and magnetized plasma. To achieve this, we introduced a novel heuristic model to characterize the solar wind electron system, named the *Core-Strahlo* (CS) model. We thoroughly investigated its properties and its applicability for describing the solar wind electrons. Furthermore, using this model, we performed a stability analysis of the whistler mode, initially considering isotropic electron subpopulations where the free energy for wave excitation was attributed solely to skewness. Subsequently, to gain a more precise and realistic understanding of mode stability, we explored anisotropic configurations, aiming to understand the interplay between skewness and anisotropy as sources of free energy within the system.

The first part of this thesis focused on introducing the CS model and conducting a comprehensive analysis of its properties. The CS model employs a superposition of two subpopulations to characterize the solar wind electron distribution: a quasithermal core described by a bi-Maxwellian function and a suprathermal *strahlo*, representing the halo and strahl electrons, described by a single skew-Kappa distribution function. We conducted a detailed examination of the properties of the skew-Kappa distribution in velocity space, focusing on the mathematical and technical details. This analysis allowed us to establish the validity range for the CS model. As a theoretical tool, the CS description is limited to situations where skewness is small ($\delta^3 \ll 1$), ensuring a suitable representation of the solar wind electrons. It is worth noting that the adoption of the skew-Kappa function was motivated by observations. Within this validity range, it accurately reproduces the primary suprathermal kinetic characteristic observed in solar wind velocity distributions: the high-energy tails (quantified by the κ parameter) associated with the halo and the skewness (quantified by the skewness parameter δ) associated with the strahl subpopulation. The use of the skew-Kappa function allows the distribution skewness to be controlled through just one parameter and significantly reduces the space of free parameters to analyze. We proposed the CS model with the intention of simplifying the description of the electrons and the subsequent kinetic studies of their dynamics. While it has not yet been observationally tested, we believe the model possesses interesting properties that warrant further exploration and we are actively working to provide observational validation for this description.

To the best of our knowledge, the skew-Kappa function has not previously been employed in the context of space plasmas. In the original derivation of this distribution for turbulent flows, Beck [111] demonstrated that the inverse of the asymmetry term, $1/\delta$, is proportional to the square root of the Reynolds number ($Re^{1/2}$). Additionally, a straightforward calculation reveals that Re is inversely proportional to the Knudsen number K_n ($Re \propto K_n^{-1}$). Given that K_n is directly related to heat flux transport in collisional plasmas [33, 70, 76], the connection between δ and K_n suggest that δ could potentially be related with parameters pertinent to turbulence and plasma collisionality. This establishes a potential link between the kinetic properties of the plasma (skewness) and a fluid description of the medium (the Knudsen number). Therefore, the CS model, based on the skew-Kappa distribution, could be more than an *ad-hoc* representation of solar wind electrons. While a comprehensive explanation of this relation is beyond the scope of this work, we firmly believe that further theoretical studies linking these parameters in plasma systems should be pursued.

In the second part of this work, we focused on utilizing the CS model to describe the solar wind electron population. We established a comprehensive framework to study the linear excitation of wave modes propagating parallel to the background magnetic field. Within this framework, we investigated the whistler heat flux instability (WHFI) and studied the impact of all relevant parameters for the isotropic case on its excitation and the marginal stability thresholds. Additionally, we presented threshold conditions for the instability that can be used for modeling and comparison with observational data. Our results demonstrated that in the isotropic setting, the excitation of the whistler mode is solely governed by δ, consistent with the WHFI, as this parameter controls the skewness of the eVDF. On the other hand, each of the remaining relevant parameters alter the stability of the mode, and the thresholds used for comparison with observations, in a distinct manner and with different strength. It has been well-documented that these parameters characterizing the suprathermal populations exhibit significant variations with radial distance from the Sun and solar wind speed [54, 86, 105]. Based on these observations, we believe dedicated efforts should be made to establish a comprehensive framework accounting for the trends and fluctuations of all relevant parameters in a consistent and systematic manner.

This is a crucial step for a realistic assessment of the relevance of the WHFI in the solar wind through comparisons between theoretical predictions and observational data. Such an understanding is especially pertinent for delineating its role in the non-collisional regulation of the electron heat flux.

In addition, we explored the impact of the macroscopic heat flux parameter on the excitation of the WHFI, as it is the parameter that has been conventionally used to analyze this instability. Our exploration revealed that plasma states with identical initial heat flux could exhibit varying stability to WHFI. In other words, systems with high $q_{\|e}/q_0$ values can be stable enough, so that the WHFI may not be able to effectively modify electron heat flux values through wave-particle interactions. Consequently, the heat flux alone may not be the most precise indicator of the WHFI. The precise source of heat flux instabilities is the distribution skewness. In the case of the CS model, this suprathermal feature is clearly represented by the skewness parameter δ. Thus, high δ values, rather than high q_e values, align with more unstable states when utilizing a more realistic representation of solar wind electrons. We expect these findings to encourage novel approaches centered on distribution skewness (a kinetic property of the eVDF) rather than just the heat flux parameter (a fluid quantity of the plasma), especially for studying the role of the WHFI in depleting field-aligned electron heat flux values below the levels predicted by the collisional transport model, as distinctly observed by Bale et al. [70]. Furthermore, we hope our results motivate efforts to develop new methods for measuring or estimating the skewness or asymmetry of the eVDF from observations.

In the last part of this work, we focused on extending the usage of the CS model to comprehensively study the excitation of the parallel propagating whistler mode, triggered by electron populations presenting skewness and anisotropy as sources of free energy. To effectively study the interplay between these suprathermal features, we isolated the effect of each subpopulation. First, we considered a skewed electron distribution with an anisotropic strahlo and studied the stability of the mode and its sensitivity to the parameters governing these characteristics. Our results showed that strahlo anisotropy is a more effective and potent source of free energy compared to field-aligned skewness, inducing much more explosive instabilities. Thus, the linear analysis suggests that anisotropy of the suprathermal population is a more critical parameter to focus on when investigating wave-particle interaction processes and the non-collisional relaxation of the electron population to quasi-stable states in the solar wind. Nonetheless, the energy exchange between particles and electromagnetic fields is a complex and highly non-linear process. Some studies have shown that more explosive instabilities (with higher growth rates) may saturate rapidly, limiting the necessary time for an effective energy exchange. On the other hand, instabilities producing smaller linear growth rates may be sustained for longer periods, exerting stronger effects over time [83]. Therefore, a quasilinear and/or non-linear approach is crucial for a comprehensive understanding of the interplay between anisotropy and skewness and the relative role the respective instabilities have on the solar wind electron dynamics.

We later repeated the linear stability analysis, considering an isotropic but skewed strahlo and an anisotropic core. We studied the changes in the dispersive properties introduced by the interplay between these suprathermal features. Our results demonstrated that we can safely disregard the core suprathermality when evaluating the significance of the WHFI in the solar wind electron dynamics. This conclusion enables us to reduce the parameter space under consideration, a particularly relevant simplification when focusing on the electron heat flux regulation problem and the relevance of WHFI in this process. Nonetheless, it is worth noting that we have restricted the analysis to electron configurations with only one anisotropic subpopulation at a time. However, this restriction does not apply to solar wind electrons. In this system, anisotropy can be present in both the core and suprathermal subpopulations. It is likely that both of these sources of anisotropy are relevant and contribute simultaneously to electron dynamics. Therefore, a more in-depth analysis, allowing both subpopulations to simultaneously exhibit anisotropy and go beyond linear theory, is necessary to fully understand the interplay between these two suprathermal characteristics and assess their importance in the kinetic processes of the solar wind. Accordingly, we intend to employ electromagnetic *Particle-In-Cell* simulations to rigorously test and further enhance the analysis presented here, encompassing a broader range of realistic solar wind scenarios.

It is worth noting that a skewed and anisotropic distribution can also be unstable to other micro-instabilities beyond the WHFI and the whistler-cyclotron instability (WCI). Recent work by López et al. [66, 162] has shown that electron distribution functions composed of an isotropic core and a beam can be unstable to several of these micro-instabilities, including the electrostatic instability. The electrostatic mode is the fastest-growing only when the relative drift between the core and beam exceeds the thermal speed. Furthermore, even when the electrostatic mode is faster than the electromagnetic instability, its saturation level is also faster but lower than that of the electromagnetic mode. Therefore, the electromagnetic mode dominates in the nonlinear regime. In our study, by design, the relative drift between the core and strahlo is smaller than the thermal speed. Hence, the electrostatic instability may be present, but the WHFI triggered by skewness should dominate. For this reason and because of the particular interest of the community in the potential role of the WHFI in regulating solar wind heat flux through wave-particle interactions, we choose to focus solely on the WHFI and its interplay with the WCI. However, we acknowledge the possible existence of additional instabilities due to the various nonthermal properties of the electron distribution. We believe it is important to address the coexistence and interaction of these instabilities, and we plan to conduct such an analysis in the near future.

To finalize, the results presented herein align with prior research and more established models of solar wind electrons, providing theoretical validation for the CS model. This representation is capable of reproducing the main kinetic characteristics of solar wind electron distributions by employing a unified description for the suprathermal halo and strahl subpopulations. Consequently, we establish this model as a robust and suitable representation of the solar wind eVDF. Moreover, the CS model offers an alternative to the typical functions used to phenomenologically model the eVDF, utilizing fewer free parameters than conventional core-halo-strahl representations. This may allow us to more easily study the interaction between the suprathermal subpopulations in intermediate states where the halo is forming at the expense of the strahl. Further, this description greatly simplifies the study of the WHFI and its application may lead to the development of simpler theoretical studies, focusing on the distribution skewness and the impact electron configurations with a less pronounced strahl have on non-collisional processes influencing solar wind dynamics. Specifically, it could shed light on the role the WHFI plays in the transport of electron thermal energy in the solar wind.

We anticipate that our theoretical analysis, inspired by observations, will offer valuable insights into the ongoing debate regarding the regulation of solar wind electron heat flux. Conducting systematic theoretical studies that consider realistic solar wind conditions and comparing with experimental data the results obtained using different kinetic models of the solar wind are crucial for a comprehensive understanding of heat flux transport through the heliosphere. It would also be valuable to further extend the analyses here conducted considering the influence of obliquely propagating whistler modes on the electron distribution shape, as well as examining their interaction with other known instabilities in the solar wind, such as the firehose instability. Furthermore, we hope this study will encourage the development of theoretical works exploring the dynamics of the halo and strahl using a unified description. This approach could prove especially helpful in comprehending the intricate dynamics of interaction between these suprathermal populations as the solar wind expands from the outer solar corona into the heliosphere. Ultimately, we expect our results to find validation through electron measurements obtained from current and upcoming solar wind missions, which is especially relevant in light of the new Parker Solar Probe and Solar Orbiter missions.

Appendix A

Macroscopic parameters

In this appendix, we provide the expressions for the key macroscopic parameters of a population of particles with mass m_s, described by a skew-Kappa distribution function, denoted as f_s and defined in Eq. (3.3). To perform the integrals in velocity space involved in these expressions, we make the assumption of small skewness ($\delta^3 \ll 1$). We calculate these macroscopic parameters by employing a second-order Taylor expansion of Eq. (3.3) with respect to δ. As customary, the subscripts $\|$ and $\perp$ refer to directions relative to the background magnetic field in the following equations.

1. **Taylor expansion of f_s**

$$f_s(v_\perp, v_\|) = n_s C_s \left[F_0(v_\perp, v_\|) - \delta F_1(v_\perp, v_\|) + \frac{\delta^2}{2} F_2(v_\perp, v_\|) + \mathcal{O}(\delta^3) \right] , \quad \text{(A.1)}$$

where

$$F_0(v_\perp, v_\|) = \left[1 + \frac{1}{\kappa - \frac{3}{2}} \left(\frac{v_\perp^2}{\theta_\perp^2} + \frac{v_\|^2}{\theta_\|^2} \right) \right]^{-(\kappa+1)} ,$$

$$F_1(v_\perp, v_\parallel) = \left[\frac{\kappa+1}{\kappa-\frac{3}{2}}\right]\left[\frac{v_\parallel}{\theta_\parallel} - \frac{v_\parallel^3}{3\theta_\parallel^3}\right]\left[1+\frac{1}{\kappa-\frac{3}{2}}\left(\frac{v_\perp^2}{\theta_\perp^2}+\frac{v_\parallel^2}{\theta_\parallel^2}\right)\right]^{-(\kappa+2)} ,$$

and

$$F_2(v_\perp, v_\parallel) = \left[\frac{\kappa+1}{\kappa-\frac{3}{2}}\right]\left[\frac{\kappa+2}{\kappa-\frac{3}{2}}\right]\left[\frac{v_\parallel}{\theta_\parallel} - \frac{v_\parallel^3}{3\theta_\parallel^3}\right]^2\left[1+\frac{1}{\kappa-\frac{3}{2}}\left(\frac{v_\perp^2}{\theta_\perp^2}+\frac{v_\parallel^2}{\theta_\parallel^2}\right)\right]^{-(\kappa+3)} .$$

2. **Number density**

$$n_s = \int f_s \; d\mathbf{v} = n_s C_s \; \frac{[(\kappa-3/2)\pi]^{\frac{3}{2}}\,\theta_\perp^2\theta_\parallel\Gamma(\kappa-1/2)}{\Gamma(\kappa+1)}\left[1+\frac{\delta^2}{4}\Psi_1(\kappa)\right] , \quad \text{(A.2)}$$

where we have defined

$$\Psi_1(\kappa) = \left(\frac{2\kappa-1}{2\kappa-3}\right) - \frac{7}{12} .$$

Hence, within the small skewness regime, the normalization constant C_s, expressed in terms of the number density, is calculated as follows:

$$C_s = \frac{\Gamma(\kappa+1)}{[(\kappa-3/2)\pi]^{3/2}\,\theta_\perp^2\theta_\parallel\Gamma(\kappa-1/2)}\left[1-\frac{\delta^2}{4}\Psi_1(\kappa)\right] . \quad \text{(A.3)}$$

3. **Parallel bulk velocity**

$$U_s = \frac{1}{n_s}\int v_\parallel f_s \; d\mathbf{v} = -\frac{\delta}{4}\theta_\parallel . \quad \text{(A.4)}$$

4. **Perpendicular temperature**

$$T_{\perp s} = \frac{m_s}{2n_s k_B}\int v_\perp^2 f_s \; d\mathbf{v} = \frac{m_s\,\theta_\perp^2}{2k_B}\left[1+\frac{\delta^2}{4}\Psi_2(\kappa)\right] , \quad \text{(A.5)}$$

where we have defined

$$\Psi_2(\kappa) = \frac{5}{12}\left(\frac{2\kappa-3}{2\kappa-5}\right) - \left(\frac{2\kappa-1}{2\kappa-3}\right) + \frac{7}{12}\,.$$

5. **Parallel temperature**

$$T_{\parallel s} = \frac{m_s}{n_s k_B}\int (v_\parallel - U_s)^2 f_s \; d\mathbf{v} = \frac{m_s\;\theta_\parallel^2}{2k_B}\left[1 + \frac{\delta^2}{4}\Psi_3(\kappa)\right]\,, \tag{A.6}$$

where we have defined

$$\Psi_3(\kappa) = \frac{35}{12}\left(\frac{2\kappa-3}{2\kappa-5}\right) - \left(\frac{2\kappa-1}{2\kappa-3}\right) - \frac{23}{12}\,.$$

6. **Parallel heat flux**

$$q_{\parallel s} = \frac{1}{2}m_s\int (\vec{v}-\vec{U}_s)^2(v_\parallel - U_s) f_s \; d\mathbf{v} = \frac{m_s\;n_s\;\theta_\parallel^3}{8}\;\delta\left[A_s\Psi_4(\kappa) + \Psi_5(\kappa)\right]\,, \tag{A.7}$$

where

$$\Psi_4(\kappa) = \left(\frac{2\kappa-3}{2\kappa-5}\right) - 1\,, \quad \Psi_5(\kappa) = \frac{5}{2}\left(\frac{2\kappa-3}{2\kappa-5}\right) - \frac{3}{2}\,, \quad A_s = \left(\frac{\theta_\perp}{\theta_\parallel}\right)^2\,.$$

As a result, the parallel heat flux for the complete electron distribution in the Core-Strahlo model, as defined by Eq. (3.1), can be expressed as:

$$q_{\parallel e} = \frac{m_e\;n_s\;\theta_\parallel^3}{4}\;\delta\left[A_s\Psi_6(\kappa) + \Psi_7(\kappa) + \frac{1}{4}\left(\frac{\alpha_\parallel}{\theta_\parallel}\right)^2(3 + 2A_c)\right]\,, \tag{A.8}$$

where

$$\Psi_6(\kappa) = \frac{1}{2}\left(\frac{2\kappa-3}{2\kappa-5}\right) - 1\,, \quad \Psi_7(\kappa) = \frac{5}{4}\left(\frac{2\kappa-3}{2\kappa-5}\right) - \frac{3}{2}\,, \quad A_c = \left(\frac{\alpha_\perp}{\alpha_\parallel}\right)^2\,.$$

Appendix B

Dispersion tensor

In a non-collisional and uniform plasma, which is immersed in a background magnetic field $\mathbf{B_0} = B_0\hat{z}$, the dispersion tensor $\mathcal{D}$ takes the following form when considering parallel-propagating waves with wavevector $\mathbf{k} = k\hat{z}$:

$$\mathcal{D}(\omega, k, f_j) = \begin{pmatrix} 1 - \frac{kc^2}{\omega^2} + 4\pi \sum_j \chi_1(f_j) & 4\pi \sum_j \chi_2(f_j) & 0 \\ -4\pi \sum_j \chi_2(f_j) & 1 - \frac{kc^2}{\omega^2} + 4\pi \sum_j \chi_1(f_j) & 0 \\ 0 & 0 & 1 + 4\pi \sum_j \chi_3(f_j) \end{pmatrix}. \tag{B.1}$$

The restriction $|\mathcal{D}(\omega, k, f_j)|$ determines the relationship between the wave frequency $\omega = \omega_r + i\gamma$ and the wavenumber k for parallel-propagating modes. In Equation (B.1), the elements of the dispersion tensor are expressed in terms of susceptibilities $\chi_i(f_j)$, with the summation carried out over all species j comprising the plasma. The functional form of $\chi_i(f_j)$ depends on the initial distribution function f_j that describes population j and is obtained by solving the following integrals:

$$\chi_1(f_j) = \frac{\omega_{pj}^2}{\omega^2}\frac{1}{8n_j}\sum_{n=-1,1}\int\int \frac{v_\perp^2 \psi_{jn}}{\omega - kv_\parallel - n\Omega_j} dv_\perp dv_\parallel - \frac{\omega_{pj}^2}{\omega^2}\frac{1}{4\pi}\,, \tag{B.2}$$

$$\chi_2(f_j) = \frac{\omega_{pj}^2}{\omega^2}\frac{i}{8n_j}\sum_{n=-1,1}\int\int \frac{n v_\perp^2 \psi_{jn}}{\omega - kv_\parallel - n\Omega_j} dv_\perp dv_\parallel\,, \tag{B.3}$$

and

$$\chi_3(f_j) = \frac{\omega_{pj}^2}{2n_j k}\int\int \frac{v_\perp}{\omega - kv_\parallel}\,\frac{\partial f_j}{\partial v_\parallel} dv_\perp dv_\parallel\,, \tag{B.4}$$

where we have defined:

$$\psi_{jn} = n\Omega_j \frac{\partial f_j}{\partial v_\perp} + kv_\perp \frac{\partial f_j}{\partial v_\parallel}\,.$$

By considering the Taylor approximation of the skew-Kappa function f_s as shown in Equation (A.1), we find that all resonant integrals necessary for constructing the dispersion tensor are reduced to those required for calculating the dispersion relation in a Kappa-distributed plasma, as previously investigated by Summers and Thorne [151], Mace and Hellberg [149], and Hellberg and Mace [150]. Consequently, under the small skewness approximation, we can safely assume that all poles and branch cuts have been accounted for, and these integrals do not present any other contribution. Thus, to second order in δ, the susceptibilities χ_i of the strahlo population take the following form:

$$\chi_1(f_s) = -\frac{\omega_{ps}^2}{4\pi\omega^2} + \frac{1}{8\pi}\frac{\omega_{ps}^2}{\omega^2}\left(\frac{\theta_\perp}{\theta_\parallel}\right)^2 \sum_{n=-1,1}\left(\Lambda_{\kappa n}^0 + \delta\Lambda_{\kappa n}^1 + \frac{\delta^2}{2}\Lambda_{\kappa n}^2\right)\,, \tag{B.5}$$

$$\chi_2(f_s) = \frac{i}{8\pi}\frac{\omega_{ps}^2}{\omega^2}\left(\frac{\theta_\perp}{\theta_\parallel}\right)^2 \sum_{n=-1,1} n\left(\Lambda_{\kappa n}^0 + \delta\Lambda_{\kappa n}^1 + \frac{\delta^2}{2}\Lambda_{\kappa n}^2\right)\,, \tag{B.6}$$

and

$$\chi_3(f_s) = \frac{1}{2\pi}\frac{\omega_{ps}^2}{k^2\ \theta_{\|}^2}\left(\frac{2\kappa-1}{2\kappa-3}\right)\left(\Lambda_{\kappa 0} + \delta\Lambda_{\kappa 1} + \frac{\delta^2}{2}\Lambda_{\kappa 2}\right)\ , \tag{B.7}$$

Here, the elements of the expansion are given by:

$$\Lambda_{\kappa n}^0 = 1 + \varphi_{n\kappa} Z_\kappa(\xi_{n\kappa})\,, \tag{B.8}$$

$$\begin{aligned} \Lambda_{\kappa n}^1 = \frac{1}{2}\sqrt{\frac{\kappa}{\kappa-\frac{3}{2}}}(1-\xi_n^2)Z_\kappa(\xi_{n\kappa}) + \frac{1}{2}\left(\frac{\varphi_n}{3} - \xi_n\right) \\ - \left(\frac{\kappa-\frac{1}{2}}{\kappa-\frac{3}{2}}\right)\left(1-\frac{\xi_n^2}{3}\right)\varphi_n[1+\bar{\xi}_{n\kappa}Z_{\kappa+1}(\bar{\xi}_{n\kappa})]\,, \end{aligned} \tag{B.9}$$

and

$$\begin{aligned} \Lambda_{\kappa n}^2 = \left(\frac{\kappa-\frac{1}{2}}{\kappa-\frac{3}{2}}\right)\left(\frac{\kappa+\frac{1}{2}}{\kappa-\frac{3}{2}}\right)\varphi_n\xi_n\left(1-\frac{\xi_n^2}{3}\right)^2[1+\tilde{\xi}_{n\kappa}Z_{\kappa+2}(\tilde{\xi}_{n\kappa})] \\ + \frac{1}{3}\left(\frac{\kappa-\frac{1}{2}}{\kappa-\frac{3}{2}}\right)\varphi_n\xi_n\left(\frac{\xi_n^2}{6}-1\right) - \frac{\xi_n}{6}\left(\xi_n - \frac{\varphi_n}{2}\right) \\ - \left(\frac{\kappa-\frac{1}{2}}{\kappa-\frac{3}{2}}\right)(1-\xi_n^2)\left(1-\frac{\xi_n^2}{3}\right)[1+\bar{\xi}_{n\kappa}Z_{\kappa+1}(\bar{\xi}_{n\kappa})] \\ + \frac{1}{2}\left(\frac{\kappa-\frac{1}{2}}{\kappa-\frac{3}{2}}\right) + \frac{1}{8} - \frac{\Psi_1(\kappa)}{2}[1+\varphi_{n\kappa}Z_\kappa(\xi_{n\kappa})] \end{aligned} \tag{B.10}$$

for $n = 1, -1$. In addition, $\Lambda_{\kappa 0}$, $\Lambda_{\kappa 1}$, and $\Lambda_{\kappa 2}$ are given by:

$$\Lambda_{\kappa 0} = 1 + \bar{\xi}_{0\kappa} Z_{\kappa+1}(\bar{\xi}_{0\kappa})\,, \tag{B.11}$$

$$
\begin{aligned}
\Lambda_{\kappa 1} =& \frac{1}{2}\sqrt{\frac{\kappa+1}{\kappa-\frac{3}{2}}}(1-\xi_0^2)Z_{\kappa+1}(\bar{\xi}_{0\kappa}) - \frac{\xi_0}{3} \\
&- \left(\frac{\kappa+\frac{1}{2}}{\kappa-\frac{3}{2}}\right)\left(1-\frac{\xi_0^2}{3}\right)\xi_0[1+\tilde{\xi}_{0\kappa}Z_{\kappa+2}(\tilde{\xi}_{0\kappa})]\,,
\end{aligned}
\tag{B.12}
$$

and

$$
\begin{aligned}
\Lambda_{\kappa 2} =& \left(\frac{\kappa+\frac{3}{2}}{\kappa-\frac{3}{2}}\right)\left(\frac{\kappa+\frac{1}{2}}{\kappa-\frac{3}{2}}\right)\xi_0^2\left(1-\frac{\xi_0^2}{3}\right)^2[1+\hat{\xi}_{0\kappa}Z_{\kappa+3}(\hat{\xi}_{0\kappa})] \\
&- \frac{1}{24}\left(\frac{\kappa-\frac{3}{2}}{\kappa-\frac{1}{2}}\right) + \frac{1}{2}\left(\frac{\kappa+\frac{1}{2}}{\kappa-\frac{3}{2}}\right)\left(1-\frac{\xi_0^2}{3}\right)^2 \\
&- \left(\frac{\kappa+\frac{1}{2}}{\kappa-\frac{3}{2}}\right)(1-\xi_0^2)\left(1-\frac{\xi_0^2}{3}\right)[1+\tilde{\xi}_{0\kappa}Z_{\kappa+2}(\tilde{\xi}_{0\kappa})] \\
&+ \frac{1}{6}\left(1-\frac{\xi_0^2}{2}\right) - \frac{\Psi_1(\kappa)}{2}[1+\bar{\xi}_{0\kappa}Z_{\kappa+1}(\bar{\xi}_{0\kappa})]\,.
\end{aligned}
\tag{B.13}
$$

Finally, the susceptibilities χ_i for the core population, which is described by a bi-Maxwellian distribution (3.2), are as follows:

$$
\chi_1(f_c) = -\frac{\omega_{pc}^2}{4\pi\omega^2} + \frac{1}{8\pi}\frac{\omega_{pc}^2}{\omega^2}\left(\frac{\alpha_\perp}{\alpha_\parallel}\right)^2 \sum_{n=-1,1}[1+\phi_n Z(\zeta_n)]\,, \tag{B.14}
$$

$$
\chi_2(f_c) = \frac{i}{8\pi}\frac{\omega_{pc}^2}{\omega^2}\left(\frac{\alpha_\perp}{\alpha_\parallel}\right)^2 \sum_{n=-1,1} n\,[1+\phi_n Z(\zeta_n)]\,, \tag{B.15}
$$

$$
\chi_3(f_c) = \frac{1}{2\pi}\frac{\omega_{pc}^2}{k^2\ \alpha_\parallel^2}\,[1+\zeta_0 Z(\zeta_0)]\,. \tag{B.16}
$$

In all of the expressions above, we used the notation $\omega_{pj}^2 = 4\pi n_j q_j^2/m_j$ to represent the square of the plasma frequency for population j, where n_j represents the density of population j, while q_j and m_j denote the charge and mass of the particles composing population j. Additionally, the plasma dispersion function, denoted as $Z(\zeta)$, is defined as follows:

$$Z_{(}\zeta) = \frac{1}{\sqrt{\pi}} \int_{-\infty}^{\infty} \frac{e^{-t^2}}{t-\zeta}\, dt\,. \tag{B.17}$$

Furthermore, Z_κ is the modified plasma dispersion function [90, 94, 147, 150]

$$Z_\kappa(\xi) = \frac{\Gamma(\kappa)}{\sqrt{\pi\kappa}\,\Gamma(\kappa-1/2)} \int_{-\infty}^{\infty} \frac{\left(1+\dfrac{t^2}{\kappa^2}\right)^{-\kappa}}{t-\xi}\, dt\,, \tag{B.18}$$

that, for any real value of κ such that $\kappa > 1/2$, can be expressed in terms of the Gauss Hypergeometric function ${}_2F_1$:

$$Z_\kappa(\xi) = i\frac{\kappa-1/2}{\kappa^{3/2}}\, {}_2F_1\left[1,\ 2\kappa;\, ,\kappa+1;\ \frac{1}{2}\left(1-\frac{\xi}{i\kappa^{1/2}}\right)\right]\,. \tag{B.19}$$

Finally, for $n = -1, 0, 1$ we have defined the following parameters:

$$\xi_n = \frac{\omega - n\Omega_e}{k\theta_\parallel}, \qquad \varphi_n = \xi_n + \frac{n\Omega_e u_\parallel}{k\theta_\perp^2}\,,$$

$$\zeta_n = \frac{\omega - n\Omega_e - kU_c}{k\alpha_\parallel}, \qquad \phi_n = \zeta_n + \frac{n\Omega_e \alpha_\parallel}{k\alpha_\perp^2}\,,$$

$$\xi_{n\kappa} = \xi_n\sqrt{\frac{\kappa}{\kappa-3/2}}, \quad \bar{\xi}_{n\kappa} = \xi_n\sqrt{\frac{\kappa+1}{\kappa-3/2}}, \quad \tilde{\xi}_{n\kappa} = \xi_n\sqrt{\frac{\kappa+2}{\kappa-3/2}}, \quad \hat{\xi}_{n\kappa} = \xi_n\sqrt{\frac{\kappa+3}{\kappa-3/2}}\,,$$

and

$$\varphi_{n\kappa} = \varphi_n\sqrt{\frac{\kappa}{\kappa-3/2}}\,,$$

where $\Omega_e = q_e B_0 / m_e c$ is the electron gyrofrequency.

Bibliography

[1] D. A. Gurnett and A. Bhattacharjee. *Introduction to Plasma Physics: With Space and Laboratory Applications*. Cambridge University Press, 2005. doi: 10.1017/CBO9780511809125.

[2] J.-F. Donati, F. Paletou, J. Bouvier, and J. Ferreira. Direct detection of a magnetic field in the innermost regions of an accretion disk. *Nature*, 438(7067): 466–469, 2005. doi: 10.1038/nature04253.

[3] J. Goodman and D. Uzdensky. Reconnection in marginally collisionless accretion disk coronae. *The Astrophysical Journal*, 688(1):555, 2008. doi: 10.1086/592345.

[4] W. M. Moslem, I. Kourakis, P. K. Shukla, and R. Schlickeiser. Nonlinear excitations in electron-positron-ion plasmas in accretion disks of active galactic nuclei. *Physics of Plasmas*, 14(10):102901, 2007. doi: 10.1063/1.2795127.

[5] M. Pollack, D. Pauls, and P. J. Wiita. Variability in active galactic nuclei from propagating turbulent relativistic jets. *The Astrophysical Journal*, 820(1):12, 2016. doi: 10.3847/0004-637X/820/1/12.

[6] E. N. Parker. Dynamics of the interplanetary gas and magnetic fields. *The Astrophysical Journal*, 128:664, 1958. doi: 10.1086/146579.

[7] H. S. Bridge, J. W. Belcher, A. J. Lazarus, J. D. Sullivan, R. L. McNutt, F. Bagenal, J. D. Scudder, E. C. Sittler, G. L. Siscoe, V. M. Vasyliunas, C. K. Goertz, and C. M. Yeates. Plasma observations near jupiter: Initial results from Voyager 1. *Science*, 204(4396):987–991, 1979. doi: 10.1126/science.204.4396.987.

[8] N. J. Fisch. Confining a Tokamak plasma with rf-driven currents. *Phys. Rev. Lett.*, 41(13):873–876, September 1978. doi: 10.1103/PhysRevLett.41.873.

[9] V. S. Mukhovatov and V. D. Shafranov. Plasma equilibrium in a Tokamak. *Nuclear Fusion*, 11(6):605, 1971. doi: 10.1088/0029-5515/11/6/005.

[10] R. Betti and O. A. Hurricane. Inertial-confinement fusion with lasers. *Nature Physics*, 12(5):435–448, 2016. doi: 10.1038/nphys3736.

[11] R. Schwenn. Space weather: The solar perspective. *Living Reviews in Solar Physics*, 3(1):2, 2006. doi: 10.12942/lrsp-2006-2.

[12] T. Pulkkinen. Space weather: Terrestrial perspective. *Living Reviews in Solar Physics*, 4(1):1, 2007. doi: 10.12942/lrsp-2007-1.

[13] C. J. Schrijver, K. Kauristie, A. D. Aylward, C. M. Denardini, S. E. Gibson, A. Glover, N. Gopalswamy, M. Grande, M. Hapgood, D. Heynderickx, N. Jakowski, V. V. Kalegaev, G. Lapenta, J. A. Linker, S. Liu, C. H. Mandrini, I. R. Mann, T. Nagatsuma, D. Nandy, T. Obara, T. P. O'Brien, T. Onsager, H. J. Opgenoorth, M. Terkildsen, C. E. Valladares, and N. Vilmer. Understanding space weather to shield society: A global road map for 2015–2025 commissioned by COSPAR and ILWS. *Advances in Space Research*, 55(12): 2745–2807, 2015. doi: 10.1016/j.asr.2015.03.023.

[14] C. Li, C.-L. Feng, H. Y. Oderji, G.-N. Luo, and H.-B Ding. Review of LIBS application in nuclear fusion technology. *Frontiers of Physics*, 11(6):114214, 2016. doi: 10.1007/s11467-016-0606-1.

[15] J. Ongena, R. Koch, R. Wolf, and H. Zohm. Magnetic-confinement fusion. *Nature Physics*, 12(5):398–410, 2016. doi: 10.1038/nphys3745.

[16] G. Fridman, G. Friedman, A. Gutsol, A. B. Shekhter, V. N. Vasilets, and A. Fridman. Applied plasma medicine. *Plasma Processes and Polymers*, 5(6): 503–533, 2008. doi: 10.1002/ppap.200700154.

[17] M. G. Kong, G. Kroesen, G. Morfill, T. Nosenko, T. Shimizu, J. van Dijk, and J. L. Zimmermann. Plasma medicine: an introductory review. *New Journal of Physics*, 11(11):115012, 2009. doi: 10.1088/1367-2630/11/11/115012.

[18] B. Jiang, J. Zheng, S. Qiu, M. Wu, Q. Zhang, Z. Yan, and Q. Xue. Review on electrical discharge plasma technology for wastewater remediation. *Chemical Engineering Journal*, 236:348–368, 2014. doi: 10.1016/j.cej.2013.09.090.

[19] C. A. Aggelopoulos. Recent advances of cold plasma technology for water and soil remediation: A critical review. *Chemical Engineering Journal*, 428:131657, 2022. doi: 10.1016/j.cej.2021.131657.

[20] H. Alfvén. Existence of electromagnetic-hydrodynamic waves. *Nature*, 150 (3805):405–406, 1942. doi: 10.1038/150405d0.

[21] P. J. Coleman. Turbulence, viscosity, and dissipation in the solar-wind plasma. *The Astrophysical Journal*, 153:371, 1968. doi: 10.1086/149674.

[22] R. Lundin and B. Hultqvist. Ionospheric plasma escape by high-altitude elec-

tric fields: Magnetic moment 'pumping'. *Journal of Geophysical Research: Space Physics*, 94(A6):6665–6680, 1989. doi: 10.1029/JA094iA06p06665.

[23] P. Rothwell and C. E. McIlwain. Magnetic storms and the Van Allen radiation belts—Observations from satellite 1958ε (Explorer IV). *Journal of Geophysical Research (1896-1977)*, 65(3):799–806, 1960. doi: 10.1029/JZ065i003p00799.

[24] C. T. Russell. Planetary magnetospheres. *Reports on Progress in Physics*, 56 (6):687, 1993. doi: 10.1088/0034-4885/56/6/001.

[25] T. E. Moore. Origins of magnetospheric plasma. *Reviews of Geophysics*, 29 (S2):1039–1048, 1991. doi: https://doi.org/10.1002/rog.1991.29.s2.1039.

[26] M. Blanc, R. Kallenbach, and N. V. Erkaev. Solar system magnetospheres. *Space Science Reviews*, 116(1):227–298, 2005. doi: 10.1007/s11214-005-1958-y.

[27] D. H. Mackay and A. R. Yeates. The Sun's global photospheric and coronal magnetic fields: Observations and models. *Living Reviews in Solar Physics*, 9 (1):6, 2012. doi: 10.12942/lrsp-2012-6.

[28] M. J. Owens and R. J. Forsyth. The heliospheric magnetic field. *Living Reviews in Solar Physics*, 10(1):5, 2013. doi: 10.12942/lrsp-2013-5.

[29] E. Marsch and H. Goldstein. The effects of Coulomb collisions on solar wind ion velocity distributions. *Journal of Geophysical Research: Space Physics*, 88 (A12):9933–9940, 1983. doi: 10.1029/JA088iA12p09933.

[30] T. H. Kho. Relaxation of a system of charged particles. *Physical Review A*, 32 (1):666–669, July 1985. doi: 10.1103/PhysRevA.32.666.

[31] B. D. Shizgal. Suprathermal particle distributions in space physics: Kappa

distributions and entropy. *Astrophysics and Space Science*, 312(3):227–237, 2007. doi: 10.1007/s10509-007-9679-1.

[32] V. Pierrard and M. Lazar. Kappa distributions: Theory and applications in space plasmas. *Solar Physics*, 267(1):153–174, 2010. doi: 10.1007/s11207-010-9640-2.

[33] C. Salem, D. Hubert, C. Lacombe, S. D. Bale, A. Mangeney, D. E. Larson, and R. P. Lin. Electron properties and Coulomb collisions in the solar wind at 1 au: Wind observations. *The Astrophysical Journal*, 585(2):1147, 2003. doi: 10.1086/346185.

[34] S. Landi, L. Matteini, and F. Pantellini. On the competition between radial expansion and coulomb collisions in shaping the electron velocity distribution function: Kinetic simulations. *The Astrophysical Journal*, 760(2):143, 2012. doi: 10.1088/0004-637X/760/2/143.

[35] J. V. Hollweg. Waves and instabilities in the solar wind. *Reviews of Geophysics*, 13(1):263–289, 1975. doi: 10.1029/RG013i001p00263.

[36] S. J. Schwartz. Plasma instabilities in the solar wind: A theoretical review. *Reviews of Geophysics*, 18(1):313–336, 1980. doi: 10.1029/RG018i001p00313.

[37] R. L. Mace. Whistler instability enhanced by suprathermal electrons within the Earth's foreshock. *Journal of Geophysical Research: Space Physics*, 103 (A7):14643–14654, 1998. doi: 10.1029/98JA00616.

[38] M. Lazar, R.A. López, S. M. Shaaban, S. Poedts, P. H. Yoon, and H. Fichtner. Temperature anisotropy instabilities stimulated by the solar wind suprathermal populations. *Frontiers in Astronomy and Space Sciences*, 8, 2022.

[39] B. T. Tsurutani and G. S. Lakhina. Some basic concepts of wave-particle interactions in collisionless plasmas. *Reviews of Geophysics*, 35(4):491–501, 1997. doi: 10.1029/97RG02200. Publisher: John Wiley & Sons, Ltd.

[40] S. P. Gary, L. Yin, and D. Winske. Electromagnetic proton cyclotron anisotropy instability: Wave-particle scattering rate. *Geophysical Research Letters*, 27(16):2457–2459, 2000. doi: 10.1029/2000GL000055.

[41] R. Koch. Wave–particle interactions in plasmas. *Plasma Physics and Controlled Fusion*, 48(12B):B329, 2006. doi: 10.1088/0741-3335/48/12B/S31.

[42] E. Marsch. Kinetic physics of the solar corona and solar wind. *Living Reviews in Solar Physics*, 3(1):1, 2006. doi: 10.12942/lrsp-2006-1.

[43] S. J. Bame, A. J. Hundhausen, J. R. Asbridge, and I. B. Strong. Solar wind ion composition. *Phys. Rev. Lett.*, 20(8):393–395, 1968. doi: 10.1103/PhysRevLett.20.393.

[44] E. Marsch, K.-H. Mühlhäuser, R. Schwenn, H. Rosenbauer, W. Pilipp, and F. M. Neubauer. Solar wind protons: Three-dimensional velocity distributions and derived plasma parameters measured between 0.3 and 1 au. *Journal of Geophysical Research: Space Physics*, 87(A1):52–72, 1982.

[45] M. R. Collier, D. C. Hamilton, G. Gloeckler, P. Bochsler, and R. B. Sheldon. Neon-20, oxygen-16, and helium-4 densities, temperatures, and suprathermal tails in the solar wind determined with WIND/MASS. *Geophysical Research Letters*, 23(10):1191–1194, 1996. doi: 10.1029/96GL00621.

[46] E. Marsch, X.-Z. Ao, and C.-Y. Tu. On the temperature anisotropy of the core part of the proton velocity distribution function in the solar wind. *Jour-*

nal of Geophysical Research: Space Physics, 109(A4), 2004. doi: 10.1029/2003JA010330.

[47] T. Nieves-Chinchilla and A. F. Viñas. Solar wind electron distribution functions inside magnetic clouds. *Journal of Geophysical Research: Space Physics*, 113(A2), 2008. doi: 10.1029/2007JA012703.

[48] W. C. Feldman, J. R. Asbridge, S. J. Bame, M. D. Montgomery, and S. P. Gary. Solar wind electrons. *Journal of Geophysical Research (1896-1977)*, 80 (31):4181–4196, 1975. doi: 10.1029/JA080i031p04181.

[49] J. D. Scudder and S. Olbert. A theory of local and global processes which affect solar wind electrons 2. Experimental support. *Journal of Geophysical Research: Space Physics*, 84(A11):6603–6620, 1979. doi: 10.1029/JA084iA11p06603.

[50] W. G. Pilipp, H. Miggenrieder, K. H. Mühlhäuser, H. Rosenbauer, R. Schwenn, and F. M. Neubauer. Variations of electron distribution functions in the solar wind. *Journal of Geophysical Research: Space Physics*, 92(A2):1103–1118, 1987. doi: 10.1029/JA092iA02p01103.

[51] M. Maksimovic, V. Pierrard, and P. Riley. Ulysses electron distributions fitted with Kappa functions. *Geophysical Research Letters*, 24(9):1151–1154, 1997. doi: 10.1029/97GL00992.

[52] V. Pierrard, M. Maksimovic, and J. Lemaire. Core, Halo and Strahl Electrons in the Solar Wind. *Astrophysics and Space Science*, 277(1):195–200, 2001. doi: 10.1023/A:1012218600882.

[53] Š. Štverák, P. M. Trávníček, M. Maksimovic, E. Marsch, A. N. Fazakerley, and E. E. Scime. Electron temperature anisotropy constraints in the solar

wind. *Journal of Geophysical Research: Space Physics*, 113(A3), 2008. doi: 10.1029/2007JA012733.

[54] V. Pierrard, M. Lazar, S. Poedts, Š. Štverák, M. Maksimovic, and P. M. Trávníček. The electron temperature and anisotropy in the solar wind. Comparison of the core and halo populations. *Solar Physics*, 291(7):2165–2179, 2016. doi: 10.1007/s11207-016-0961-7.

[55] J. Tao, L. Wang, Q. Zong, G. Li, C. Salem, R. F. Wimmer-Schweingruber, J. He, C. Tu, and S. D. Bale. Quiet-time suprathermal (∼0.1–1.5 keV) electrons in the solar wind. *The Astrophysical Journal*, 820(1):22, 2016. doi: 10.3847/0004-637X/820/1/22.

[56] L. B. Wilson, L.-J. Chen, S. Wang, S. J. Schwartz, D. L. Turner, M. L. Stevens, J. C. Kasper, A. Osmane, D. Caprioli, S. D. Bale, M. P. Pulupa, C. Salem, and K. A. Goodrich. Electron energy partition across interplanetary shocks. I. Methodology and data product. *The Astrophysical Journal Supplement Series*, 243(1):8, 2019. doi: 10.3847/1538-4365/ab22bd.

[57] L. B. Wilson, L.-J. Chen, S. Wang, S. J. Schwartz, D. L. Turner, M. L. Stevens, J. C. Kasper, A. Osmane, D. Caprioli, S. D. Bale, M. P. Pulupa, C. Salem, and K. A. Goodrich. Electron energy partition across interplanetary shocks. II. Statistics. *The Astrophysical Journal Supplement Series*, 245(2):24, 2019. doi: 10.3847/1538-4365/ab5445.

[58] M. Maksimovic, I. Zouganelis, J.-Y. Chaufray, K. Issautier, E. E. Scime, J. E. Littleton, E. Marsch, D. J. McComas, C. Salem, R. P. Lin, and H. Elliott. Radial evolution of the electron distribution functions in the fast solar wind

between 0.3 and 1.5 au. *Journal of Geophysical Research: Space Physics*, 110 (A9), 2005. doi: 10.1029/2005JA011119.

[59] Š. Štverák, M. Maksimovic, P. M. Trávníček, E. Marsch, A. N. Fazakerley, and E. E. Scime. Radial evolution of nonthermal electron populations in the low-latitude solar wind: Helios, Cluster, and Ulysses observations. *Journal of Geophysical Research: Space Physics*, 114(A5), 2009. doi: 10.1029/2008JA013883.

[60] L. Berčič, M. Maksimović, S. Landi, and L. Matteini. Scattering of strahl electrons in the solar wind between 0.3 and 1 au: Helios observations. *Monthly Notices of the Royal Astronomical Society*, 486(3):3404–3414, 2019. doi: 10.1093/mnras/stz1007.

[61] A. R. Macneil, M. J. Owens, M. Lockwood, Š. Štverák, and C. J. Owen. Radial evolution of sunward strahl electrons in the inner heliosphere. *Solar Physics*, 295(2):16, 2020. doi: 10.1007/s11207-019-1579-3.

[62] C. J. Owen, J. Abraham, G. Nicolaou, D. Verscharen, P. Louarn, and T. S. Horbury. Solar Orbiter SWA observations of electron strahl properties inside 1 au. *Universe*, 8(10), 2022. doi: 10.3390/universe8100509.

[63] S. P. Gary, W. C. Feldman, D. W. Forslund, and M. D. Montgomery. Heat flux instabilities in the solar wind. *Journal of Geophysical Research (1896-1977)*, 80(31):4197–4203, 1975. doi: 10.1029/JA080i031p04197.

[64] S. P. Gary, R. M. Skoug, and W. Daughton. Electron heat flux constraints in the solar wind. *Physics of Plasmas*, 6(6):2607–2612, 1999. doi: 10.1063/1.873532.

[65] S. M. Shaaban, M. Lazar, and S. Poedts. Clarifying the solar wind heat flux

instabilities. *Monthly Notices of the Royal Astronomical Society*, 480(1):310–319, 2018. doi: 10.1093/mnras/sty1567.

[66] R. A. López, M. Lazar, S. M. Shaaban, S. Poedts, and P. S. Moya. Alternative high-plasma beta regimes of electron heat-flux instabilities in the solar wind. *The Astrophysical Journal Letters*, 900(2):L25, 2020. doi: 10.3847/2041-8213/abaf56.

[67] S. P. Gary and W. C. Feldman. Solar wind heat flux regulation by the whistler instability. *Journal of Geophysical Research (1896-1977)*, 82(7):1087–1094, 1977. doi: 10.1029/JA082i007p01087.

[68] S. P. Gary, E. E. Scime, J. L. Phillips, and W. C. Feldman. The whistler heat flux instability: Threshold conditions in the solar wind. *Journal of Geophysical Research: Space Physics*, 99(A12):23391–23399, 1994. doi: 10.1029/94JA02067.

[69] S. P. Gary and H. Li. Whistler heat flux instability at high beta. *The Astrophysical Journal*, 529(2):1131, 2000. doi: 10.1086/308294.

[70] S. D. Bale, M. Pulupa, C. Salem, C. H. K. Chen, and E. Quataert. Electron heat conduction in the solar wind: Transition from Spitzer–Härm to the collisionless limit. *The Astrophysical Journal Letters*, 769(2):L22, 2013. doi: 10.1088/2041-8205/769/2/L22.

[71] S. Saeed, M. Sarfraz, P. H. Yoon, M. Lazar, and M. N. S. Qureshi. Electron heat flux instability. *Monthly Notices of the Royal Astronomical Society*, 465 (2):1672–1681, 2016. doi: 10.1093/mnras/stw2900.

[72] I. V. Kuzichev, I. Y. Vasko, A. R. Soto-Chavez, Y. Tong, A. V. Artemyev, S. D. Bale, and A. Spitkovsky. Nonlinear evolution of the whistler heat flux in-

stability. *The Astrophysical Journal*, 882(2):81, 2019. doi: 10.3847/1538-4357/ab3290.

[73] S. M. Shaaban, M. Lazar, P. H. Yoon, S. Poedts, and R. A. López. Quasi-linear approach of the whistler heat-flux instability in the solar wind. *Monthly Notices of the Royal Astronomical Society*, 486(4):4498–4507, 2019. doi: 10.1093/mnras/stz830.

[74] S.-Y. Lee, E. Lee, and P. H. Yoon. Nonlinear development of electron heat flux instability: Particle in cell simulation. *The Astrophysical Journal*, 876(2):117, 2019. doi: 10.3847/1538-4357/ab12db.

[75] A. Micera, A. N. Zhukov, R. A. López, M. E. Innocenti, M. Lazar, E. Boella, and G. Lapenta. Particle-in-cell simulation of whistler heat-flux instabilities in the solar wind: Heat-flux regulation and electron halo formation. *The Astrophysical Journal Letters*, 903(1):L23, 2020. doi: 10.3847/2041-8213/abc0e8.

[76] Lyman Spitzer and Richard Härm. Transport phenomena in a completely ionized gas. *Phys. Rev.*, 89(5):977–981, 1953. doi: 10.1103/PhysRev.89.977.

[77] S. Cuperman, A. Harten, and M. Dryer. Characteristics of the quiet solar wind beyond the Earth's orbit. *The Astrophysical Journal*, 177:555, 1972. doi: 10.1086/151732.

[78] D. W. Forslund. Instabilities associated with heat conduction in the solar wind and their consequences. *Journal of Geophysical Research (1896-1977)*, 75(1):17–28, 1970. doi: 10.1029/JA075i001p00017.

[79] J. V. Hollweg and J. R. Jokipii. Heat conduction in a turbulent magnetic field, with application to solar-wind electrons. *Journal of Geophysical Research*, 77(19):3311–3316, 1972. doi: 10.1029/JA077i019p03311.

[80] E. E. Scime, S. J. Bame, W. C. Feldman, S. P. Gary, J. L. Phillips, and A. Balogh. Regulation of the solar wind electron heat flux from 1 to 5 au: Ulysses observations. *Journal of Geophysical Research: Space Physics*, 99 (A12):23401–23410, 1994. doi: 10.1029/94JA02068.

[81] J. V. Hollweg. On electron heat conduction in the solar wind. *Journal of Geophysical Research (1896-1977)*, 79(25):3845–3850, 1974. doi: 10.1029/JA079i025p03845.

[82] F. Perkins. Heat conductivity, plasma instabilities, and radio star scintillations in the solar wind. *The Astrophysical Journal*, 179:637–642, 1973. doi: 10.1086/151902.

[83] R. A. López, S. M. Shaaban, M. Lazar, S. Poedts, P. H. Yoon, A. Micera, and G. Lapenta. Particle-in-cell simulations of the whistler heat-flux instability in solar wind conditions. *The Astrophysical Journal Letters*, 882(1):L8, 2019. doi: 10.3847/2041-8213/ab398b.

[84] S. M. Shaaban, M. Lazar, P. H. Yoon, and S. Poedts. The interplay of the solar wind core and suprathermal electrons: A quasilinear approach for firehose instability. *The Astrophysical Journal*, 871(2):237, 2019. doi: 10.3847/1538-4357/aaf72d.

[85] M. L. Adrian, A. F. Viñas, P. S. Moya, and D. E. Wendel. Solar wind magnetic fluctuations and electron non-thermal temperature anisotropy: Survey of WIND-SWE-VEIS observations. *The Astrophysical Journal*, 833(1):49, 2016. doi: 10.3847/1538-4357/833/1/49.

[86] M. Lazar, V. Pierrard, S. Poedts, and H. Fichtner. Characteristics of solar wind

suprathermal halo electrons. *Astronomy & Astrophysics*, 642:A130, 2020. doi: 10.1051/0004-6361/202038830.

[87] S. P. Gary and H. Karimabadi. Linear theory of electron temperature anisotropy instabilities: Whistler, mirror, and Weibel. *Journal of Geophysical Research: Space Physics*, 111(A11), 2006. doi: 10.1029/2006JA011764.

[88] E. Camporeale and D. Burgess. Electron firehose instability: Kinetic linear theory and two-dimensional particle-in-cell simulations. *Journal of Geophysical Research: Space Physics*, 113(A7), 2008. doi: 10.1029/2008JA013043.

[89] M. Lazar, S. Poedts, and R. Schlickeiser. The interplay of Kappa and core populations in the solar wind: Electromagnetic electron cyclotron instability. *Journal of Geophysical Research: Space Physics*, 119(12):9395–9406, 2014. doi: 10.1002/2014JA020668.

[90] A. F. Viñas, P. S. Moya, R. E. Navarro, J. A. Valdivia, J. A. Araneda, and V. Muñoz. Electromagnetic fluctuations of the whistler-cyclotron and firehose instabilities in a Maxwellian and Tsallis-kappa-like plasma. *Journal of Geophysical Research: Space Physics*, 120(5):3307–3317, 2015. doi: 10.1002/2014JA020554.

[91] M. Sarfraz, S. Saeed, P. H. Yoon, G. Abbas, and H. A. Shah. Macroscopic quasi-linear theory of electromagnetic electron cyclotron instability associated with core and halo solar wind electrons. *Journal of Geophysical Research: Space Physics*, 121(10):9356–9368, 2016. doi: 10.1002/2016JA022854.

[92] M. Lazar, S. M. Shaaban, H. Fichtner, and S. Poedts. Temperature anisotropy instabilities stimulated by the interplay of the core and halo electrons in space plasmas. *Physics of Plasmas*, 25(2):022902, 2018. doi: 10.1063/1.5016261.

[93] M. Lazar, P. H. Yoon, R. A. López, and P. S. Moya. Electromagnetic electron cyclotron instability in the solar wind. *Journal of Geophysical Research: Space Physics*, 123(1):6–19, 2018. doi: 10.1002/2017JA024759.

[94] P. S. Moya, M. Lazar, and S. Poedts. Toward a general quasi-linear approach for the instabilities of bi-Kappa plasmas. Whistler instability. *Plasma Physics and Controlled Fusion*, 63(2):025011, 2020. doi: 10.1088/1361-6587/abce1a.

[95] E. Husidic, M. Lazar, H. Fichtner, K. Scherer, and P. Astfalk. Linear dispersion theory of parallel electromagnetic modes for regularized Kappa-distributions. *Physics of Plasmas*, 27(4):042110, 2020. doi: 10.1063/1.5145181.

[96] M. Sarfraz, R. A. López, S. Ahmed, and P. H. Yoon. Electron mirror and cyclotron instabilities for solar wind plasma. *Monthly Notices of the Royal Astronomical Society*, 509(3):3764–3771, 2021. doi: 10.1093/mnras/stab3291.

[97] S. P. Gary and J. Wang. Whistler instability: Electron anisotropy upper bound. *Journal of Geophysical Research: Space Physics*, 101(A5):10749–10754, 1996. doi: 10.1029/96JA00323.

[98] R. Schlickeiser and T. Skoda. Linear theory of weakly amplified, parallel propagating, transverse temperature-anisotropy instabilities in magnetized thermal plasmas. *The Astrophysical Journal*, 716(2):1596, 2010. doi: 10.1088/0004-637X/716/2/1596.

[99] M. Lazar, S. Poedts, and R. Schlickeiser. Instability of the parallel electromagnetic modes in Kappa distributed plasmas – I. Electron whistler-cyclotron modes. *Monthly Notices of the Royal Astronomical Society*, 410(1):663–670, 2011. doi: 10.1111/j.1365-2966.2010.17472.x.

[100] P. Hellinger, P. M. Trávníček, V. K. Decyk, and D. Schriver. Oblique electron fire hose instability: Particle-in-cell simulations. *Journal of Geophysical Research: Space Physics*, 119(1):59–68, 2014. doi: 10.1002/2013JA019227.

[101] M. Lazar, S. M. Shaaban, S. Poedts, and Š. Štverák. Firehose constraints of the bi-Kappa-distributed electrons: a zero-order approach for the suprathermal electrons in the solar wind. *Monthly Notices of the Royal Astronomical Society*, 464(1):564–571, 2016. doi: 10.1093/mnras/stw2336.

[102] S. M. Shaaban, M. Lazar, R. A. López, H. Fichtner, and S. Poedts. Firehose instabilities triggered by the solar wind suprathermal electrons. *Monthly Notices of the Royal Astronomical Society*, 483(4):5642–5648, 2019. doi: 10.1093/mnras/sty3377.

[103] Y. Tong, I. Y. Vasko, A. V. Artemyev, S. D. Bale, and F. S. Mozer. Statistical study of whistler waves in the solar wind at 1 au. *The Astrophysical Journal*, 878(1):41, 2019. doi: 10.3847/1538-4357/ab1f05.

[104] J. S. Halekas, P. L. Whittlesey, D. E. Larson, D. McGinnis, S. D. Bale, M. Berthomier, A. W. Case, B. D. G. Chandran, J. C. Kasper, K. G. Klein, K. E. Korreck, R. Livi, R. J. MacDowall, M. Maksimovic, D. M. Malaspina, L. Matteini, M. P. Pulupa, and M. L. Stevens. Electron heat flux in the near-Sun environment. *Astronomy & Astrophysics*, 650, 2021. doi: 10.1051/0004-6361/202039256.

[105] C. Cattell, A. Breneman, J. Dombeck, E. Hanson, M. Johnson, J. Halekas, S. D. Bale, T. Dudok de Wit, K. Goetz, K. Goodrich, D. Malaspina, M. Pulupa, T. Case, J. C. Kasper, D. Larson, M. Stevens, and P. Whittlesey. Parker Solar Probe evidence for the absence of whistlers close to the Sun to scatter strahl

and to regulate heat flux. *The Astrophysical Journal Letters*, 924(2):L33, 2022. doi: 10.3847/2041-8213/ac4015.

[106] K. Horaites, P. Astfalk, S. Boldyrev, and F. Jenko. Stability analysis of core–strahl electron distributions in the solar wind. *Monthly Notices of the Royal Astronomical Society*, 480(2):1499–1506, 2018. doi: 10.1093/mnras/sty1808.

[107] S. M. Shaaban, M. Lazar, P. H. Yoon, and S. Poedts. Beaming electromagnetic (or heat-flux) instabilities from the interplay with the electron temperature anisotropies. *Physics of Plasmas*, 25(8):082105, 2018. doi: 10.1063/1.5042481.

[108] K. Scherer, H. Fichtner, and M. Lazar. Regularized κ-distributions with non-diverging moments. *Europhysics Letters*, 120(5):50002, 2018. doi: 10.1209/0295-5075/120/50002.

[109] K. Horaites, S. Boldyrev, and M. V. Medvedev. Electron strahl and halo formation in the solar wind. *Monthly Notices of the Royal Astronomical Society*, 484(2):2474–2481, 2018. doi: 10.1093/mnras/sty3504.

[110] I. Y. Vasko, V. Krasnoselskikh, Y. Tong, S. D. Bale, J. W. Bonnell, and F. S. Mozer. Whistler fan instability driven by strahl electrons in the solar wind. *The Astrophysical Journal Letters*, 871(2):L29, 2019. doi: 10.3847/2041-8213/ab01bd.

[111] C. Beck. Application of generalized thermostatistics to fully developed turbulence. *Physica A: Statistical Mechanics and its Applications*, 277(1):115–123, 2000. doi: 10.1016/S0378-4371(99)00508-7.

[112] I. Gallo-Méndez and P. S. Moya. Understanding the level of turbulence by

asymmetric distributions: A motivation for measurements in space plasmas. *The Astrophysical Journal*, 952(1):30, 2023. doi: 10.3847/1538-4357/acd6f0.

[113] C. Vocks, C. Salem, R. P. Lin, and G. Mann. Electron halo and strahl formation in the solar wind by resonant interaction with whistler waves. *The Astrophysical Journal*, 627(1):540, 2005. doi: 10.1086/430119.

[114] A. Bhatnagar and W. Livingston. *Fundamentals of Solar Astronomy*, volume 6 of *World Scientific Series in Astronomy and Astrophysics*. World scientific, 2005. doi: 10.1142/5171.

[115] Y. Kamide and A. C. L. Chian. *Handbook of the Solar-Terrestrial Environment*. 2007.

[116] J. Christensen-Dalsgaard. Solar structure and evolution. *Living Reviews in Solar Physics*, 18(1):2, 2021. doi: 10.1007/s41116-020-00028-3.

[117] N. Meyer-Vernet. *Basics of the Solar Wind*. Cambridge Atmospheric and Space Science Series. Cambridge University Press, Cambridge, 2007. doi: 10.1017/CBO9780511535765.

[118] M. Moldwin. *An Introduction to Space Weather*. Cambridge University Press, Cambridge, 2008. doi: 10.1017/CBO9780511801365.

[119] R. Erdélyi and I. Ballai. Heating of the solar and stellar coronae: a review. *Astronomische Nachrichten*, 328(8):726–733, 2007. doi: 10.1002/asna.200710803.

[120] S. K. Solanki, B. Inhester, and M. Schüssler. The solar magnetic field. *Reports on Progress in Physics*, 69(3):563, 2006. doi: 10.1088/0034-4885/69/3/R02.

[121] L. Bellot Rubio and D. Orozco Suárez. Quiet Sun magnetic fields: an

observational view. *Living Reviews in Solar Physics*, 16(1):1, 2019. doi: 10.1007/s41116-018-0017-1.

[122] P. Bochsler. Minor ions in the solar wind. *The Astronomy and Astrophysics Review*, 14(1):1–40, 2007. doi: 10.1007/s00159-006-0002-x.

[123] S. T. Lepri, E. Landi, and T. H. Zurbuchen. Solar wind heavy ions over solar cycle 23: ACE/SWICS measurements. *The Astrophysical Journal*, 768(1):94, 2013. doi: 10.1088/0004-637X/768/1/94.

[124] D. Verscharen, K. G. Klein, and B. A. Maruca. The multi-scale nature of the solar wind. *Living Reviews in Solar Physics*, 16(1):5, 2019. doi: 10.1007/s41116-019-0021-0.

[125] S. R. Habbal, R. Woo, S. Fineschi, R. O'Neal, J. Kohl, G. Noci, and C. Korendyke. Origins of the slow and the ubiquitous fast solar wind. *The Astrophysical Journal*, 489(1):L103, 1997. doi: 10.1086/310970.

[126] U. Feldman, E. Landi, and N. A. Schwadron. On the sources of fast and slow solar wind. *Journal of Geophysical Research: Space Physics*, 110(A7), 2005. doi: 10.1029/2004JA010918.

[127] B. T. Tsurutani, W. D. Gonzalez, A. L. C. Gonzalez, F. L. Guarnieri, N. Gopalswamy, M. Grande, Y. Kamide, Y. Kasahara, G. Lu, I. Mann, R. McPherron, F. Soraas, and V. Vasyliunas. Corotating solar wind streams and recurrent geomagnetic activity: A review. *Journal of Geophysical Research: Space Physics*, 111(A7), 2006. doi: 10.1029/2005JA011273.

[128] M. Temmer. Space weather: the solar perspective. *Living Reviews in Solar Physics*, 18(1):4, 2021. doi: 10.1007/s41116-021-00030-3.

[129] V. Pierrard, M. Maksimovic, and J. Lemaire. Electron velocity distribution functions from the solar wind to the corona. *Journal of Geophysical Research: Space Physics*, 104(A8):17021–17032, 1999. doi: 10.1029/1999JA900169.

[130] W. G. Pilipp, H. Miggenrieder, M. D. Montgomery, K. H. Mühlhäuser, H. Rosenbauer, and R. Schwenn. Characteristics of electron velocity distribution functions in the solar wind derived from the Helios plasma experiment. *Journal of Geophysical Research: Space Physics*, 92(A2):1075–1092, 1987. doi: 10.1029/JA092iA02p01075.

[131] K. Horaites, S. Boldyrev, L. B. Wilson, A. F. Viñas, and J. Merka. Kinetic theory and fast wind observations of the electron strahl. *Monthly Notices of the Royal Astronomical Society*, 474(1):115–127, 2017. doi: 10.1093/mnras/stx2555.

[132] D. Verscharen, B. D. G. Chandran, E. Boella, J. Halekas, M. E. Innocenti, V. K. Jagarlamudi, A. Micera, V. Pierrard, Š. Štverák, I. Y. Vasko, M. Velli, and P. L. Whittlesey. Electron-driven instabilities in the solar wind. *Frontiers in Astronomy and Space Sciences*, 9, 2022. doi: 10.3389/fspas.2022.951628.

[133] S. P. Gary. *Theory of Space Plasma Microinstabilities*. Cambridge Atmospheric and Space Science Series. Cambridge University Press, 1993. doi: 10.1017/CBO9780511551512.

[134] T. H. Stix. *Waves in Plasmas*. American Institute of Physics, 1992.

[135] Peter H. Yoon. Generalized weak turbulence theory. *Physics of Plasmas*, 7(12):4858–4871, 2000. doi: 10.1063/1.1318358.

[136] R. Fitzpatrick. *Plasma physics: An introduction*. Crc Press, 2022.

[137] S. M. Shaaban and M. Lazar. Whistler instabilities from the interplay of electron anisotropies in space plasmas: a quasi-linear approach. *Monthly Notices of the Royal Astronomical Society*, 492(3):3529–3539, 2019. doi: 10.1093/mnras/stz3569.

[138] P. Astfalk and F. Jenko. LEOPARD: A grid-based dispersion relation solver for arbitrary gyrotropic distributions. *Journal of Geophysical Research: Space Physics*, 122(1):89–101, 2017. doi: 10.1002/2016JA023522.

[139] E. E. Scime, J. E. Littleton, S. P. Gary, R. Skoug, and N. Lin. Solar cycle variations in the electron heat flux: Ulysses observations. *Geophysical Research Letters*, 28(11):2169–2172, 2001. doi: 10.1029/2001GL012925.

[140] B. Zenteno-Quinteros, A. F. Viñas, and P. S. Moya. Skew-kappa distribution functions and whistler heat flux instability in the solar wind: The core-strahlo model. *The Astrophysical Journal*, 923(2):180, 2021. doi: 10.3847/1538-4357/ac2f9c.

[141] B. Zenteno-Quinteros and P. S. Moya. The role of core and strahlo electrons properties on the whistler heat-flux instability thresholds in the solar wind. *Frontiers in Physics*, 10:910193, 2022. doi: 10.3389/fphy.2022.910193.

[142] S. Olbert. Summary of experimental results from M.I.T. detector on IMP-1. In *Physics of the Magnetosphere*, pages 641–659, Dordrecht, 1968. Springer Netherlands.

[143] V. M. Vasyliunas. A survey of low-energy electrons in the evening sector of the magnetosphere with OGO 1 and OGO 3. *Journal of Geophysical Research (1896-1977)*, 73(9):2839–2884, 1968. doi: 10.1029/JA073i009p02839.

[144] J. D. Scudder. Electron and ion temperature gradients and suprathermal tail strengths at Parker's solar wind sonic critical point. *Journal of Geophysical Research: Space Physics*, 101(A5):11039–11053, 1996. doi: 10.1029/96JA00188.

[145] F. Xiao, Q. Zhou, H. Zheng, and S. Wang. Whistler instability threshold condition of energetic electrons by kappa distribution in space plasmas. *Journal of Geophysical Research: Space Physics*, 111(A8), 2006. doi: 10.1029/2006JA011612.

[146] M. Lazar, H. Fichtner, and P. H. Yoon. On the interpretation and applicability of κ-distributions. *Astronomy & Astrophysics*, 589, 2016. doi: 10.1051/0004-6361/201527593.

[147] A. F. Viñas, R. Gaelzer, P. S. Moya, R. Mace, and J. A. Araneda. Chapter 7 - Linear kinetic waves in plasmas described by Kappa distributions. In George Livadiotis, editor, *Kappa Distributions*, pages 329–361. Elsevier, 2017. doi: 10.1016/B978-0-12-804638-8.00007-3.

[148] C. M. Bender and S. A. Orszag. *Advanced mathematical methods for scientists and engineers I: Asymptotic methods and perturbation theory*, volume 1. Springer Science & Business Media, 1999.

[149] R. L. Mace and M. A. Hellberg. A dispersion function for plasmas containing superthermal particles. *Physics of Plasmas*, 2(6):2098–2109, 1995. doi: 10.1063/1.871296.

[150] M. A. Hellberg and R. L. Mace. Generalized plasma dispersion function for a plasma with a kappa-Maxwellian velocity distribution. *Physics of Plasmas*, 9 (5):1495–1504, 2002. doi: 10.1063/1.1462636.

[151] D. Summers and R. M. Thorne. The modified plasma dispersion function. *Physics of Fluids B: Plasma Physics*, 3(8):1835–1847, 1991. doi: 10.1063/1.859653.

[152] S. Rizzo, A. Rapisarda, and CACTUS Group. Environmental atmospheric turbulence at Florence airport. *AIP Conference Proceedings*, 742(1):176–181, 2004. doi: 10.1063/1.1846475.

[153] I. Gallo-Méndez and P. S. Moya. Langevin based turbulence model and its relationship with Kappa distributions. *Scientific Reports*, 12(1):2136, 2022. doi: 10.1038/s41598-022-05996-0.

[154] T. H. Stix. *The theory of plasma waves*. McGraw-Hill, 1962.

[155] N. A. Krall, A. W. Trivelpiece, and R. A. Gross. Principles of plasma physics. *American Journal of Physics*, 41(12):1380–1381, 1973. doi: 10.1119/1.1987587.

[156] B. D. Fried and S. D. Conte. *The Plasma Dispersion Function*. 1961. doi: 10.1016/C2013-0-12176-9.

[157] S. P. Gary. Electromagnetic electron beam instabilities: Hot, isotropic beams. *Journal of Geophysical Research: Space Physics*, 90(A11):10815–10822, 1985. doi: 10.1029/JA090iA11p10815.

[158] B. Abraham-Shrauner and W. C. Feldman. Whistler heat flux instability in the solar wind with bi-Lorentzian velocity distribution functions. *Journal of Geophysical Research (1896-1977)*, 82(13):1889–1892, 1977. doi: 10.1029/JA082i013p01889.

[159] A. Shrauner and W. C. Feldman. Electromagnetic ion-cyclotron wave growth

rates and their variation with velocity distribution function shape. *Journal of Plasma Physics*, 17(1):123–131, 1977. doi: 10.1017/S002237780002047X.

[160] I. B. Bernstein. Waves in a plasma in a magnetic field. *Phys. Rev.*, 109(1): 10–21, 1958. doi: 10.1103/PhysRev.109.10.

[161] B. Zenteno-Quinteros, P. S. Moya, M. Lazar, A. F. Viñas, and S. Poedts. Interplay between anisotropy- and skewness-driven whistler instabilities in the solar wind under the core–strahlo model. *The Astrophysical Journal*, 954(2): 184, 2023. doi: 10.3847/1538-4357/ace973.

[162] R. A. López, M. Lazar, S. M. Shaaban, S. Poedts, and P. S. Moya. A firehose-like aperiodic instability of counter-beaming electron plasmas. *Plasma Physics and Controlled Fusion*, 62(7):075006, 2020. doi: 10.1088/1361-6587/ab8bb5.